Molecular Beam Epitaxy Growth and Structural Property of Self-assembled InAs Quantum Dots on GaAs

Dissertation
zur Erlangung des Doktorgrades
des Fachbereichs Physik
der Universität Hamburg

vorgelegt von
Kai Zhang
aus Shenyang, China

Hamburg
2000

Gutachter der Dissertation:	Professor Dr. W. Hansen Professor Dr. J. Falta
Gutachter der Disputation:	Professor Dr. W. Hansen Professor Dr. R. L. Johnson
Datum der Disputation:	August 25, 2000
Dekan des Fachbereichs Physik und Vorsitzender des Promotionsausschusses:	Professor Dr. F.-W. Büßer

for God !
for my daughter !

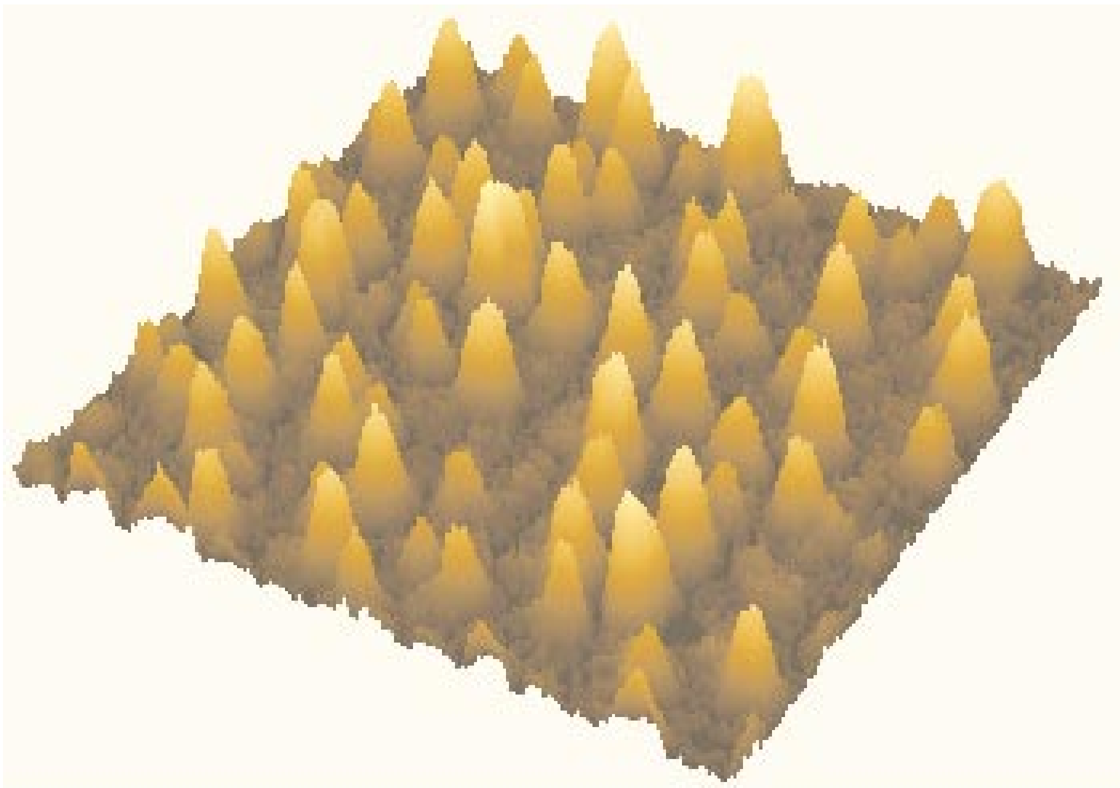

Fig. 1: *Quantum dots will enter your life in next century... ...*

Abstract

Self-assembled InAs quantum dots (QDs) with a few 10 nanometer (nm) size and atomic-like zero-dimensional electron states have prospective applications in semiconductor opto-electronic devices. Structural features in such system are essential and highly influence the opto-electronic properties of the dots. In the present work, we focus on methods for structural characterization to evaluate structure properties of InAs QDs, such as ordering, shape, composition and strain status.

Quantitative x-ray diffraction and atomic force microscopy (AFM) experiments have been performed on self-assembled InAs QDs grown by molecular-beam epitaxy (MBE). *In situ* RHEED was utilized to control the InAs coverage. We find InAs deposited for homogeneous InAs QD growth is limited to be 2.3 ML, beyond which saturation effects of the dot number density are observed by AFM.

From grazing incidence small angle x-ray scattering (GISAXS) we find pronounced non-specular diffuse scattering satellite peaks, indicating a lateral ordering in InAs QD distribution. Mean dot-dot distances and correlation lengths of the dot lateral distribution are found to be anisotropic. We determine the most pronounced ordering of dot distribution in [110] direction. Moreover, we observe additional broad intensity peaks induced by the truncation rod intensity of InAs QD facets that enable us to reveal the QD shape as a truncated octagonal-based pyramid.

The grazing incidence x-ray diffraction (GIXRD) technique allows determination of strain status inside the InAs QDs. Strain as a driving force for InAs QD formation, is revealed experimentally to be elastic with different components in all measured samples. Furthermore, a small volume fraction of relaxed $In_xGa_{1-x}As$ is found in samples with relative low As-flux.

In addition, the atomic structure at the interface of buried InAs ultra-thin films is a dominant element for opto-electronic properties of InAs quantum wells fabricated by

hetero-epitaxy of MBE growth. We structurally characterize the interface by using the combination of grazing incidence x-ray reflectivity (GIXR), crystal truncation rod (CTR) and x-ray standing wave (XSW) techniques. GIXR and CTR experiments were utilized to determine the average layer thickness, interface roughness, and the stoichiometry of the InAs layer. XSW experiments determine the In lattice site and vertical distribution at the interface.

Inhaltsangabe

Selbstorganisierte InAs Quantenpunkte (QDs) mit Abmessungen von wenigen 10 Nanometern (nm) und mit Atom-ähnlichen null-dimensionalen Elektronenzuständen haben potentielle Anwendungen in Bauelementen der Halbleiter-Optoelektronik. Die strukturellen Eigenschaften solcher Systeme sind von wesentlicher Bedeutung und beeinflussen entscheidend die opto-elektronischen Eigenschaften der Quantenpunkte. In der vorliegenden Arbeit liegt das Hauptaugenmerk auf Methoden zur strukturellen Charakterisierung, mit denen die strukturellen Eigenschaften von InAs QDs, wie Anordnung, Form, Komposition und Verspannung ermittelt werden können.

Quantitative Röntgendiffraktion und Rasterkraftmikroskopie (Atomic Force Microscopy, AFM) wurden an selbstorganisierten InAs QDs durchgeführt, die durch Molekular-Strahl-Epitaxie (MBE) gewachsen wurden. Es wurde Elektronenbeugung (RHEED) ver-wendet, um das Wachstum und die Dicke der InAs-Schichten zu kontrol-lieren. Wir finden, daß die InAs-Schichtdicke für ein homogenes InAs QD Wachstum auf 2.3 ML begrenzt ist, und daß bei höheren Bedeckungen Sätti-gungseffekte der Dichte der QD mittels AFM beobachtet werden können.

Mit Röntgenstreuexperimenten bei streifendem Einfall (grazing incidence small angle x-ray scattering GISAXS) werde deutliche, nicht spekulare Satellitenpeaks beo-bachtet, die auf eine laterale Ordnung der InAs Quantenpunkte hinweisen. Der mittlere Abstand zwischen den QD und die Korrelationslängen der lateralen Verteilung sind ani-sotrop. Wir stellen fest, daß die Verteilung der QD in Richtung [110] am regelmäßig-sten ist.

Außerdem beobachten wir zusätzliche breite Peaks in der Streuintensität bei größeren Winkeln, die durch reziproke Gitterstäbe senkrecht in den InAs QD Facetten induziert werden. Das ermöglicht uns, die QD-Form als abgeflachte Pyramide mit oktago-na-ler Basis zu bestimmen.

Die Technik der Röntgenstreuung (Grazing incidence x-ray diffracting, GIXRD) bei streif-

endem Einfall erlaubt die Bestimmung des Verspannungszustandes innerhalb der InAs QDs. Die Verspannung als treibende Kraft für die Bildung von InAs QD zeigt sich experimentell in allen gemessenen Proben als elastisch mit unterschiedlichen Komponenten. Außerdem findet sich ein kleiner Volumenanteil von relaxiertem $In_xGa_{1-x}As$ in Proben mit niedrigem Arsenfluß.

Zusätzlich ist die atomare Struktur an der Grenzfläche eines vergrabenen ultradünnen InAs Films ein wichtiges Element für die opto-elektronischen Eigenschaften der durch heteroepitaktisches MBE-Wachstum hergestellten InAs Quantenwells. Wir charakterisieren die Struktur der Grenzfläche mit einer Kombination aus Techniken der Röntgenuntersuchungen, wie Reflektion unter streifen-dem Einfall (grazing incidence x-ray reflectivity, GIXR), Crystal Truncation Rod (CTR) und x-ray standing wave (XSW). Mit GIXR und CTR-Experimenten wurde die durchschnittliche Schichtdicke, die Rauhigkeit der Grenzfläche und die Stoichiometrie der InAs-Schichten bestimmt. XSW-Experimente bestimmen die Position der In-Atome im Gitter sowie die vertikale Verteilung an der Grenzfläche.

Contents

Abstract **i**

Inhaltsangabe **iii**

1 Introduction **1**

2 Molecular Beam Epitaxy **4**

2.1 In general 4

2.2 Fundamentals of the MBE growth 5

2.2.1 Basic physical processes of MBE growth 5

2.2.2 Lattice mismatch between epilayer and substrate 8

2.2.3 Crystallographic orientation of the substrate 10

2.3 Self-assembling effect in MBE growth 13

2.4 Reflection High Energy Electron Diffraction 14

3 Principle of X-ray Experimental Methods **18**

3.1 In general 18

3.2 Background of x-ray diffraction 19

3.2.1 X-ray optics 19

3.2.2 X-ray diffraction intensity 20

3.3 Grazing Incidence X-ray Diffraction 22

3.4 Grazing Incidence Small Angle X-ray Scattering 27
3.5 Grazing Incidence X-ray Reflectivity 30
3.6 Crystal Truncation Rods 34
3.7 X-Ray Standing Waves 38

4 Experimental Setup 44
4.1 In general 44
4.2 MBE growth procedure 44
4.3 X-ray experiments 48
4.3.1 X-ray Topography 50
4.3.2 Grazing incidence x-ray experiments 52
4.3.3 Crystal Truncation Rod Technique 53
4.3.4 X-ray Standing Wave Technique 53
4.4 Summary 55

5 Growth Investigation by RHEED 56
5.1 In general 56
5.2 *In situ* RHEED pattern 56
5.3 RHEED intensity observation 58

6 AFM Investigations on Self-assembled InAs QDs 60
6.1 In general 60
6.2 AFM image 60

7 Ordering and Shape of Self-assembled Uncapped InAs QDs 64
7.1 Research focus 64
7.2 Sample preparation 66
7.3 Experimental 66
7.4 Results and discussions 67

7.4.1 AFM results 67
7.4.2 GISAXS results 70
7.5 Summary 75

8 Ordering Study on Self-assembled Capped InAs QDs 76

9 Strain Status of Self-assembled InAs QDs 81
9.1 Research focus 81
9.2 Sample preparation 82
9.3 GIXRD experimental 83
9.4 Results and discussions 83
9.4.1 The first type of samples 83
9.4.2 The second type of samples 89
9.5 Summary 95

10 Interface Characterization of Buried InAs Monolayers 96
10.1 Research focus 96
10.2 Sample growth 98
10.3 X-ray experimental 98
10.4 Results and discussions 99
10.4.1 GIXR 99
10.4.2 CTR 103
10.4.3 XSW 105
10.5 Summary 107

11 Conclusion and Prospect 108

Literature 113

Publications 122

List of Figures

Fig. 1: InAs QDs 4

Fig. 2: MBE system 5

Fig. 3: Surface processes 7

Fig. 4: Three crystal growth modes 7

Fig. 5: Step surfaces 11

Fig. 6: Surface bonds 12

Fig. 7: RHEED diffraction geometry 15

Fig. 8: RHEED pattern 16

Fig. 9: GaAs surface $c(4\times4)$ reconstruction 16

Fig. 10: RHEED-azimuths 17

Fig. 11: Laue-Bragg diffraction condition 20

Fig. 12: Penetration depth in grazing case 24

Fig. 13: Schematic illustration of GIXRD 26

Fig. 14: Schematic illustration of GISAXS 29

Fig. 15: Reflection and transmission waves at the mth layer 31

Fig. 16: Calculated reflectivities for GaAs thin film 33

Fig. 17: Principle of CTR 36

Fig. 18: Model of CTR oscillations 37

Fig. 19: Reflectivity R, phase shift φ curves and XSW field movement 41

Fig. 20: Relation between atomic positions and Fluorescence yields 43

Fig. 21: Schematic illustration of cell positions in Riber-32P MBE system . . . 45
Fig. 22: In flux projection 46
Fig. 23: In coverage by fluorescence measurements 47
Fig. 24: Distribution of QD number densities 48
Fig. 25: X-ray diffraction geometry 49
Fig. 26: Setup of Topography 51
Fig. 27: Topographic images 52
Fig. 28: X-ray standing wave performance 54
Fig. 29: Schematic illustration of x-ray experiments in reciprocal space 55

Fig. 30: *In situ* RHEED patterns 58
Fig. 31: RHEED intensity curve 59

Fig. 32: AFM image of InAs QDs 61
Fig. 33: InAs QD height distribution 62
Fig. 34: InAs QDs on stepped surface 63

Fig. 35: Schematic illustration of ordering situation 68
Fig. 36: a zoom of AFM image 69
Fig. 37: AFM Fourier transformation 69
Fig. 38: GISAXS intensity curves 71
Fig. 39: Azimuthal distribution of GISAXS intensity 73
Fig. 40: GISAXS intensities at different q_z values 73
Fig. 41: Sketched InAs QD shape 75

Fig. 42: AFM image on capped InAs QDs 77
Fig. 43: Sketched GISAXS setup 77
Fig. 44: GISAXS intensity map 79

Fig. 45: GISAXS intensity curves 80

Fig. 46: AFM image of InAs QDs 83

Fig. 47: 3-dimensional plot of GIXRD intensity 84

Fig. 48: Reciprocal space map of InAs (202) Bragg diffraction 85

Fig. 49: Distinction of intensity position between InAs and $In_xGa_{1-x}As$ 87

Fig. 50: Intensity maxima with different strain components 89

Fig. 51: Reciprocal space q_x or $q_y - q_z$ map 91

Fig. 52: Intensity peak position 92

Fig. 53: Intensity maxima distribution 92

Fig. 54: Reciprocal space $q_x - q_y$ maps 93

Fig. 55: Strain dependent lateral size distribution inside InAs QDs 94

Fig. 56: GIXR intensity curves for samples grown at 500^0C 100

Fig. 57: Dispersion correction models 101

Fig. 58: GIXR intensity curves for samples grown at 450^0C 102

Fig. 59: CTR intensity curve 104

Fig. 60: XSW fluorescence and reflectivity curves 106

Chapter 1

Introduction

Semiconductor heterostructures which exhibit quantum confinement in three dimensions (3D) - socalled quantum dots (QDs) - are presently of high interest for fundamental research as well as technology [Hei93]. In experiments the atom-like electronic states in the quantum dots are occupied with a controlled number of electrons offering the possibility to study interaction and correlation effects as function of electron occupation in potentials different in shape and size to those of real atoms. On the other hand the high density of states associated with the dots can be very profitable for semiconductor laser applications. For the preparation of quantum dots focus of interest has recently been devoted to self-assembling mechanisms occurring in III-V materials grown by molecular beam epitaxy (MBE) with highly strained heterolayers, e.g. InAs (InGaAs)/GaAs systems. A few years ago the first experimental evidence for the existence of zero-dimensional electronic states in self-assembled InAs QDs was obtained with capacitance and Far Infrared Spectroscopy [Dre94]. Since then this type of QDs has been studied very intensively by means of a wide spectrum of techniques in view of both fundamental aspects as well as potential technological applications [bim98]. The atomic like electron states have been probed by, e. g. photoluminescence [Mar94, Sch97], cathodoluminescence [Gru95a], capacitance measurements [Mil97] and Far Infrared Spectroscopy [Fri96, Sau97], as well as Ballistic Electron Emission Spectroscopy [Rub96]. From these studies one can predict that there exhibits a prospective application in the near future. Meanwhile, we are also aware of the fact that the structural organization of the dots is a dominant element in such systems, which may strongly influence their optoelectronic property. The dots with coherent strain, dislocation-free, and having a surprisingly narrow size distribution are highly desired. The most optimized point is to make the dots with high ordering in lateral distribution. For

the electronic device application reason, the quantum dots at least must be capped/or buried by a so-called cap layer.

In addition, considerable efforts have been devoted to understand the opto-electronic and structural properties of quantum wells fabricated by hetero-epitaxy of, e. g. MBE grown GaAs/InAs/GaAs(001) layers. Moreover, much interest is devoted to the understanding of structural formation of ultra-thin InAs layers buried in GaAs, since the information on the atomic structure of the interface is essential to fully understand the electronic properties of such heterostructures. The issue of the 7% lattice mismatch is one the major obstacles for InAs/GaAs epitaxy. The interface morphology, film strain, and dislocation existence are strongly affected by the discrepancy of this large lattice mismatch.

For MBE heterostructure growth, it is possible to adjust the thickness of thin film so that the lateral lattice parameter of the thin film is strained to match the substrate crystal lattice. However, the most intriguing response occurs when the film thickness deposited closes to the critical film thickness, below which the lateral lattice parameter of the film is strained to match that of the substrate. The corresponding vertical lattice parameter compensates in the opposite sense. As the film thickness increases above its critical thickness, the lateral lattice parameter relaxes towards the bulk value with a corresponding decrease in the vertical response. This may result in the dislocation inside the thin film. However, in the case of e.g. InAs film on GaAs, 3D islands with dislocation free inside are formed as soon as the deposited InAs coverage thickness exceeds its critical thickness. As we know, the strain relaxation in the epitaxy layer as a driving force, forms QD structures with socalled Stranski-Krastanov growth mode [Str39]. Such 3D InAs QDs were intensively investigated worldwide in recent years, as indicated in the Chap. 7, Sec. 7.1 and Chap. 9, Sec. 9.1. Also, many works have been done experimentally and theoretically in order to highlight the mechanism of the ultra-thin InAs film formation, see Chap. 10, Sec. 10.1. However, there is no definite picture about them so far.

Segregation effects at III-V semiconductor heterointerfaces have been the key focus of numerous investigation throughout the past few years. Because that the segregation effects may change the originally designed interface composition profiles of the heterostructure and the relative electronic properties, the quantitative determination on the actual composition profile in the fine structure is no doubt very crucial for us to fully understand the interface structure in such hetero-system.

In order to reveal the structure properties of InAs QDs and InAs quantum well grown on GaAs substrate, in the present work we utilize x-ray diffraction techniques supported by

synchrotron radiation with high flux rate, which may provide us an opportunity to study such small quantum confinements.

Some fundamental aspects concerning MBE growth and x-ray diffraction which is important for the discussion of the experiments presented in the following are introduced in Chap. 2 and Chap. 3, respectively. Chap. 4 describes the present experimental procedures including both MBE growth and X-ray techniques employed in the present work. In Chap. 5, we study ultra-thin InAs film growth and InAs QD formation by means of reflection high energy electron diffraction (RHEED) experiments. Especially, we address on structural characterization as following:

In Chap. 6, we perform atomic force microscopy (AFM) investigation on InAs QDs grown with different InAs deposit coverage.
In Chap. 7, grazing incidence small angle x-ray scattering (GISAXS) technique is utilized to study lateral ordering of uncapped InAs QD distribution and to determine QD facet features.
In Chap. 8, GISAXS technique is also performed to reveal the ordering situation on capped InAs QDs.
In Chap. 9, we discuss experimentally the very important structure parameter for InAs QD formation, i.e. strain status inside QDs, in the case of different InAs growth conditions. The experiments on such structure characterization were performed by means of grazing incidence x-ray diffraction (GIXRD).
In Chap. 10, a combination of grazing incidence x-ray reflectivity (GIXR), crystal truncation rods (CTR) and x-ray standing waves (XSW) techniques is employed to characterize the surface and interface structural features in buried ultra-thin InAs film systems with a few monolayers, i.e. surface and interface roughness, In segregation effect, interface composition profile and In atom sites at the interface.

This thesis will end with conclusions and prospects in Chap. 11.

Chapter 2

Molecular Beam Epitaxy

2.1 In general

The samples studied in this work were grown by MBE. This technique is a very powerful tool for epitaxial growth of semiconductor, metal and insulator thin films on single crystalline substrates. The growth is achieved using a directed beam of neutral atoms or molecules possessing only thermal energy. This beam can be generated with two different methods. The first method is the evaporation from a Knudsen cell which is a thermally heated oven containing the materials. The other one uses an electron beam to evaporate the materials from a well cooled cell. Usually the substrate is heated during the growth to improve the diffusion of the atoms on the sample surface. In order to prevent any contamination of the samples and to avoid collisions of the molecular beam with residual gas, the growth process is performed under ultra-high vacuum (UHV)conditions of the order of 10^{-11} mbar. All beam sources can be closed by a mechanical beam shutter to define the sequence and composition of the various layers. MBE is an epitaxial growth process involving the reaction of one or more thermal beams of atoms or molecules with a crystalline surface under UHV conditions. The knowledge of surface physics and the observation of surface atom rearrangements resulting from the relations between the beam fluxes and the substrate temperature allow considerable understanding of how to prepare high quality thin films with compilation of atomic layer upon atomic layer. A great advantage of the MBE method as compared to conventional vacuum evaporation techniques is the ability to precisely control the beam fluxes and deposition conditions, and the opportunity to perform *in situ* growth control via surface sensitive tools like Reflection High

Energy Electron Diffraction (RHEED). More detailed information on the MBE technique is provided, e.g. in Ref. [Cha85, Her89, Far95].

2.2 Fundamentals of the MBE growth

2.2.1 Basic physical processes of MBE growth

The essential elements of a MBE system are shown schematically in Fig. 2. It is clear that a MBE system is divided into three zones where different physical phenomena take place.

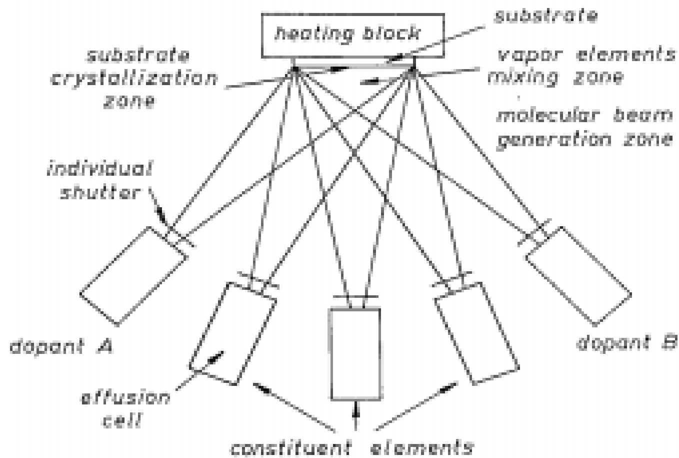

Fig. 2: Schematic illustration of the essential parts of a MBE growth system. Three zones where the basic processes of MBE take place are indicated [Her82].

The molecular beams are generated in the first zone under UHV conditions from sources of material cells, whose temperatures are accurately controlled. Conventional temperature control, based on high performance proportional-integral-derivative controllers and thermocouple feedback, enables a flux stability of better than $\pm 1\%$. By choosing e.g. appropriate flux rates of deposited materials and substrate temperatures, epitaxial films of the desired chemical composition can be obtained. Accurately selected and controlled temperatures for the substrate and for the sources of the constituent beams have thus a direct effect upon the growth process. The uniformity in thickness as well as in the composition of the films grown by MBE depends on the uniformities of the molecular beam fluxes and also on the geometrical relationship between the configurations of the sources and the substrate. As to the latter case, the substrate can be rotated during

the growth with a constant angular velocity around the axis perpendicular to its surface. The substrate rotation causes a considerable enhancement in thickness and composition homogeneity of the grown epilayer [Cho81].

The second zone in the MBE vacuum reactor is the mixing zone, where the molecular beams intersect each other. Since the mean free path of the molecules belonging to the intersecting beams is so long, no collisions and no other interactions between the molecules of different species occur in this zone.

The third zone, i.e. on the substrate surface, epitaxial growth of MBE is realized. Although, a series of surface processes are involved in MBE growth, the following are the most important [Mad83]:

i) Adsorption of the constituent atoms or molecules impinging on the substrate surface,
ii) Surface migration and dissociation of the adsorbed molecules,
iii) Incorporation of the constituent atoms into the crystal lattice of the substrate or the epilayer already grown,
iv) The thermal desorption of the atoms not associated with the crystal lattice.

These processes are schematically illustrated in Fig. 3 [Her86]. The substrate crystal surface is displayed by crystal lattice sites, with which the impinging molecules or atoms may interact. Each crystal site is a small part of the crystal surface characterized by its individual chemical activity. A site may be created by a dangling bond, vacancy, step edge, etc. [Lew78].The surface processes occurring during MBE growth are characterized from a set of relevant kinetic parameters that describe them quantitatively [Her89].

Three possible modes of MBE crystal growth on surfaces may be distinguished, as illustrated schematicallly in Fig. 4 [Ven84]. The layer-by-layer, or Frank-van der Merwe mode, displays the opposite characteristics. Because the atoms are more strongly bound to the substrate than to each other, the atoms form a complete monolayer on the surface, which is covered with a somewhat less tightly bound second layer. Provided the decrease in binding is monotonic towards the value for a bulk crystal of the deposit, the layer growth mode is achieved.

In the island, or Volmer-Weber mode, small clusters are nucleated directly on the substrate surface and then grow into islands of the condensed phase. This happens when the atoms, or molecules, of the deposit are more strongly bound to each other than to the substrate.

The layer plus island, or Stranski-Krastanov [Str39] growth mode is an intermediate case. After forming the first monolayer, or a few monolayers, subsequent layer growth is unfa-

vorable and islands are formed on top of this intermediate layer. There are many possible reasons for this mode to occur and almost any factors which disturb the monotonic decrease in binding energy characteristic for layer-by-layer growth may be the cause [Ven84]. In the following, we will discuss strain status, which plays an important role for island formation.

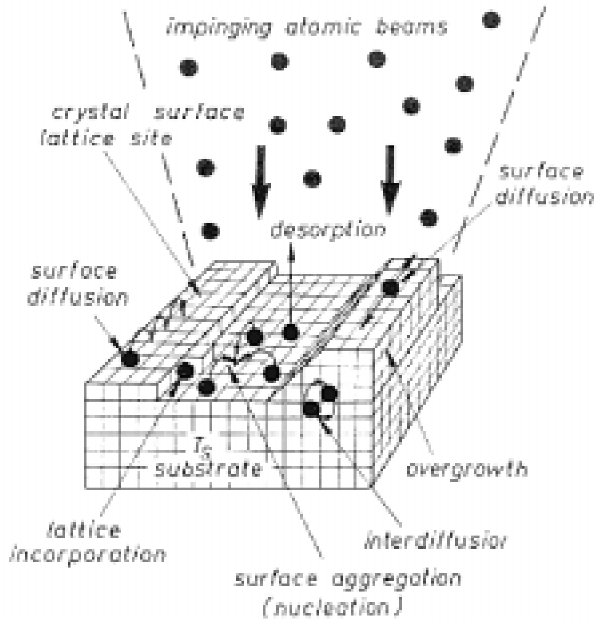

Fig. 3: Schematic illustration of the surface processes occurring during film growth by MBE [Her86].

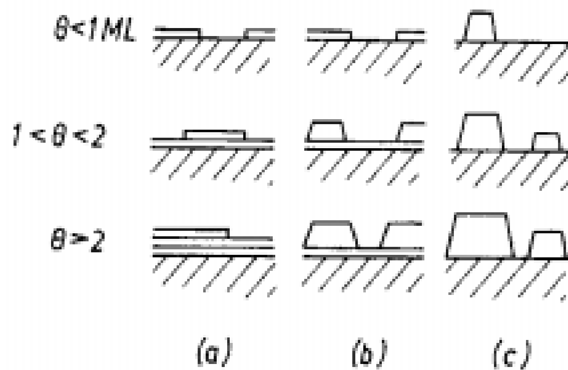

Fig. 4: Schematic representation of the three crystal growth modes (a) Layer-by-layer or Frank-van der Merwe; (b) layer plus island or Stranski-Krastanov; (c) island or Volmer-Weber mode. Θ denotes the coverage in monolayers [Ven84].

2.2.2 Lattice mismatch between epilayer and substrate

The surface of the substrate crystal plays a crucial role in the MBE growth process, because it influences directly the arrangement of the atomic species of the growing film through interactions between the outermost atomic layer of the surface and the adsorbed constituent atoms of the film. Generally, MBE epitaxy is a growth process of a solid film on a crystalline substrate in which the atoms of the growing film mimic the arrangement of the atoms of the substrate [Str82]. Consequently, the epitaxially grown layer should exhibit the same crystal structure and the same orientation as the substrate. This is true for epitaxial layers and structures of many practically important materials systems, i.e. GaAs/AlGaAs or CdTe/HgCdTe. However, the most frequent case of MBE growth is heteroepitaxy, namely, the epitaxial growth of a layer with a chemical composition and sometimes structural parameters different from those of the substrate. One essential issue of heteroepitaxy is associated to lattice mismatch. When lattice mismatch occurs, it is usually accommodated by structural defects in the layer or by strain connected with a relevant interfacial potential energy. In the simplest case, for instance, where the equilibrium interfacial atomic arrangements of the substrate and the overgrown epilayer have rectangular symmetry, and the epilayer is fairly thin in comparison to the thickness of the substrate crystal, the misfit may be quantitatively defined as [Mat75]

$$f_i = \frac{a_{si} - a_{oi}}{a_{oi}} \quad , \qquad i = x, y \quad , \tag{2.1}$$

where a is the bulk lattice constant, and s and o designate the substrate and the epitaxial layer, respectively. If a film is strained so that the lattices of film and substrate are identical at the interface, then the lateral misfit strain of the epitacial layer defined by

$$\varepsilon_i = \frac{a_{oi}^{str} - a_{oi}}{a_{oi}} \quad , \qquad i = x, y \tag{2.2}$$

will be equal to f_i. In Eq. 2.2, a_{oi}^{str} stays for the lateral atomic spacing in the strained epitaxial layer. If, however, the misfit is shared between dislocations and strain, then

$$f_i = \varepsilon_i + d_i \quad , \qquad i = x, y \quad , \tag{2.3}$$

where d_i is the part of the misfit accommodated by dislocations. A positive value for f implies that the misfit strain is tensile and that the misfit dislocations are positive Taylor dislocations, i.e. extra atomic planes lie in the epitaxial layer [Nab67].

It is known that if the misfit between a substrate and a growing layer is sufficiently small, the first atomic layers deposited will be strained to match the substrate and a perfectly matched epitaxial layer will be formed. For such a state the term "pseudomorphism" has been introduced [Fin34]. However, as the layer thickness increases, the homogeneous strain energy E_H becomes so large that a thickness is reached when it is energetically favorable for misfit dislocations to be introduced. The overall strain will be reduced but at the same time the dislocation energy E_D will increase.

The existence of the critical thickness for the generation of dislocations in the strained epitaxial layers was first discussed theoretically by Frank and van der Merwe [Fra49]. The basic assumption of the theory is that the configuration of the epitaxial system is the one of minimum energy. For a particular epitaxial layer-substrate crystal consisting of a semi-infinite substrate A and an epitaxial layer B of thickness t, the interfacial energy per unit area E_I will be [Bal83]

$$\begin{aligned} E_I = E_H + E_D = \tfrac{\mu t}{1-\nu}(\varepsilon_1^2 + 2\nu\varepsilon_1\varepsilon_2 + \varepsilon_2^2) \\ + \tfrac{\mu b}{4\pi(1-\nu)} \sum_{i=1}^{2} \left[\tfrac{|\varepsilon_i + f_{0,i}|}{\cos\gamma_i \sin\beta_i}(1 - \nu\cos^2\beta_i)\ln(\tfrac{\varrho R_i}{b_i}) \right] \quad , \end{aligned} \tag{2.4}$$

where μ and ν are the interfacial shear modules and Poisson's ratio, respectively; ε_i are the strains in the epitaxial layers defined by Eq. 2.2 ($i = 1, 2$); b is the magnitude of the Burgers vector characterizing the dislocation at the interface; $f_{0,i}$ is the natural misfit between the layer and the substrate; β and γ are the angles between the Burgers vector and the dislocation line, and between the glide plane of the dislocation and the interface, respectively; R_i stands for the cut-off radius of the dislocation which defines the outermost boundary of the dislocation's strain field, and ϱ is a numerical factor used to take the core energy of the dislocation into account. For the (001) interface of fcc structures, the misfits and lattice parameters will be identical with respect to the two perpendicular interfacial directions [110] and [1$\bar{1}$0]. In this case, since the homogeneous strains ε_1 and ε_2 are the same, i.e. ε_1=ε_2=ε, Eq. 2.4 can be simplified as

$$E_I = 2\mu t\varepsilon^2 \frac{1+\nu}{1-\nu} + \mu b \frac{(|\varepsilon + f_0|)(1-\nu\cos^2\beta)}{2\pi(1-\nu)\cos\gamma\sin\beta} \ln\left(\frac{\varrho R}{b}\right) \quad . \tag{2.5}$$

One should note that the homogeneous strain energy E_H is zero at zero strain (ε=0), while the dislocation energy E_D falls to zero at

$$f = \varepsilon + f_0 = 0 \quad , \tag{2.6}$$

which is the condition of pseudomorphism in the epitaxial layer-substrate system. The criterion for the critical thickness is [Ols75]

$$\frac{\partial E_I}{\partial |\varepsilon|} = 0 \quad \text{evaluated at} \quad |\varepsilon| = |f_0|_- \quad , \tag{2.7}$$

which gives the relation

$$t_c = \frac{b(1-\nu\cos^2\beta)}{8\pi\,|f_0|\,(1+\nu)\sin\beta\cos\gamma}\ln\left(\frac{\varrho t_c}{b}\right) \tag{2.8}$$

from which t_c can be calculated for given natural misfit f_0.

The calculated value of critical thickness do serve as a useful indication of the lower limit of the thickness at which misfit dislocations are introduced. There is no case recorded, so far, of misfit dislocations being introduced at the thickness below the critical thickness [Her89].

It is also possible to change the critical thickness of an epitaxial layer by growing one or more subsequent layers. E.g., if an epitaxial layer of B was deposited on substrate A, and the layer thickness t exceeded the critical thickness t_c, it might be possible in theory to restore coherency by the deposition of a cap layer with the same material as the substrate A [Ols75, Bas78]. It has also been shown [Bas78] that there is a second critical thickness of the layer B, above which it is not possible to restore coherence no matter how thick the top layer is grown. Furthermore, it has been revealed that the critical thickness in such single layer systems is directly correspondent to that in a multilayer system [Peo86]. This relation has been used to design the MBE growth of strained-layer superlattice structure, and for application in device technology [Osb87].

2.2.3 Crystallographic orientation of the substrate

Many experimental results comfirm that the crystallographic orientation of the substrate plays an important role in MBE growth. E.g. when III-V compounds are grown with MBE on III-V substrates, the substrate orientation influences considerably the incorporation process of dopants. This concerns the intentionally introduced dopants like Si in GaAs and AlGaAs/GaAs heterostructures, as well as the unintentionally incorporated contaminants like C in GaAs [Upp87, Wan86]. The orientation of the substrate surface influences also the opto-electronic properties of GaAs and the AlGaAs/GaAs heterostructures [Upp87]. This results from the difference in the band structure for different substrate orientations, and from the influence of the substrate orientation on the electrical compensation of the

dopants introduced into the heterostructure [Sub86, Vin86]. Drastic improvement in opto-electronic properties of the epitaxial layers grown on the GaAs (111)b surface has been achieved by slightly misorienting the substrates, i.e. 2^0 off towards the (100) orientation. Such misorientation introduces surface steps, and thus changes the growth mechanism. A schematic illustration is shown in Fig. 5. The effect of the substrate misorientation on the surface morphology and photoluminescence spectra of III-V layers on III-V substrates has been further demonstrated by growing AlGaAs layers on lenticular (planoconvex shaped) GaAs substrates with orientations close to (100) [Kra87]. It has been found that the smoothest areas, which simultaneously exhibited the narrowest photoluminescence lines were centered 6^0 off (100) towards the (111) A face, i.e. where growth occurred on monoatomic steps terminated by Ga atoms.

A strong influence of the substrate orientation on the growth parameters has also been demonstrated in MBE of narrow gap II-VI compounds [Siv87]. In this case the substrate orientation considerably influences the surface condensation coefficients [Mai70]. In order to fully understand the opto-electronic properties, it is important to analyze the structural properties of crystallographic misorientations, i.e. the geometry of chemical bonds on the substrate surface for different crystallographic orientations of crystals with the same bulk structure. Regarding to how the surface bond geometry may help to explain the orientational dependences of the MBE growth, more details are described in Ref. [Her89]. Here we only present some typical GaAs surface structures in Fig. 6. It shows schematically the geometry of surface bonds for some selected orientations of GaAs, which is the substrate material most frequently used for III-V MBE. Similar schematic illustrations may be constructed for other semiconducting crystals, showing the geometry of surface bonds when the orientation is changed [Wil62].

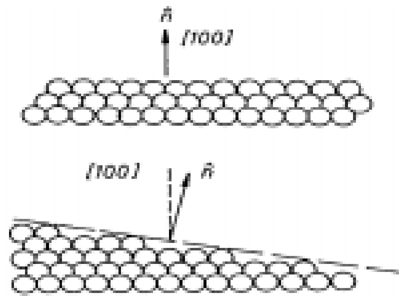

Fig. 5: Schematic illustration of how surface steps (lower case) occur, by slightly misorienting the (100) surface (upper case) of a substrate crystal

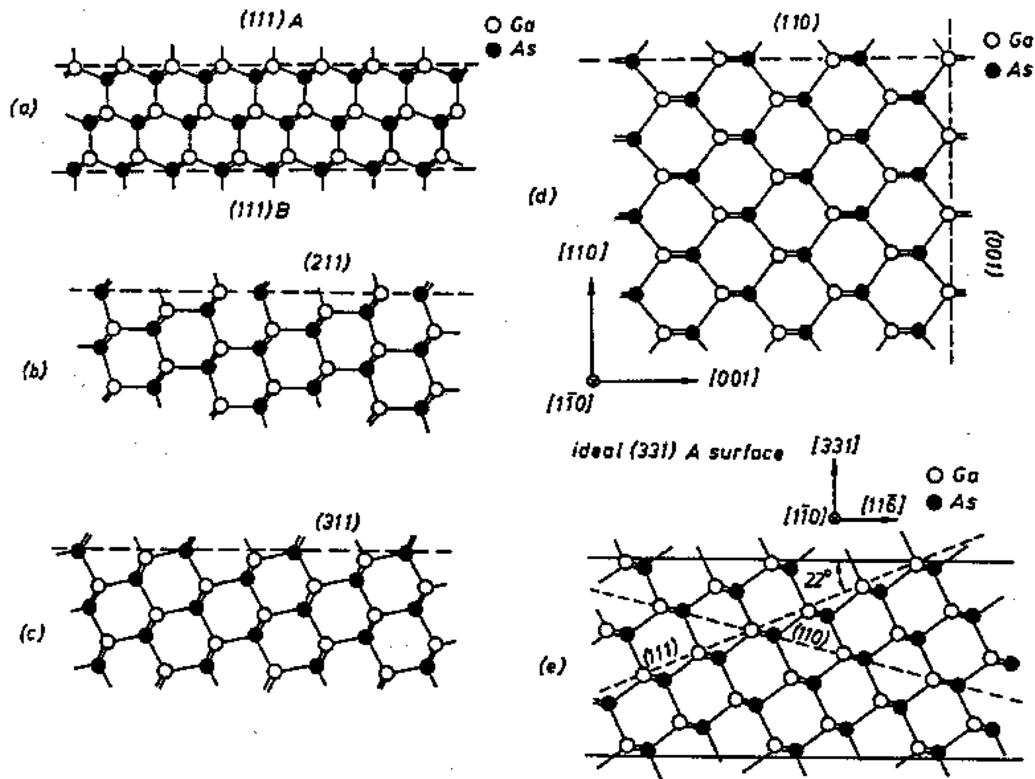

Fig. 6: Surface bonds for differently oriented GaAs substrate crystals. (a) (111) surface viewed along the $[01\bar{1}]$ direction, showing the A(Ga) and the B(As) faces. (b) (211) surface viewed along the $[01\bar{1}]$ direction. (c) (311) surface viewed along the $[01\bar{1}]$ direction. (d) a cross-section of the crystal lattice showing the planes (110) and (001). (e) The (331) surface viewed along the [110] direction [Upp87].

2.3 Self-assembling effect in MBE growth

Self-assembled epitaxial deposits which means spontaneous structural formation during the growth process, as observed in the strained layer and/or in step mediated growth on vicinal surfaces, is gaining an increasing interest because of the possibility of growing sophisticated low dimensional heterostructures, e.g. superlattices, quantum wires and QDs. Here, we just give an example concerning of self-assembled InAs QDs grown on GaAs substrate. Formation of homogeneous nanometer scale InAs dots on GaAs has been investigated e.g. with AFM preliminarily [Moi94, Mui95, Gru96]. The main features of the growth process can be summarized as following: [Moi94, Mui95, Gru96]
(i) the initial dots appear at the critical coverage of 1.75 ML of InAs at which the epitaxial layer is perfectly wetting the GaAs substrate (2D growth or Frank-van der Merwe mode).
(ii) the InAs used for forming the initial dots is provided by a sudden decrease of the InAs coverage in the 2D layer from 1.75 ML down to about 1.2 ML, i.e. nearly 1 ML of InAs strained to fit the GaAs substrate is changed into single crystal dots. This is the symptom of the self-assembled process in the strained epitaxial layer.
(iii) 2D-grown InAs coverage decreases further with growth of InAs above the critical coverage for the appearance of the initial dots, and vanishes around the coverage when coalescence of the dots occurs. This processing is actually a departure from the Stranski-Krastanov (SK) growth mode in which the 2D grown layer remains constant in coverage after transition to 3D growth mode.
(iv) coalescence and, hence, loss of homogeneity in the arrangement of the dots occurs when increased lateral sizes allow matter transfer by direct dot-to-dot bridging.

Moreover, the morphology of the InAs epitaxial layer observed with AFM together with PL data indicate that the self-assembled growth in the strained structures can be a simple and efficient way of building QDs [Moi94, Mui95, Gru96]. The average dot density can be varied between 10^9 and 10^{11} cm^{-2} [Leo93].

Growth mechanisms of self-assembled QDs has been proposed in Ref. [Leo93]. Here, we just summarize as following. At the start of deposition, the growth proceeds in a layer-by-layer fashion. With the buildup of strain, relaxation occurs by the formation of small coherent islands on the surface [Sny91]. With further deposition, the energy cost associated with adatom incorporation in a strained island is dictated by the size of the island. As a result, the larger islands (higher strain) tend to grow more slowly than smaller island [Cop89, Wak95] leading to some critical limits for dislocation formation. Growth beyond this critical point may cause some islands to relax by forming dislocations, which

then allows them to grow uninhibited by strain energies, causing the uniformity in sizes of the islands to severely degrade. Alternative explanations can be found from analytical models that consider energetics of island shape transitions [Bue86] or from treatments of island coarsening under elastic strain effects [Dae87]. Nevertheless, it is clear that under elastic strain effects and optimal kinetics, sharply peaked size distributions can be obtained. Specifically, various island size and number densities can be obtained by varying the strain (In content) and the growth kinetics (As pressure and substrate temperature) in the system. In the later chapter, we will discuss the structural properties of InAs QDs.

2.4 Reflection High Energy Electron Diffraction

In situ RHEED allows direct measurements of the surface structure of the substrate wafer and the grown epitaxial layers. It also allows observation of the dynamics for MBE growth. The scattering geometry of RHEED is appropriate for MBE, since the electron beam is at grazing incidence, whereas the molecular beams impinge almost normally on the substrate. Therefore, RHEED may be called an in-growth surface analytical technique.

RHEED is an electron diffraction technique which can yield information on surface structure, smoothness, and growth rate. Since the principle of diffraction theory on RHEED is similar to that in grazing incident x-ray case, we will introduce the grazing incident theory in Chap. 3. Here, we just show an experimental illustration and its applications on *in situ* MBE characterization. Fig. 7 shows an RHEED diffraction geometry. The diffraction of the incoming primary beam leads to the appearance of intensity-modulated streaks (or rods) normal to the shadow edge superposed on a fairly uniform background which is due to inelastically scattered electrons. As to the background knowledge of RHEED technique, please refer Ref. [Her89].

An example of RHEED pattern is shown in Fig. 8. For the rough surface in Fig. 8a, the diffraction pattern is produced in transmission through the surface asperities (3D island) and exhibits many spotty features. Fig. 8b, for the smooth surface with 2D islands, the diffraction pattern presents elongated streaks (surface truncation rods) normalized to the surface. This is due to the fact that the incoming beam can penetrate into the solid surface with restrictive to the uppermost layer of the crystal. In the case of 2D islands with finite size, the surface truncation rods are broadening. The intersection between the rods and Ewald sphere exhibits streak structure. Fig. 8c, for the ideal smooth surface, the width of the surface rods are quite narrow, like δ function. The intersection between

rods and Ewald sphere is a spot instead of Fig. 8b case.

It is evident that in all real systems atoms at and near a surface do not exhibit the same arrangement as in the bulk [Kah83]. The simplest arrangement is surface relaxation, whereby the topmost layers retain the bulk symmetry, but the atomic distances perpendicular to the surface are different from the bulk value [Rie85]. Surface reconstruction is a stronger disturbance giving rise to rearrangements of the topmost layers into symmetries different from the respective bulk crystal truncation case [Rie85]. As an example, Fig. 9 shows possible models for the $c(4\times4)$As surface, indicating how different coverage can originate the same surface structure. It is assumed that the As-As bond lengths are the same as the case in amorphous As, but the bond angles have been distorted [Lar83].

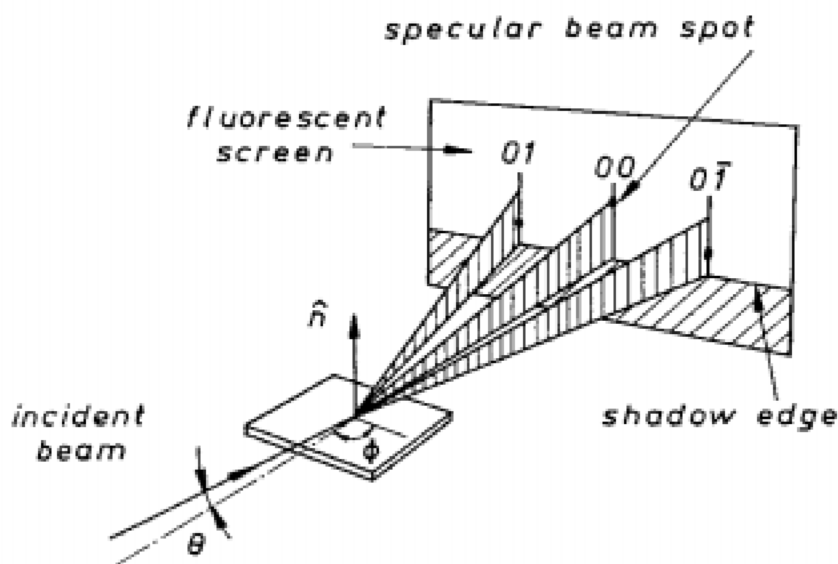

Fig. 7: Schematic diagram of RHEED geometry showing the incident beam at an angle θ to the surface plane. The azimuthal angle is φ. The elongated spots indicate the intersection of the Ewald sphere with 01, 00, and $0\bar{1}$ surface rods.

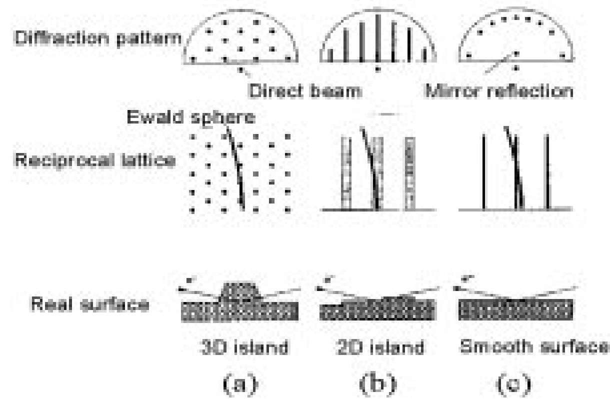

Fig. 8: Schematic illustration of RHEED pattern on different surface structures. (a) 3D island, (b) 2D island, (c) smooth surface.

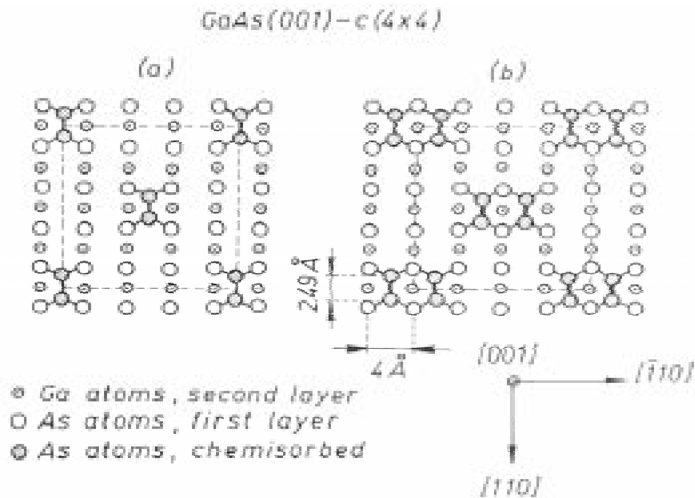

Fig. 9: Possible models for the $c(4{\times}4)$GaAs surface, based on a trigonally bonded excess As layer. (a) an additional 25% As coverage, (b) an additional 50% As coverage [Lar83].

RHEED pattern is a powerful tool to characterize these surface structures. An example is shown in Fig. 10. The reciprocal lattice sections for both $c(4{\times}2)$Ga and $c(8{\times}2)$Ga

structures together with the expected theoretical RHEED patterns in different azimuths are presented.

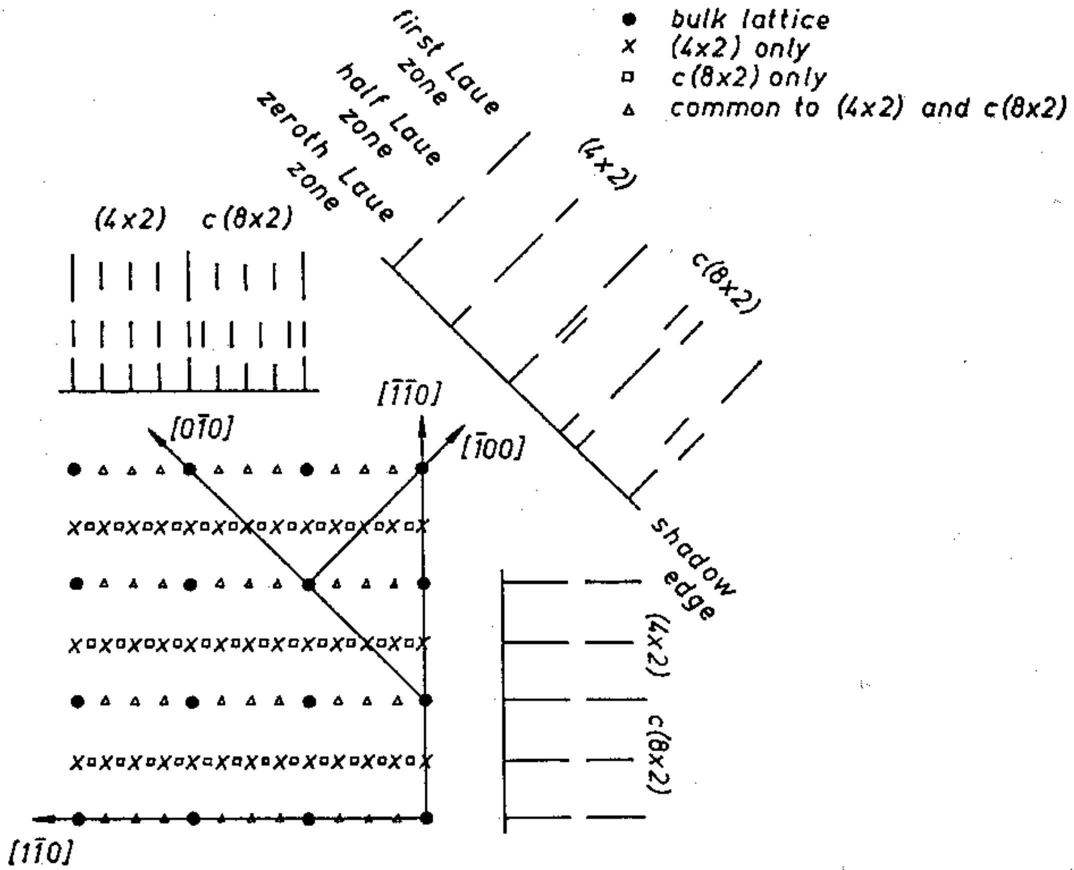

Fig. 10: Reciprocal lattice section showing $c(4{\times}2)$ and $c(8{\times}2)$ structures with the associated schematic RHEED patterns in different azimuths [Nea78]

Moreover, RHEED intensity oscillations of the specular beam play an important role for determining the thickness of layers or beam fluxes used in MBE growth. They provide a convenient method for the study of the mechanisms of crystal growth and for determination of the kinetics of surface diffusion under the conditions of MBE [Her89].

Chapter 3

Principle of X-ray Experimental Methods

3.1 In general

The X-ray technique is a tool for the characterization of the structural properties of solid crystals. This technique may provide us multiple information about the structure of the samples. A radiation wavelength in the order of the lattice constant allows the determination of atomic structures. In the present work, we employ the x-ray technique to investigate the semiconductor crystals, e.g. the ultra-thin films, and 3D single crystal islands with nanometer sizes on substrate surface, i.e. QDs. The x-ray experiments performed in the present work include:
i) X-ray topography, to detect crystal defects of substrate wafers; ii) GISAXS, to determine the ordering and shape of QDs grown by MBE; iii) GIXRD, to study the strain status inside QDs and possible intermixing structures; iv) GIXR, to study electron density induced surface and interface structures of the thin films; v) CTR, to reveal the crystalline structure at the interface of thin films; vi) XSW, to observe information about the positions of the adatoms (with respect to the lattice spacing of substrate lattice) and the atomic disorder at the surface and interface.

In particular, the penetration depth of the x-ray and corresponding structural information being gained from the scattering process may be varied by tuning the incidence angle of the x-ray in the grazing incident case. This allows depth sensitive investigations of the crystalline structure which are very valuable in layered structures.

3.2 Background of x-ray diffraction

3.2.1 X-ray optics

An ideal crystal lattice can be described as a periodic structure with a unit cell being formed by the three lattice vectors $\vec{a}$, $\vec{b}$ and $\vec{c}$. A translation in space by lattice vectors $\vec{r}_{mnp} = m\vec{a} + n\vec{b} + p\vec{c}$ from one unit cell in the lattice leads to a corresponding point in another unit cell. Here, m, n, and p are integers taking all values. In most cases, the unit cell consists of more than one atom. If there are atoms at positions $\vec{r_j} = m_{1j}\vec{a} + m_{2j}\vec{b} + m_{3j}\vec{c}$ with ($0 \leq m_i \leq 1$, i =1,2,3) and $0 \leq j \leq n$ in a unit cell containing n atoms we can describe the position of any atoms by $\vec{R_j} = \vec{r}_{mnp} + \vec{r_j}$.

An incident electromagnetic wave is scattered at atoms in different unit cells in the lattice, and interference effects lead to sharp reflections at well defined angular positions in a large distance from the sample due to the spatial periodicity of the structure. For a theoretical description of the scattering process it is very convenient to use the reciprocal lattice which is formed by the vectors,

$$\begin{aligned} \vec{a}^* &= \tfrac{2\pi}{v_0} \cdot \vec{b} \times \vec{c} \quad , \\ \vec{b}^* &= \tfrac{2\pi}{v_0} \cdot \vec{c} \times \vec{a} \quad , \\ \vec{c}^* &= \tfrac{2\pi}{v_0} \cdot \vec{a} \times \vec{b} \quad , \end{aligned} \tag{3.1}$$

where v_0 is the volume of the unit cell.

This definition leads to a periodicity in the reciprocal space with reciprocal lattice vectors

$$\vec{G} = H\vec{a}^* + K\vec{b}^* + L\vec{c}^* \quad , \tag{3.2}$$

with integers H, K and L (the Miller-index) denoting the lattice planes in the crystal. Regarding an incoming x-ray wave with a wave vector $\vec{k}$ striking two atoms having a distance $\vec{R}$, we get a phase shift $\vec{R} \cdot \vec{q}$ with $\vec{q} = \vec{k}' - \vec{k}$. $\vec{q}$ is the scattering vector and $\vec{k}'$ is the wave vector of the scattered wave. If $\vec{R}$ is lattice vector $\vec{r}_{mnp}$ in the real space we get constructive interference for

$$\vec{q} = \vec{G} \quad , \tag{3.3}$$

since $\overrightarrow{r_{mnp}} \cdot \vec{G}$=$2\pi$. Eq. 3.3 is the well known Laue-equation. This condition is illustrated in Fig. 11a. Fig. 11b shows the diffraction condition in the real lattice space, i.e.

$$2d_{HKL} \cdot \sin\theta = n\lambda \quad , \tag{3.4}$$

where λ is the wavelength of the incident and diffracted wave, d_{HKL} is the interplanar spacing of the lattice planes (HKL), θ is the incident and diffraction angle to the lattice planes, and n is the diffraction order. This is the well-known Bragg equation.

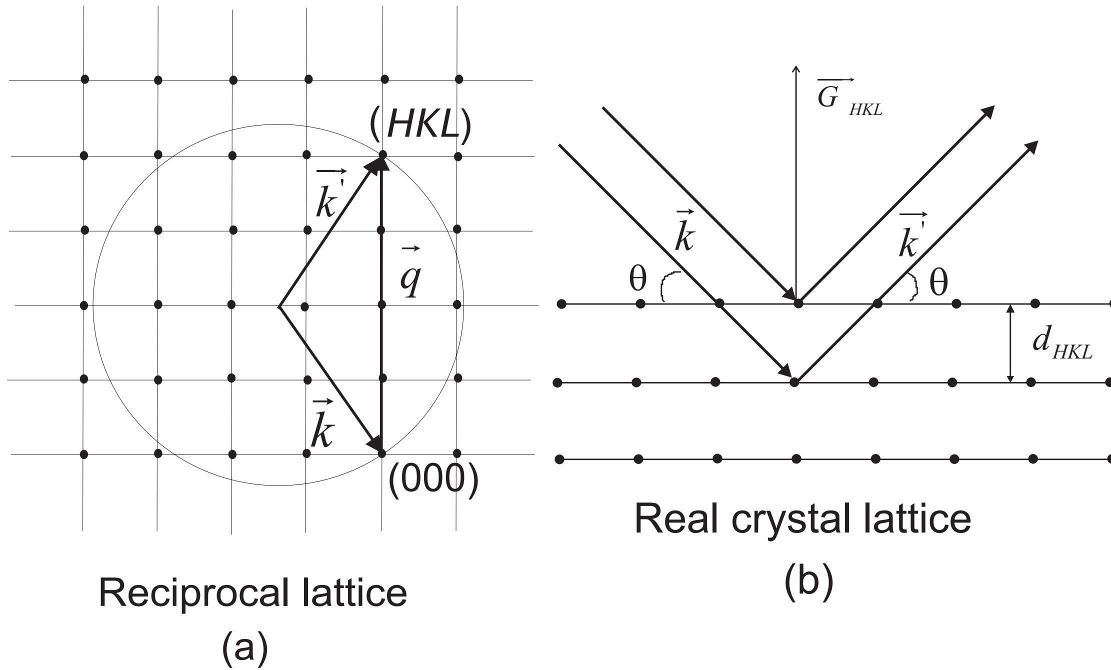

Fig. 11: (a) The Laue equation for the diffraction condition in reciprocal lattice space; (b) The Bragg equation for the diffraction condition in real crystal lattice.

3.2.2 X-ray diffraction intensity

First of all, we discuss the diffraction intensity for a single crystal cell. Since the scattering amplitude contribution from each atom inside the unit cell to the entire scattered amplitude can be added, the structure factor F_{HKL} defined for a Bragg diffraction with the scattering vector $\vec{q}$ is expressed in Eq. 3.5, leading to a quantitative calculation of

the diffraction intensity from a unit crystal cell.

$$F_{HKL} = \sum_{j=1}^{n} f_j(q) \cdot e^{i\overrightarrow{q}\cdot\overrightarrow{r}_j} \quad , \tag{3.5}$$

where $f_j(q)$ is the atomic scattering factor of the jth atom in the unit cell being a Fourier transformation of the electron density $\rho_j(\overrightarrow{r})$ of the atom:

$$f_j^0 = \int_{atom} \rho_j(\overrightarrow{r}) \cdot e^{i\overrightarrow{q}\cdot\overrightarrow{r}} d^3\overrightarrow{r} \quad . \tag{3.6}$$

Taking the dispersion $\Delta f'$ and absorption $\Delta f''$ effects into account, the atomic scattering factor f_j can be described as, $f_j = f_j^0 + \triangle f' + i\triangle f''$.

The diffraction intensity is defined as the square of the structure factor,

$$I = |F_{HKL}|^2 \quad . \tag{3.7}$$

The structure factor symbolize the scattering ability of x-ray from one unit crystal cell. It thus can be used to calculate diffraction intensity on a single crystal with finite volume. For further describing the diffraction process on a whole crystal, one should make some extensions.

The calculated diffraction intensity of the crystal can be expressed as

$$I_M = I_e \cdot F_{HKL}^2 \, |\Gamma|^2 \quad , \tag{3.8}$$

where I_M denotes the calculated diffraction intensity, I_e is a constant relevant to the incoming beam, $|\Gamma|^2$ is the diffraction function.

$$\Gamma = \sum_N e^{i\phi_{mnp}} = \sum_{m=0}^{N_1-1} e^{2\pi i m\xi} \sum_{n=0}^{N_2-1} e^{2\pi i n\eta} \sum_{p=0}^{N_3-1} e^{2\pi i p\zeta} \quad , \tag{3.9}$$

here, ϕ_{mnp} is the phase shift of the coherent scattering among the crystal cells. It is thus expressed as

$$\phi_{mnp} = 2\pi\overrightarrow{r}_{mnp} \cdot \overrightarrow{r}^*_{\xi\eta\zeta} = 2\pi(m\xi + n\eta + p\zeta) \quad , \tag{3.10}$$

where $\overrightarrow{r}^\star_{\xi\eta\zeta} = \xi\overrightarrow{a}^\star + \eta\overrightarrow{b}^\star + \zeta\overrightarrow{c}^\star$ is the coordinate vector in the reciprocal lattice space. ξ, η and ζ are the coordinate values in the reciprocal space, consisting of arbitrary real values close to the integer (H,K,L).

The diffraction function $|\Gamma|^2$ can be written as:

$$|\Gamma|^2 = \frac{\sin^2 \pi N_1 \xi}{\sin^2 \pi \xi} \cdot \frac{\sin^2 \pi N_2 \eta}{\sin^2 \pi \eta} \cdot \frac{\sin^2 \pi N_3 \zeta}{\sin^2 \pi \zeta} \quad . \tag{3.11}$$

Eq. 3.11 clearly indicates that the diffraction function can be used to express the corresponding diffraction intensity distribution in the reciprocal lattice space. The phase space with large diffraction intensity of the (H,K,L) Bragg spot corresponds to: $\xi = H \pm \frac{1}{N_1}$, $\eta = K \pm \frac{1}{N_2}$, and $\zeta = L \pm \frac{1}{N_3}$. As $\xi = H,\ \eta = K,\ \zeta = L$, i.e. in the case of exact Laue equation condition, (ξ, η, ζ) is located at the exact intensity maximum position. The corresponding maximum intensity value is,
$|\Gamma|^2_{max} = N_1^2 N_2^2 N_3^2 = N^2$. Therefore, the intensity maximum is proportional to N^2, and the corresponding integrated intensity is proportional to the number of unit cells in the crystal, i.e N value. Moreover, the full width at half maximum (FWHM) value of the intensity distribution is inversely proportional to the N value. From above, we conclude that the diffraction function is very sensitive to the contributing crystal size, and thus can be used in an intensity profile analysis. In the present section, we do not introduce the influence of the Debye_Waller factor to the actual intensity profiles, which in fact attenuates the diffraction intensity by an exponential factor due to atomic thermal and static vibrations around the lattice sites. More details of the diffraction intensity expression in some certain cases, are given in Ref. [War90].

3.3 Grazing Incidence X-ray Diffraction

GIXRD is a unique technique for the surface structural study, especially for the structural investigation of ultra-thin films with a few monolayers and interface characterization of buried structures. In comparison to the conventional x-ray diffraction technique, the grazing incidence can provide larger illuminated area of the incoming x-ray beam on the sample surface and thus highly increases the surface volume fraction which contributes to the x-ray diffraction intensity. Successes in developing surface x-ray diffraction methods which can exploit this advantage have resulted from separate attacks on the combined problems of surface sensitivity and surface specificity. An important factor in achieving the necessary surface sensitivity has been the development of synchrotron radiation source beamlines which provide extremely intense and highly collimated sources of x-rays, allowing one to deliver high x-ray fluxes to a surface and thus permitting to detect the weak surface scattering signals. The method of achieving surface specifity is based on two

different ideas. The first is in grazing reflection condition, an approach which is similar to the situation of RHEED. The physical basis of this approach in x-rays is, however, rather different. X-rays have a refractive index in solids which is smaller than unity, so if one approaches a surface at a sufficient grazing angle, total external reflection can be achieved. In this case the penetration is small, so any scattering signal is specific to the near surface region, even if the scattering signal is measured well away from the forward scattered geometry as, e.g. used in RHEED. A second approach to surface specificity is to make measurements in scattering geometries in which the surface scattered signal is significant but the substrate scattering is weak. One obvious example is when one has a reconstructed surface structure with a larger unit cell than that of the underlying substrate; in this case the diffracted beams associated with the surface superlattice (the fractional order diffracted beams) lie in scattering directions well away from the main substrate scattered beams.

The penetration depth of the x-ray into the sample is a dominant parameter, which can be controlled by the incident angle α_i. There is a limit for the incident angle, i.e. the total external reflection angle α_c, below which the refracted beam lies on the sample surface and the incident beam is totally reflected by the surface. The total external reflection angle can be calculated by Eq. 3.12

$$\alpha_c = (2.6 \times 10^{-6} \rho \lambda^2)^{1/2} \quad , \tag{3.12}$$

where the unit of α_c is radian, ρ is the mass density of the sample $(g \cdot cm^{-3})$. If $\alpha_i \leq \alpha_c$, the penetration depth t equals to

$$t = \lambda \Big/ \left[2\pi (\alpha_c^2 - \alpha_i^2)^{1/2} \right] \quad ; \tag{3.13}$$

If $\alpha_i > \alpha_c$, the penetration depth depends on the linear absorption coefficient $\overline{\mu}_l$,

$$t = 2\alpha_i \sqrt{\overline{\mu}_l} \quad . \tag{3.14}$$

As an example, we show the calculated penetration depth t of GaAs and InAs crystals as a function of the incident angle α_i in Fig. 12.

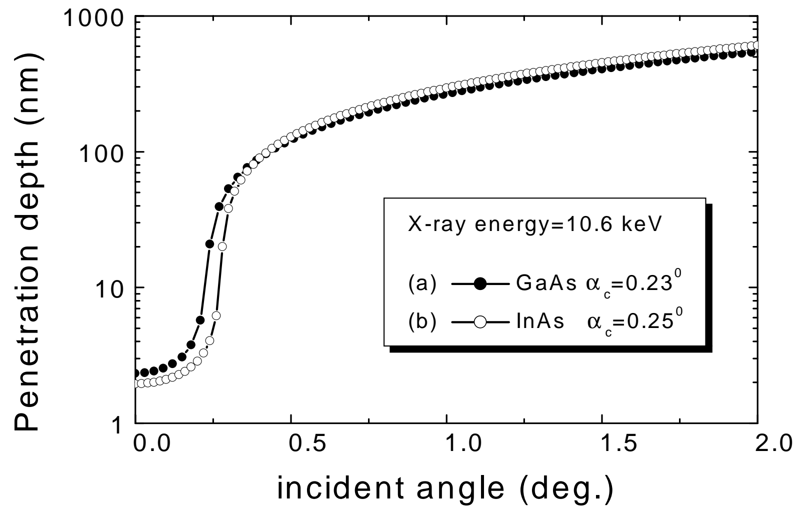

Fig. 12: The effective penetration depth of a grazing incidence x-ray beam into GaAs crystal (a) and InAs crystal (b) as a function of the incident angle. The energy of the incoming x-ray beam is of 10.6 keV, corresponding to a wavelength of 1.17 Å.

The grazing incidence geometry requires the highly collimated flux available from synchrotron radiation. It is also worth noting that the use of near critical angles of incidence is potentially important even when diffracted beams are measured at exited angles well separated from the position for the specular beam condition.

In order to maintain the surface specificity offered by critical incidence angle, surface x-ray diffraction studies are typically conducted at a fixed angle of incidence relative to the surface plane, diffracted beams being measured by a combination of sample azimuthal rotation and detector movement. Collecting a surface x-ray diffraction pattern at constant momentum transfer perpendicular to the surface is therefore a time consuming activity, and is rather demanding of the instrumentation if the very grazing incidence angle is to be kept strictly constant. In this case, the rigorous requirements of high precision positioning and rotating of the sample and detector in surface x-ray diffraction are a major design in the experiments.

As we know, an evanescent transmitted wave is generated when the x-ray beam strikes a crystal surface under a grazing angle. The transverse component (parallel to the surface) of the reflected beam may be attributed to the grazing incidence x-ray diffraction in case the Laue condition being satisfied with the lattice planes either perpendicular or tilted to the sample surface. We sketch both cases in Fig. 13. Fig. 13a illustrates a diffraction geometry of the incoming beam to the lattice plane perpendicular to the sample surface. We then call this case the in-plane diffraction, since the scattering vector is parallel to the sample surface, i.e. $\vec{q} = \vec{q}_{\|}$, while $\vec{q}_{\perp} \cong 0$. By using the conventional Bragg equation, the interplanar distance d_{HK0} can be calculated from the in-plane diffraction angle 2θ, characterizing the in-plane surface structure, e.g. the in-plane lattice constant. Besides this, the grazing incident case can also provide us out-of-plane structural information. Fig. 13b shows a situation, where the diffraction is contributed from lattice planes inclined relative to the sample surface. The scattering vector $\vec{q}$ is out of the surface plane leading to finite values for the projection on $\vec{q}_{\|}$ and $\vec{q}_{\perp}$ vectors. By analyzing both scattering vectors, the crystal lattice structure in horizontal and vertical directions can be achieved. Moreover, by combining both in-plane and out-of-plane GIXRD techniques, one can thoroughly investigate all Bragg spots found in the reciprocal lattice space. For clarity, we illustrate the Bragg diffraction condition by means of the Ewald sphere in the reciprocal lattice in Fig. 13c,d. The intersection between the Ewald sphere and reciprocal lattice is Bragg condition leading to the observed diffraction intensity. The scattering vector $\vec{q}$ (momentum transfer) in Fig. 13c is exactly in Laue condition, i.e. $\vec{q}_{HK0} = \vec{q}_{\|} = \vec{G}_{HK0}$ (Eq. 3.3), where $\vec{G}$ stands for the in-plane reciprocal lattice vector. Similarly, for the out-of-plane case the scattering vector $\vec{q}_{HKL} = \vec{G}_{HKL}$. Here we only show the simple schematic illustration of GIXRD, since the actually experimental performance is rather complicated. As to the detailed relation between the angular performance in real space and out-of-plane diffraction in the reciprocal space, please refer Ref. [Loh93]. Further applications of GIXRD technique on surface structural characterization are discussed in Ref. [Zab92].

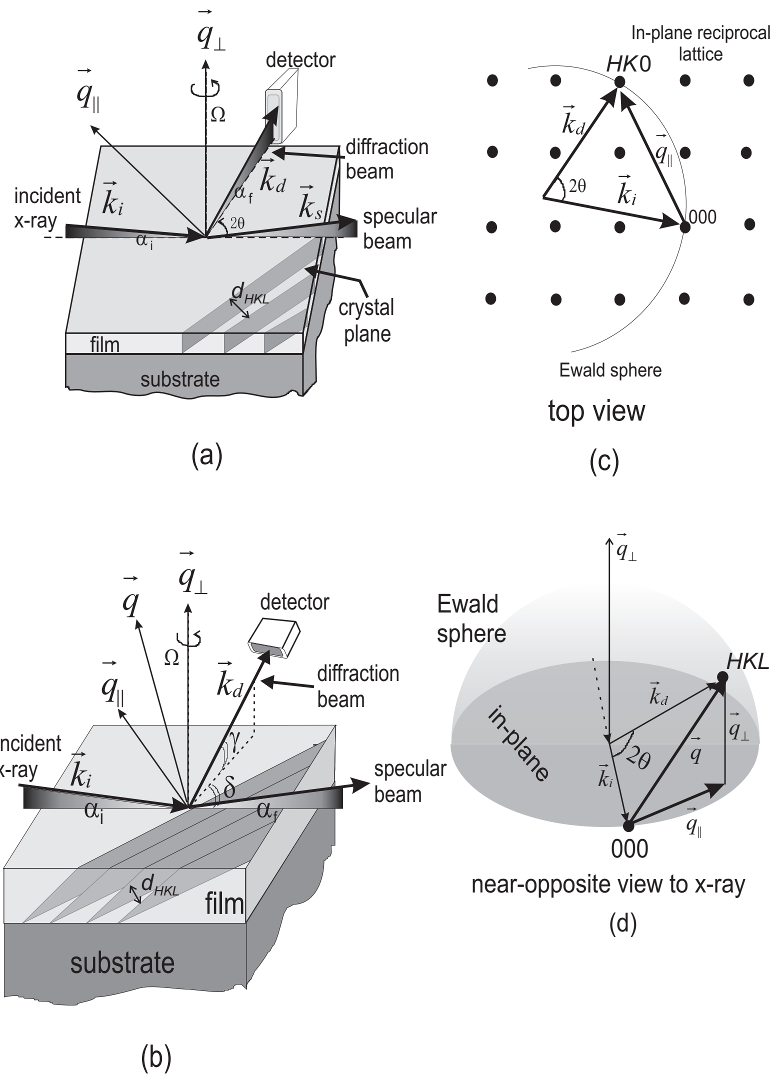

Fig. 13: Schematic illustration of GIXRD experiments. (a) In-plane GIXRD, the lattice plane perpendicular to the sample surface is attributed to the diffraction, $\vec{q}_{\perp} \cong 0$. (b) Out-of-plane GIXRD, the inclined lattice plane to the sample surface contributes to the diffraction with the scattering vector $\vec{q}_{\perp} \neq 0$. (c) Top view of the in-plane diffraction condition between the Ewald sphere and reciprocal lattice. (d) Near-opposite view to the incoming x-ray beam for out-of-plane Bragg diffraction in reciprocal space.

3.4 Grazing Incidence Small Angle X-ray Scattering

We apply GISAXS as a novel technique to investigate lateral ordering of self-assembled InAs QDs. In the following we will present this experimental method. We assume that the 3D dots are lateral randomly distributed with a short-range ordering. In the grazing incident case, we focus on scattering intensity observation off the specular beam position, where one can obtain the possible diffuse scattering intensity induced by the 3D dot distribution. The diffuse scattering intensity is symmetrically distributed at both sides of the specular beam. We then name it as satellite peaks. In a certain sample azimuthal orientation, the satellite peak intensity I can be expressed by [Wol97]

$$I(q_{||}) \propto \sum \frac{w}{w^2 + (q_{||} \pm q_0)^2} \quad , \tag{3.15}$$

where $q_{||}$ is the lateral diffuse scattering vector in the reciprocal space; $q_{||} = q_0$ is the satellite peak position; and w is FWHM of the satellite peak intensity. By analyzing the satellite peak profile, we derive two important parameters describing the lateral distribution of 3D dots, i.e. the mean dot-dot distance $\overline{d}$ and the standard deviation of the mean dot-dot distance $\langle \sigma/\overline{d} \rangle$, in which σ represents the average divergence of dot-dot distance with respect to the mean value of $\overline{d}$ [Wol97],

$$\begin{aligned} \overline{d} &= {}^{2\pi}/_{q_0} \quad ; \\ \langle \tfrac{\sigma}{\overline{d}} \rangle &= \sqrt{\tfrac{w}{2\pi q_0}} \quad . \end{aligned} \tag{3.16}$$

The standard deviation is very important to symbolize the divergence of the dot-dot distances in the direction parallel to the $q_{||}$, i.e. the sharpness of the dot-dot distribution. This parameter also yields a finite dot-dot correlation length and can be interpreted as coherent broadening. A quantitative determination of the correlation length from the satellite FWHM depends on the choice of the pair correlation function. For short-range order correlation we may use an exponential function of the type $exp(-r/l)$ [Sch98]. The correlation length l is then connected with the FWHM as, $l = 2/w$. We then use the Scherrer formula [War90] to treat the FWHM as due to finite sizes of crystalline domains. The average domain size L can be interpreted as a correlation length with [Sch98]

$$L = 0.9 \times 2\pi/w \quad . \tag{3.17}$$

A schematic illustration of GISAXS is shown in Fig. 14. Fig. 14a sketches the experimental setup. The incoming beam is parallel to y direction. α_i is the incident angle below the

total external reflection angle α_c; α_f is the reflection angle; Ω is the sample azimuthal oriented angle; The position sensitive detector (PSD) was mounted parallel to the sample surface, and perpendicular to the sample azimuthal direction. Fig. 14b sketches as dot distribution in a certain dot row which is perpendicular to the sample azimuth. Fig. 14c illustrates the intensity curve of the diffuse scattering from the dots in Fig. 14b. For the detailed introduction, please refer the caption of Fig. 14.

The importance noted here is that the sharpness of the dot-dot distribution is proportional to the correlation length, manifesting the ordering of the dot lateral distribution. The larger the correlation length, the higher the ordering. Moreover, the integrated intensity of the satellite peak is attributed to the displacements of the dots from their lattice-like sites determined from $\overline{d}$ values, e.g. sketched as open circles in Fig. 14b. The larger the displacement, the smaller the corresponding integrated intensity. The integrated intensity is decreasing by a factor of e^{-2M}, where M is proportional to the displacement of dots. This is similar to the Debye-Waller factor describing dynamic displacements of atoms in the crystal unit cell (see, Sec. 3.2.2). Assuming a square-like lattice for dot distribution, this factor expresses the static displacements of dots around their corresponding lattice sites.

In addition, the GISAXS experimental method provides us a way to determine the facet structure surrounding the dots [Son94, Son95, Wat95, Sch98]. By analyzing the intensity profile of crystal truncation rods (CTR) induced by the facet shape of dots, one can derive the average facet size and facet family, which are important parameters utilized for the calculation of electron structures.

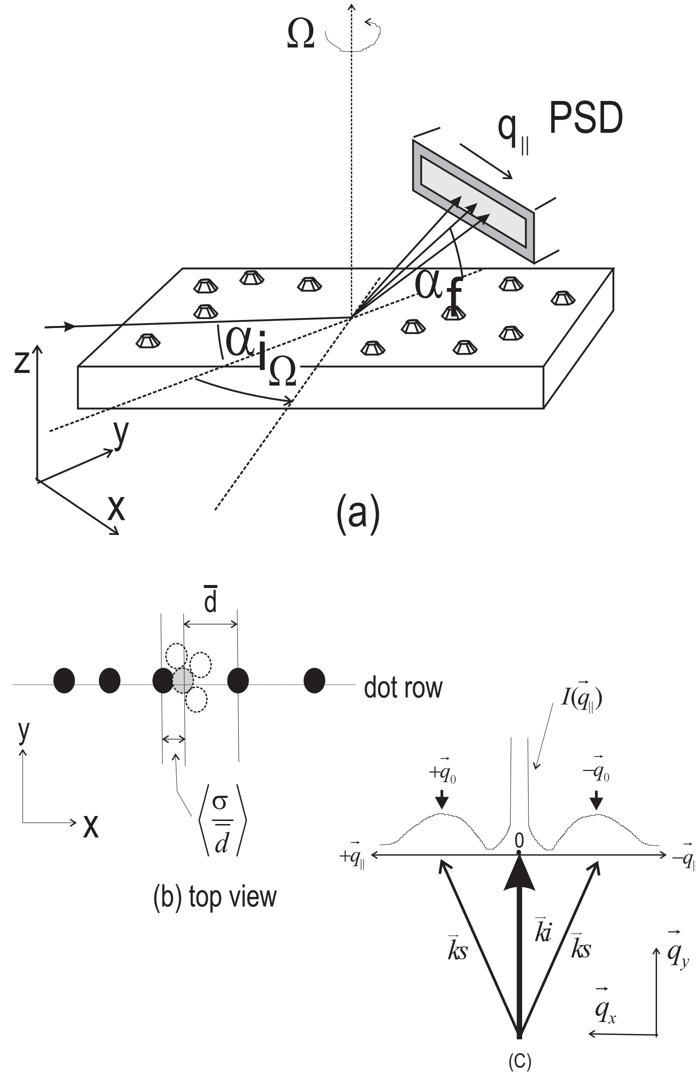

Fig. 14: Principle of GISAXS experiment. (a) The schematic illustration of GISAXS setup. (b) Top view of an schematic dot row. The mean dot-dot distance is $\overline{d}$, and the standard deviation of the dot-dot distance is $\langle\sigma/\overline{d}\rangle$. The dot row is parallel to $\overrightarrow{q}_{||}$ direction. open circles denote the displaced dots and a grey circle presents the lattice-like site. (c) The sketched intensity curve of diffuse scattering from the dots in (b). $\overrightarrow{k}_i$ is the incoming x-ray wave vector; $\pm\overrightarrow{k}_s$ is the diffuse scattering vector; $\pm\overrightarrow{q}_{||}$ is the momentum transfer, i.e. the scattering vector in the reciprocal space; $\pm\overrightarrow{q}_0$ is the satellite peak position. The illustrated intensity curve sums over the satellite peaks and the specular beam intensity.

3.5 Grazing Incidence X-ray Reflectivity

GIXR measurements provide a wealth of information on thickness and interfacial properties. In particular, GIXR is very sensitive to non-crystalline layers. This method is therefore well suited for the study of nano-structure thin films and superlattices. The GIXR experiment for multilayer systems was first described by Parrat [Par54], from which it is adequately explained by a recursive application of the Fresnel equation.

The refractive index may be expressed as a function of the magnitude of the scattering vector, $|\overrightarrow{q}_0| = \left|\overrightarrow{k}_{0,f} - \overrightarrow{k}_{0,i}\right| = q_0$, [Par54]:

$$\begin{aligned} n(q_0) &= 1 - \tfrac{2\pi r_0}{k_0^2} \sum_i \left[f_i(q_0) + \Delta f_i\right] - \tfrac{i\mu}{2k_0} \quad , \\ &= 1 - \delta - i\beta \quad , \end{aligned} \tag{3.18}$$

where $\left|\overrightarrow{k}_{0,i}\right| = \left|\overrightarrow{k}_{0,f}\right| = k_0 = {}^{2\pi}/_{\lambda}$ is the vacuum wave-number for elastic scattering, r_0 is the classical electron radius (0.2818×10^{-5} nm), $f(q_0)$ is the atomic form factor (in the present grazing incident case, it equals to the atomic number Z), Δf takes dispersion corrections of δ into account, and μ is the mass absorption coefficient. Since the real part δ is positive and on the order of 10^{-5}, total external reflection of the x-ray beam penetrating into a medium of higher electron density of ρ_e occurs at the critical scattering vector:

$$q_c^2 = 16\pi\rho_e r_0 = 4k_0^2(1 - n^2) \quad , \tag{3.19}$$

where q_c is a property of the materials. Assuming a specular reflectivity configuration in which a collimated x-ray beam impinges from the vacuum side onto an extended flat surface of a material and the scattering vector is normal to the physical surface, the incident and exit angles α_i and α_f of the beam to the surface are identical and the scattering vector is given by $q_0 = 2k_0 sin(\alpha)$. Inside of the material the scattering vector is changed according to $q_1^2 = q_0^2 - q_c^2$. For $q_0 < q_c$, q_1 becomes imaginary and the transmitted wave is exponentially damped in the material with a characteristic penetration depth of Δ_{eff} being $\lim_{q \to 0} \Delta_{eff}(q_0) = \frac{1}{q_c}$. $\Delta_{eff}(0)$ is in the order of 2 to 5 nm depending on the electron density of the materials. For $q_0 > q_c$, $\Delta(q_0)$ is mainly determined by the photoelectric absorption.

In the case of thin films and superlattices one has to deal with several or many interfaces. The boundary conditions must be fulfilled at each individual interface and the reflectivities and transmittivities add together to provide an overall reflectivity for a stratified medium.

The reflectivity may then be calculated by the optical transfer matrix method or by the recursion scheme described by Parrat [Par54]. Here, we discuss the latter case.

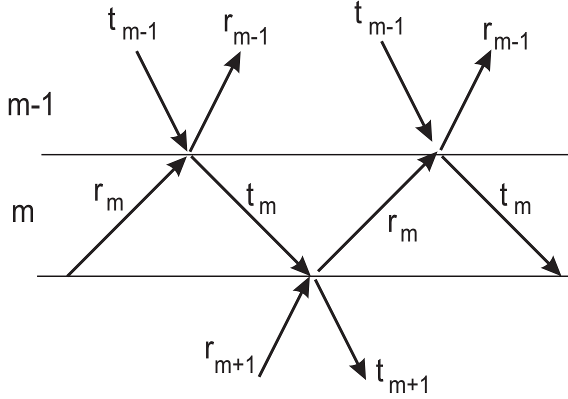

Fig. 15: Reflection and transmission of waves occurs at all interfaces separating regions of different electron densities in a layered material. r_m and t_m are the amplitudes of the reflected and transmitted electrical field vectors, respectively.

As shown in Fig. 15, t_m and r_m are the amplitudes of the electric field transmitted and reflected in medium, respectively. Moreover, we define a phase factor for the field in between two interfaces:

$$a_m = e^{iq_m d_m/2} \quad , \tag{3.20}$$

where d_m is the thickness of the mth layer, q_m is the scattering vector in the medium. Continuity of the transverse component of the electric field vector at the interface between m and $m-1$ medium layers is:

$$t_{m-1}a_{m-1} + r_{m-1}a_{m-1}^{-1} = t_m a_m^{-1} + r_m a_m \quad , \tag{3.21}$$

and continuity of the electric field gradient:

$$(t_{m-1}a_{m-1} - r_{m-1}a_{m-1}^{-1})q_{m-1}/2 = (t_m a_m^{-1} - r_m a_m)q_m/2 \quad . \tag{3.22}$$

Solution of these two equations is achieved by taking their difference and dividing it by the sum to be,

$$\Re_{m-1} = a_{m-1}^4 \left[\frac{R_{m-1,m} + \Re_m}{R_{m-1,m}\Re_m + 1} \right] \quad . \tag{3.23}$$

In Eq. 3.23,

$$\Re_m = \tfrac{r_m}{t_m} a_m^2 \quad ,$$
$$R_{m-1,m} = \tfrac{q_{m-1}-q_m}{q_{m-1}+q_m} \quad , \tag{3.24}$$

where $\Re$ is a generalized Fresnel reflectivity for the interface between m and $m+1$, and $R_{0,1}$ is the usual Fresnel coefficient for a smooth surface.

For deriving the reflected intensity of a stratified medium, a recursion method is applied, starting with the lowest layer (substrate crystal), which is assumed to be infinitely thick so that $\Re$ equals to 0, and then going to the top surface. The reflected intensity I_R is expressed as,

$$\frac{I_R}{I} = |\Re_0|^2 = R_F = \left[\frac{q_0 - q_1}{q_0 + q_1}\right]^2 \quad , \tag{3.25}$$

where I is the intensity for the incoming beam in the medium. The Parrat formalism has the advantage of providing the correct expression for all regions of scattering, because no approximation is made. The absorption is automatically taken into account, and any density profile can be modeled by slicing the material in an arbitrary number of thin layers. Fig. 16 shows typical GIXR intensity curves for a film structure like, 10nm GaAs/1 ML InAs/GaAs substrate. The reflectivity exhibits a critical scattering vector q_c, below which the intensity is constant. As $q > q_c$, the reflectivity drops off approximately with q^{-4}, which is usually referred to as Fresnel reflectivity. It also shows the interference fringes above q_c, i.e. an intensity oscillation, which is primarily due to the interference of waves scattered from the surface and from the interface between the GaAs film and InAs monolayer. The periodicity Δq of the oscillation curve is originated from the film thickness with the relation of $T_{thickness} = 2\pi/\Delta q$. While at the oscillation maxima a large fraction of the incoming beam intensity is reflected, at the minima the waves are being trapped within the film boundaries and form standing waves. At the minima, the film acts as a wave guide and a high electric field is set up, leading to a high probability for atomic excitations. Therefore, the fluorescence radiation is expected to have maxima at the positions where the reflectivity exhibits minima.

Considered that the interfaces exhibit roughness with an atomic scale due to intermixing and interdiffusion, the deviation from an abrupt interface affects the q dependence of the reflectivity, which drops off faster as compared to an ideally sharp interface. Assuming the electron density across an interface between $m-1$, and m has a Gaussian shape with a width of σ, the attenuation can be described according to Nevot and Croce [Nev80], by a factor like a static Debye-Waller factor,

$$R_{m-1,m}(\sigma) = R_{m-1,m}(0)e^{-q_0^2\sigma_{m-1,m}^2} \quad . \tag{3.26}$$

As to non-Gaussian roughness, the electron density may be approximated by slicing the interface into thin slabs of varying electron density.

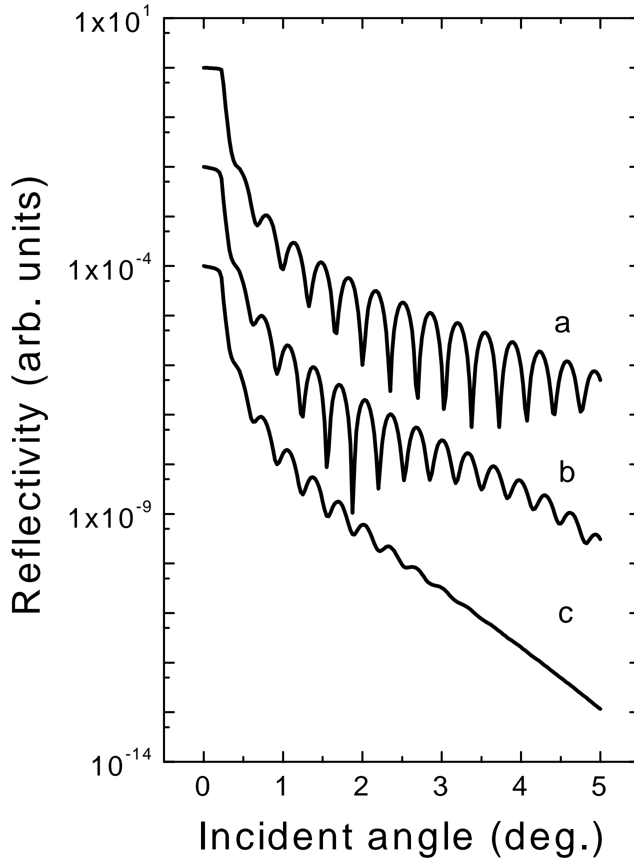

Fig. 16: Calculated reflectivities from a buried InAs δ layer (1 ML) with a 10 nm-thick GaAs cap layer on a GaAs substrate using the Parrat formalism, i.e. sample structure as GaAs cap/InAs δ/GaAs substrate. (a) reflectivity curve without surface and interface roughness. (b) reflectivity curve for 2.5 Årough surface and smooth interface. (c) reflectivity curve for 2.5 Årough surface and 5 Årough interface. For clarity, the lower curves are displaced by two orders of magnitude.

Now, we present a more complex electron density profile for the reflectivity of thin films. In the kinematical approach the reflectivity of an electron density profile $g(z)$ perpendicular to the sample surface is described by the well-known Master-Formula [AN87]

$$R(q_\perp) = R_F \cdot \left| \int g^{'}(z) \cdot e^{iq_\perp z} dz \right|^2 \quad , \tag{3.27}$$

where R_F is the Fresnel reflectivity of the bulk materials and $g^{'}(z) = dg/dz$ is the gradient of the electron density profile. However, the main deficiency of this method is that the absorption effects in the materials are not taken into accounted.

For a rough surface the transmittivity is larger than that for a smooth surface, enhancing the intensity of the interference fringes at certain angles, see Fig. 16b. Vice versa, for

a smooth surface because of its high reflectivity the transmittivity is smaller, reducing the amplitude of the intensity oscillation. In the case of both surface and interface being rough, the reflected intensity drops off drastically with increasing q and the amplitudes of the Fringes are highly damped, see Fig. 16c.

3.6 Crystal Truncation Rods

In the case adatoms form a single layer with a larger surface lattice than the substrate, but produces no reconstruction or distortion of the substrate atom positions, the structural information available from fractional order beams is only the relative location of the adsorbate atoms within this layer. This may require the measurement of crystal truncation rods (CTR). In the following we briefly introduce this experimental method.

The surface CTR exists on the semi-infinite crystal surface. The rod intensity can be regarded as the scattering from a single atomic layer and expressed as a evolution from Eq. 3.8 and Eq. 3.11 assuming the infinite number of unit cells N_1 and N_2 parallel to the surface [Rob86].

The rod intensity is very sensitive to the surface crystal roughness, by which it is highly damped along surface normal, i.e. along q_3 away from its Bragg condition. This can be understood with following simple model. If a partial layer of atoms is added to the surface, in such a way that they occupy sites that are a continuation of the bulk lattice, there will be interference between the two-dimensional diffraction pattern of the layer and the ideal CTR of the rest of the crystal. A convenient way to model roughness is to extend more than one layer, i.e. a fractional occupancy β with $0 < \beta < 1$ is given to the first added layer, β^2 to the second, and so on. The distribution of atoms within each layer is assumed to be terraced structure whose lateral extent is smaller comparing to the coherence length of the x-rays. The diffraction intensity can be expressed as,

$$I_{HK} = F_{HK}^2 N_1^2 N_2^2 \frac{(1-\beta)^2}{[1+\beta^2-2\beta\cos(q_3 c)]} \frac{1}{4\sin^2(\frac{1}{2}q_3 c)} \quad , \tag{3.28}$$

It is convenient to express the surface roughness as a root-mean-square value of the surface contour,σ_{rms}. The relation is,

$$\sigma_{rms} = \frac{\beta^{1/2}}{(1-\beta)} d_{\perp} \quad , \tag{3.29}$$

where $d_\perp$ is the lattice spacing perpendicular to the surface. This formula is specific to the model and will give an inaccurate measure of the surface contour if there are significant components of vibration or disorder. From above, we conclude that for a perfect crystal with a flat surface, the intensity of the CTR decays proportionally to about $\frac{1}{\Delta q^2}$, with $\Delta q = q - G_{HKL}$ denoting the distance to the Bragg condition in the reciprocal space. For the case of a rough surface the intensity drops more rapidly with increasing Δq.

Considered the case of a thin film grown on top of the substrate, an intensity oscillation becomes visible along the CTR due to the difference between the scattering vectors resulted from the substrate and from the thin film [Fal98]. The period of the oscillation is proportional to the reciprocal thickness of the film. As in the case of surface and interface roughness, the presence of interface roughness leads to a reduction of the CTR intensity and a damping of the amplitude of the oscillation with increasing $|\Delta q|$. A different lattice constant of the film leads to a second Bragg peak appearing near the substrate Bragg peak in the reciprocal space. The presence of a buried δ layer under a capping layer, identical to the substrate in material and structure, leads to CTR intensity oscillations with a periodicity corresponding to the reciprocal thickness of the top layer. These oscillations result from a phase shift between x-ray diffracted from the substrate and from the top layer, due to the presence of the δ layer with a different lattice constant.The CTR is asymmetric with respect to the substrate Bragg condition. The asymmetry of the oscillation is a general feature for CTR of a δ layer. The exact shape of the CTR, however, strongly depends on the lattice constant and scattering vector of the δ layer. Fig. 17 shows a schematic CTR principle from a buried δ layer structure.

The CTR intensity has been calculated by summing the intensities from the top layer, δ layer and the substrate, within the kinematical theory [Rob88],

$$
\begin{aligned}
I(q) = const.|&e^{-\Delta q^2 \sigma_{top}^2} f_{top}(q) \tfrac{1-e^{iqa_{top}N_{top}}}{1-e^{iqa_{top}}} \\
&+e^{-\Delta q^2 \sigma_{\delta}^2} f_{\delta}(q) e^{iqa_{top}N_{top}} \tfrac{1-e^{iqa_{\delta}N_{\delta}}}{1-e^{iqa_{\delta}}} \\
&+e^{-\Delta q^2 \sigma_{sub}^2} f_{sub}(q) \tfrac{e^{iq(a_{top}N_{top}+a_{\delta}N_{\delta}+a_{\delta}-a_{sub})}}{1-e^{iqa_{sub}}}|^2 \quad .
\end{aligned}
\tag{3.30}
$$

$f(q)$ represents the structure factor including the temperature dependent Debye-Waller factor in each layer. The structure factor of the δ layer is assumed to be $f_\delta = xf_{adatom}(q)+(1-x)f_{sub}(q)$, x denotes the concentration of the adsorbate atoms in the δ layer. $q = 4\pi sin(\theta)/\lambda$ is the scattering vector of the incoming wave and diffracted wave, which is normal to the sample surface. The number of lattice planes of the top layer and δ layer

are denoted as N_{top} and N_δ, respectively. a_{top}, a_δ, and a_{sub} are the lattice spacings for the top layer, the δ layer, and the substrate layer. The roughness σ in each layer is indexed as σ_{top}, σ_δ, and σ_{sub} which are denoted from Eq. 3.29, correspondingly. Eq.3.30 is a very important formula which can be used to determine the structural information of a buried layer, i.e. the thickness of the top layer and δ layer; the surface and interface roughness of crystals; the actual lattice constant for each layer; and intermixing (stoichiometry) in the layers.

Fig. 18 shows the CTR intensity curves calculated by three different crystal models. (a), the CTR curves result from the surface of a semi-infinite crystal with smooth and rough surfaces. (b), the CTR oscillation curves contributed by a thin film on the substrate are indicated. (c) the CTR curves are associated to the buried δ layer and top thin layer, from which we observe the asymmetric CTR oscillation comparing to the (b) case. For above three cases, the existence of a rough surface and/or interface leads to the CTR intensities being significantly decreased and the oscillation being damped along with scattering vector q away from the Bragg condition.

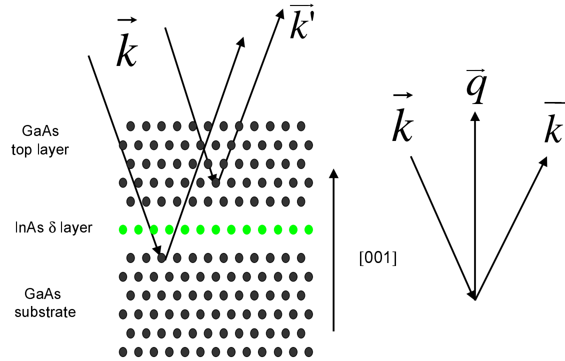

Fig. 17: a schematic illustration of buried InAs δ layer capped by GaAs (001)layer. The incoming wave vector is $\overrightarrow{k}$ and the diffracted wave vector is $\overrightarrow{k}'$. The corresponding scattering vector (momentum transfer) q is normal to the sample surface, i.e. along [001] direction.

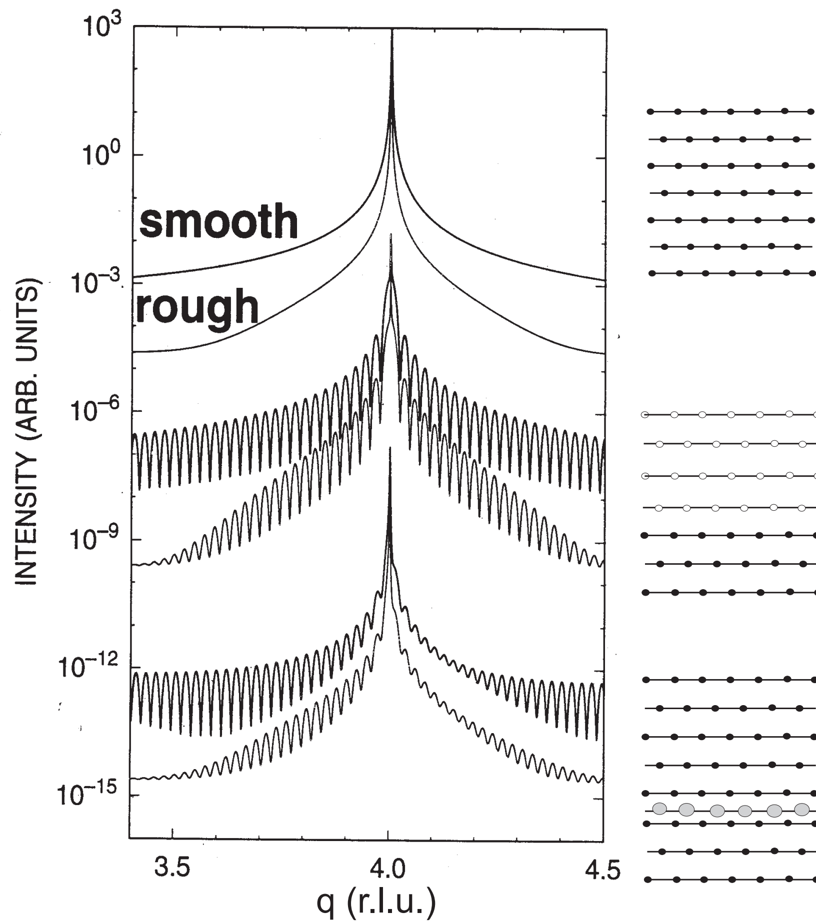

Fig. 18: Schmatic illustration of CTR model calculations for (004) Bragg diffraction . (a) is for the crystal surface CTR, (b) shows the CTR oscillations of a thin film grown on substrate, (c) is for the buried δ layer. The crystal structure is shown schmatically on the right side.

3.7 X-Ray Standing Waves

XSW method of surface structure determination using x-ray scattering is based on the fact that when a Bragg diffraction condition is established in a crystal, the interference between the incident and scattered x-ray beams generates a standing x-ray wavefield in the crystal with an intensity period which is equal to the scattered plane spacing. There is a finite range of the scattering conditions over which the standing wavefield is established; within this range, the phase of the standing wavefield relative to the substrate planes shifts in a systematic fashion by one-half of its periodicity such that the antinodal planes of the wave move from being directly on the substrate planes to midway between them.

The existence of this effect means that if one measures the absorption of the x-ray wavefield at specific atoms as a function of the scattering condition throughout the standing wave range, it is possible to determine the location of these x-ray absorbing atoms relative to the substrate planes. Now, we describe the basis theory of the x-ray standing waves [Zeg93].

We assume that two x-ray waves exist in such a way that they are planar and linearly polarized in parallel direction. The latter requirement is not necessary but convenient since we can omit vector symbols. The first wave is characterized by the complex amplitude ϵ_1 of the electric field of the electromagnetic wave

$$\epsilon_1 = E_1 e^{2\pi i(\nu_1 t - \overrightarrow{k} \cdot \overrightarrow{r})} \quad . \tag{3.31}$$

Here ν_1 is the frequency of the radiation. $\overrightarrow{k}$ the propagation vector of the wave and $\overrightarrow{r}$ a coordinate vector with respect to an origin. The second wave ϵ_2 is defined in the same fashion as

$$\epsilon_2 = E_2 e^{2\pi i(\nu_2 t - \overrightarrow{k}' \cdot \overrightarrow{r})} \quad . \tag{3.32}$$

Note that we relate the magnitudes of the propagation vector $\overrightarrow{k}$ to the wavelength λ via $|\overrightarrow{k}| = \lambda^{-1}$. Moreover, assuming $\nu_1 = \nu_2 = \nu$, then we get

$$\left|\overrightarrow{k}'\right| = \left|\overrightarrow{k}\right| = \frac{c}{\nu} \quad , \tag{3.33}$$

where c is the speed of light. The amplitudes E_1 and E_2 are also complex numbers, i.e. they contain a phase factor as well. Since we assume ϵ_1 and ϵ_2 to be coherent, we can write

$$E_2 = \sqrt{R} E_1 e^{iv} \quad , \tag{3.34}$$

where $\sqrt{R}$ relates the amplitude of E_2 to E_1, and υ defines the phase relationship of E_2 to E_1. Coherence means here that υ is independent of time and space. Here,

$$R = \frac{I_2}{I_1} = \frac{|E_2|^2}{|E_1|^2} \quad . \tag{3.35}$$

The phase υ can be expressed as

$$\begin{aligned} \upsilon &= \varphi, \qquad &for \ \mathrm{Re}(E_2/E_1) > 0, \\ \upsilon &= \varphi + \pi, \qquad &for \ \mathrm{Re}(E_2/E_1) < 0, \end{aligned} \tag{3.36}$$

where $\varphi = \arctan[\ \mathrm{Im}(E_2/E_1)/\mathrm{Re}(E_2/E_1)]$. An x-ray standing wave via superposition of ϵ_1 and ϵ_2 is generated. This leads to the total wavefield

$$\begin{aligned} \epsilon = \epsilon_2 + \epsilon_1 &= \sqrt{R} E_1 e^{i\upsilon} e^{2\pi i(\nu t - \overrightarrow{k}' \cdot \overrightarrow{r})} + E_1 e^{2\pi i(\nu t - \overrightarrow{k} \cdot \overrightarrow{r})} \\ &= |E_1|\, e^{2\pi i(\nu t - \overrightarrow{k} \cdot \overrightarrow{r})}(1 + \sqrt{R} e^{i(\upsilon - 2\pi \overrightarrow{q} \cdot \overrightarrow{r})}) \quad , \end{aligned} \tag{3.37}$$

where $\overrightarrow{q} = \overrightarrow{k}' - \overrightarrow{k}$, normal to the wavefield planes. Here, E_1 is substituted by $|E_1|$. For the normalized intensity $I = \epsilon\epsilon^*/|E_1|^2$, we then obtain the intensity expression,

$$\begin{aligned} I &= \left|1 + \sqrt{R} e^{i(\upsilon - 2\pi \overrightarrow{q} \cdot \overrightarrow{r})}\right|^2 \\ &= 1 + R + 2\sqrt{R} \cos(\upsilon - 2\pi \overrightarrow{q} \cdot \overrightarrow{r}) \quad . \end{aligned} \tag{3.38}$$

The superposition of the two coherent plane waves creates a planar standing wave. The particular pattern of this wave determined by $\overrightarrow{q}$ and the phase υ is the intensity at a particular location of $\overrightarrow{r}$ in space. In the direction parallel to $\overrightarrow{q}$ the intensity is maximum and zero in the direction normal to $\overrightarrow{q}$.

In order to understand the phase shift in the XSW field generated at Bragg diffraction case, requirements of dynamic theory of x-ray diffraction need to be presented here briefly. For a thorough description of this theory, please refer Ref. [Bat64]. The basic assumption of the dynamic theory of x-ray diffraction is that, the conductivity is zero at x-ray frequencies so that there is no resistive heat loss and that magnetically the crystal has the same behavior as vacuum space, i. e. $\mu = \mu_0$. In this way, the well known Maxwell's equations are used,

$$\begin{aligned} \nabla \times \overrightarrow{E} &= -\mu_0 \tfrac{\partial}{\partial t} \overrightarrow{H} \quad , \\ \nabla \times \overrightarrow{H} &= \tfrac{\partial}{\partial t} \overrightarrow{D} \quad , \end{aligned} \tag{3.39}$$

where $\overrightarrow{E}$, $\overrightarrow{H}$ and $\overrightarrow{D}$ are the electric field, magnetic field and electric displacement vector, respectively. From the solution at the Bragg diffraction case, the ratio of the complex amplitudes E_1 and E_2 for the incident and reflected waves is given as,

$$E_2/E_1 = (\chi_n/\chi_{\overline{n}})^{1/2} \left[\eta \pm (\eta^2 - 1)^{1/2}\right] \quad , \tag{3.40}$$

which is for the case of a symmetrical reflection. It indicates that the incident angle and the reflected angle with respect to the crystal surface are the same. Here, σ-polarized x-rays, i.e. the E-field vectors of the incident and reflected waves are collinear and normal to $\overrightarrow{q}$, are chosen. χ_0 and χ_n are the 0-th and n-th order Fourier components of the complex, lattice periodic susceptibility $\chi(\overrightarrow{r})$. The susceptibility related to the dielectric function $\varepsilon(\overrightarrow{r})$ (only in here, we use ε to present the dielectric function.) and a function of $\overrightarrow{r}$ in the crystal unit cell, can be described as,

$$\chi(\overrightarrow{r}) = \varepsilon(\overrightarrow{r}) - 1 \quad . \tag{3.41}$$

For a centrosymmetric crystal case, $\chi_{\overline{n}} = \chi_n^*$ and $(\chi_n\chi_{\overline{n}})^{1/2} = |\chi_n|$. The complex variable η is a function of the angle θ by,

$$\eta = \frac{(\theta_B - \theta)\sin 2\theta - \chi_0}{(\chi_n\chi_{\overline{n}})^{1/2}} \quad , \tag{3.42}$$

where θ is the reflection angle, and θ_B the Bragg angle defined by the kinematic theory, i.e. Eq. 3.4. The total wave field intensity is given by Eq. 3.38, where R is the reflectivity and the phase υ is now a function of angle within the range of Bragg reflection. Passing through the range of Bragg reflection by tuning the angle of θ or the x-ray energy, the phase υ changes by π. As a result, the XSW field moves to half of a diffraction plane spacing. The particular value of υ for a given angle depends on $[\chi_n/\chi_{\overline{n}}]^{1/2}$ in Eq. 3.40. Thus, υ is also dependent on the origin chosen for $\chi(\overrightarrow{r})$ or the structure factor. The locations of the nodal planes of the interference field for $\theta \ll \theta_B$, which corresponds to $\upsilon = \pi$, are commonly called diffraction planes and their position depends on structure factor or susceptibility [Zeg93]. An illustration is shown in Fig. 19 which presents the rocking of the reflectivity curve R around Bragg angle θ_B, the corresponding phase shift φ and the movement of the XSW field.

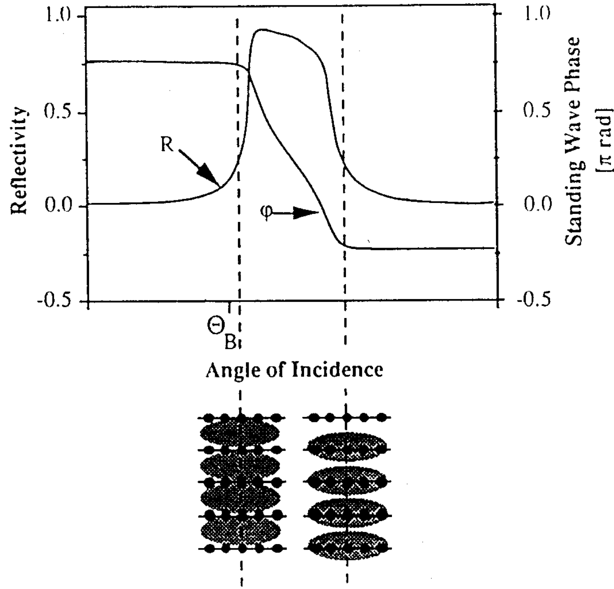

Fig. 19: Rocking the reflectivity curve R of a Bragg reflection from lower to higher angle θ around Bragg angle θ_B, the phase shift φ between incident and diffracted beam decreases by π radians. As a consequence the XSW field generated in the overlap region shifts by half a diffraction plane spacing into the crystal so that nodes are coincident with diffraction planes on the lower angle side of the reflection while on the higher angle side nodes are situated midway between these planes. θ_B is the Bragg angle.

For the XSW structural analysis, an important concept is that the detected scattering signal from an adsorbate atom directly reflects the corresponding wave field intensity I at this atomic position. The emission process of the adsorbate atom which is exclusively initiated by the photon interference field, i.e. a primary emission channel (PEC), is exactly proportional to the local wave field intensity. In this case, the normalized scattered yield Y_{sc} (fluorescence yield intensity) from an atom within the interference field characterized by $\overrightarrow{q}$ reflects the photoelectric absorption probability, and can be expressed as Eq. 3.38, where I is experimentally determined by Y_{sc}. From this formula we can determine the position of an adsorbate atom with $\overrightarrow{r} = \overrightarrow{r_A}$.

For a number N of adsorbate atoms, the XSW field is simply the sum of the scattered yields from the individual atoms at positions r_i. Moreover, consider that the thermal and/or static atomic displacements from their lattice sites, the conventionally used intensity expression of the XSW field is

$$Y_{sc}(\theta) = 1 + R(\theta) + 2f_c\sqrt{R(\theta)}\cos\left[\upsilon(\theta) - 2\pi\Phi_c\right] \quad , \tag{3.43}$$

where $R(\theta)$ is the reflectivity describing the shape of the Bragg peak and $\upsilon(\theta)$ denotes the phase of the XSW field changing from π to 0 when scanning through a Bragg reflection. $\Phi_c$and f_c are the coherent position and coherent fraction denoting the phase and amplitude

of the atomic distribution function in the crystal. A value of $f_c = 1$ indicates that all atoms occupy an identical lattice position, whereas $f_c = 0$ indicates a random order. The coherent position Φ_c gives the relative position of the adsorbate atoms with respect to the diffraction plane. Regarding to the occupancy of atoms at N different substrate lattice planes, the resulting f_c and Φ_c are related to the percentages f_{ci} of adatoms distributed on different positions Φ_{ci} by the following expressions, [Lag92]

$$\Phi_c = \frac{1}{2\pi} \arctan \left[\frac{\sum_{i=1}^{N} f_{ci} \sin(2\pi\Phi_{ci})}{\sum_{i=1}^{N} f_{ci} \cos(2\pi\Phi_{ci})} \right] \tag{3.44}$$

$$f_c = D_{DW}(1 - D_S)A_G$$

with

$$A_G = \left[\left[\sum_{i=1}^{N} f_{ci} \sin(2\pi\Phi_{ci}) \right]^2 + \left[\sum_{i=1}^{N} f_{ci} \cos(2\pi\Phi_{ci}) \right]^2 \right]^{1/2} \quad , \tag{3.45}$$

where A_G is the multiple position factor, D_{DW} is the Debye-Waller factor which represents the thermal vibrations, and D_s represents the random static disorder. By fitting the reflectivity intensity and the fluorescence yield, it is possible to evaluate f_c and Φ_c and hence to obtain information about the positions of the adsorbate atoms and the atomic disorder.

In order to understand the relation between $R(\theta)$, Y_{sc}, and Φ_c, we schematically illustrate them using an adsorbate atom in the crystal as Fig. 20. For the different atomic positions d within the lattice spacing d_n, i.e. different Φ, there are different shapes of fluorescence yield Y_{sc}, from which we can determine the atomic positions.

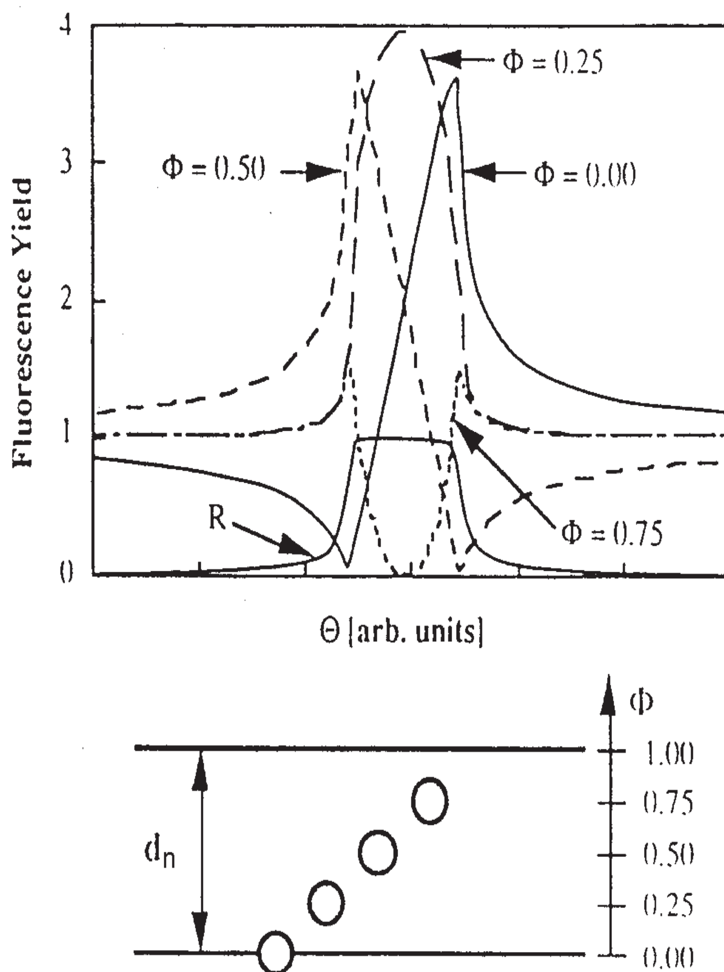

Fig. 20: Characteristic fluorescence yields as a function of angle in the vicinity of a Bragg reflection for atoms located at particular positions Φ within the diffraction plane spacing d_n. $\Phi = d/d_n$, where d is the distance of adsorbate atom with respect to the diffraction plane.

Chapter 4

Experimental Setup

4.1 In general

In this chapter we mainly introduce the experimental setup and procedures utilized for sample growth and structure investigation. It includes sample preparation of self-assembled InAs QDs, and x-ray diffraction experiments.

4.2 MBE growth procedure

In chapter 2, we have discussed the basic background of MBE growth. In this section we introduce the experimental performance of MBE grown self-assembled InAs QDs.

MBE growth experiments of self-assembled InAs QDs have performed in a Riber 32P MBE system with a ultra-high vacuum (UHV) of 1×10^{-11}mbar. The MBE growth chamber was equipped with a 12 kV RHEED system, in combination with a CCD camera, frame grabber, and a personal computer for image processing. A special developed software allows either to follow selected spots in a tracking mode or to measure the intensity of the most intensive spot within a selected frame. RHEED oscillations were recorded using the first mode. The second mode was used for the *in situ* measurements of the InAs QD formation. The substrate used in the present work is epi-ready (001) GaAs wafer. The GaAs wafers have been processed in a etching chamber, where the thermal oxide desorption of the wafers were done. Subsequently, the wafers were transferred into the MBE growth chamber. Prior to InAs growth, a 200 nm-thick GaAs buffer layer was

grown at 600^0C substrate temperature so that a smooth substrate surface is achieved. This growth is monitored by RHEED pattern. For the self-assembled InAs QDs growth, the growth parameters such as the substrate temperature, InAs growth speed, deposited coverage thickness, and As-flux are essential to the InAs QD quality. In our case, the conventional temperature range for InAs growth was chosen between 450^0C and 500^0C. The InAs growth speed is about 0.1 ML/s. The As-flux was adjusted corresponding to a flux gauge reading between 1×10^{-5} mbar and 4×10^{-6} mbar. By changing the above growth parameters, we expect to get different InAs QD structures. The actual growth conditions for different aspects of structural characterizations will be discussed in each of the latter chapters.

The InAs growth speed was determined by performing RHEED intensity oscillations for GaAs growth at 600^0C and $In_{0.1}Ga_{0.9}As$ growth at 500^0C, respectively. Since the RHEED oscillation frequency approximately reflects the growth speed, the InAs growth speed was obtained from the difference between the measured $In_{0.1}Ga_{0.9}As$ and GaAs growth speeds. The respective growth temperatures were chosen in such a way that on one hand a large number of oscillation periods was found and on the other hand the sticking coefficients of both species are nearly unity [Hey00].

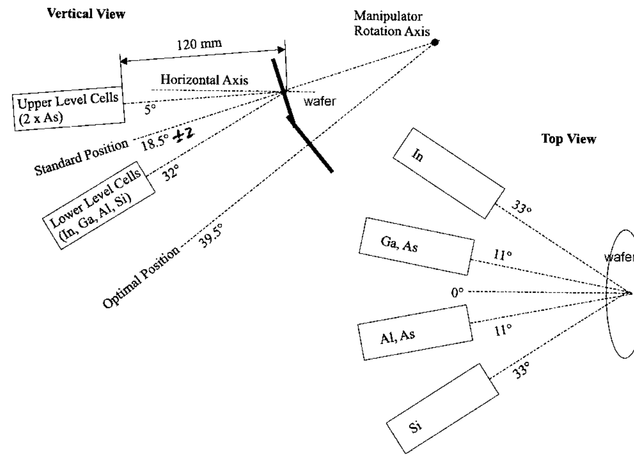

Fig. 21: Schematic illustration of the cell positions in the Riber-32P MBE system. The relative positions of effusion cells of growth materials and the wafer position are shown in vertical and top views.

In the Riber 32P-MBE system employed in the present measurements, the relative location of effusion cells of deposited materials are sketched in Fig. 21. In vertical view, the In cell is located with an angular divergence relative to wafer surface normal, i.e. the dashed line marked with standard position. The standard position is the actual wafer position for MBE growth, whereas the optimal position marked in the figure is the best geometry for InAs growth. In top view, the angular divergence of the In cell with respect to the wafer is illustrated. From the In cell location, we calculate the actual direction for In flux projection on the wafer being of about 23^0 with respect to the $[1\,\bar{1}0]$ direction of the wafer as shown in Fig. 22. Moreover, from the divergence of the spatial azimuth of In cell with respect to the wafer surface normal as shown in Fin. 21, we predict that the deposited InAs coverage thickness on the wafer should be inhomogeneous. This inhomogeneous distribution leads to the higher InAs coverage thickness existing at the regime of the wafer close to In cell, whereas the lower coverage is expected at the regime far from the In cell.

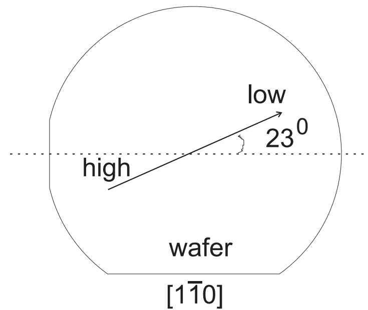

Fig. 22: Schematic illustration of the direction for In flux projection on the wafer. In inhomogeneously distributed along this direction. high $\longrightarrow$ higher InAs coverage thickness, and low $\longrightarrow$ lower coverage.

In order to experimentally characterize this inhomogenety of InAs coverage on the wafer, we performed In fluorescence measurements on MBE grown samples. The nominal InAs deposition determined by RHEED is 2 ML. By normalizing the intergrated In fluorescence intensities to that determined from a reference sample inside which the amount of In equal to 2 ML is inserted by using ioni-insertion technique, we get the distribution of the InAs coverage thickness on the wafer. As to the detailed description concerning the measurements, please refer Ref. [Foe99]. We show the distribution of InAs coverage thickness in Fig. 23. The InAs coverage thickness is inhomogeneously distributed in both $[1\bar{1}0]$ and [110] directions. This result is mainly due to the In cell location geometry as shown in the Fig. 22. Furthermore, from AFM image analysis of samples grown with 1.86 ML InAs coverage at 450^0C, we get the QD number densities at different regions of

the sample, as shown in Fig. 24. This experimentally reflects that InAs distribution is inhomogeneous. In order to avoid such effect, we adopted to rotate wafer during InAs deposition to form QDs. This technical processing was utilized for all samples studied in the later chapter, except for samples used for RHEED oscillation studies.

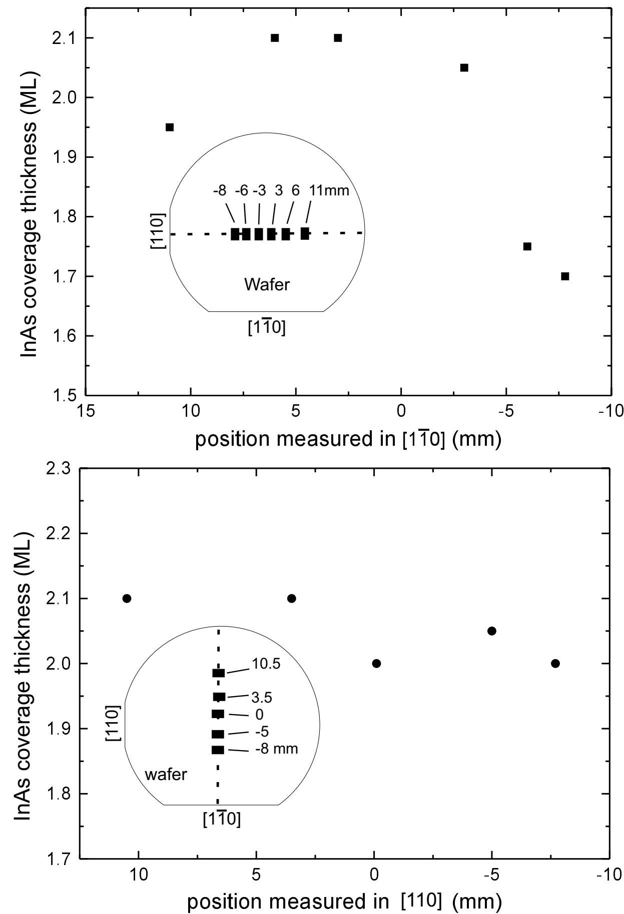

Fig. 23: The actual In coverage in different sample positions. The sample used here is InAs QDs grown at 500^0C with nominal InAs coverage of 2ML determined by RHEED. Data in upper figure were collected along [110] direction, and in lower figure along [1$\bar{1}$0] direction. The inset in both figures are the schematically shown positions.

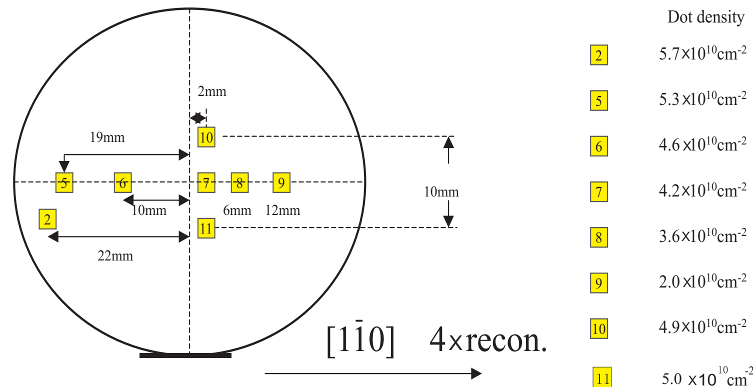

Fig. 24: Dot number density distribution determined from AFM measurements on InAs QD 2-inch-wafer sample grown at 450^0C with InAs coverage of 1.86 ML. The small square areas are the positions for AFM measurements.The central of the wafer is defined as 0 mm.

4.3 X-ray experiments

In general, we have performed x-ray experiments at different beamline stations of the Hamburger synchrotron radiation laboratory (DESY HASYLAB). In the present work, we employed GISAXS, GIXRD, CTR and XSW techniques at undulator Beamline BW1, where high x-ray flux is available. This enables us to study the crystal structure and atomic location in ultra-thin films and QDs system grown by MBE. Moreover, we also performed GIXR, x-ray topography and other test experiments at ROEMO I beamline with double monochramator and CEMO beamline with reflected mirrors. The main difference among these beamlines is the different intensity fluxes generated by synchrotron radiation. Therefore, the experimental setups mounted are different for different experimental purposes. In the following we show a schematic illustration of the diffraction geometry [Loh93] in Fig. 25 which presents the geometry with six-circle movements.

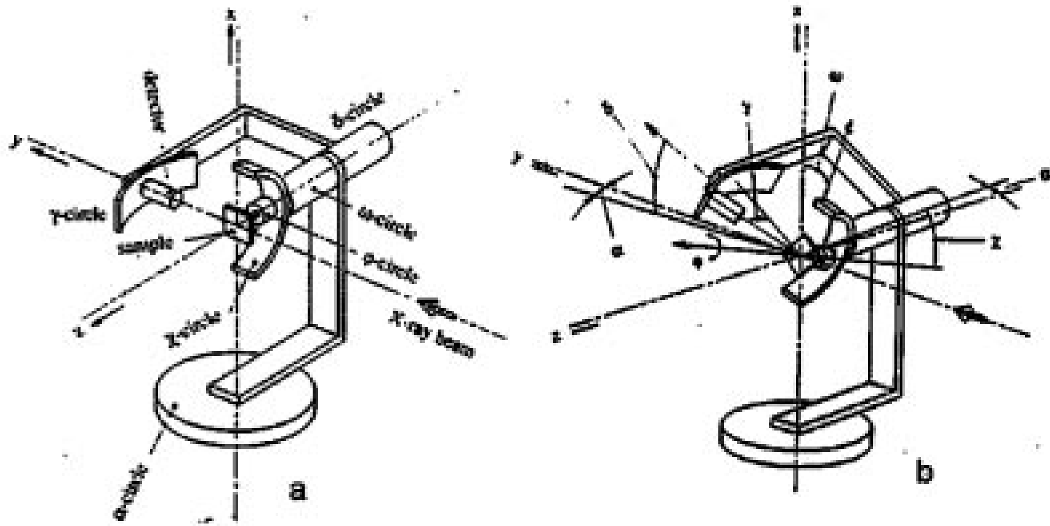

Fig. 25: (a) A schematic drawing of the six-circle diffractometer with all circles set to the zero position. (b) The diffractometer with all circles having a setting in the first quadrant [Loh93].

In the figure, there are totally six degrees of freedom, that can be separated into one for shared α circle, two for detector of δ and γ circles, and three for sample of ω, φ, and χ circles of freedom. Fig. 25(a) shows the diffractometer with all angles set to zero, and Fig. 25(b) shows that with all angles having values in the first quadrant. In the case of all angles set to zero, the laboratory frame coordinates $x,\ y,\ z$ are chosen such that the horizontal plane of diffractometer lies in the yz plane, the incoming x-ray beam impinges on the sample along the positive y direction, and the φ axis points to the positive z direction. The sample was mounted on the φ axis, and can be adjusted by rotating both φ and χ axis. Both the φ and χ circles are supported by the ω circle, which connects to the main diffractometer mount. The detector was mounted on the γ axis, which is fixed to the detector arm. The detector arm can rotate around the δ axis. The whole axises are mounted on top of a rotary table which can be rotated as α circle. With these six circles

of freedom, the diffractometer can be operated in the different geometries leading to the different kinds of diffraction experiments being possible. In each diffraction experiment, one has to fulfill the general diffraction condition by moving different axises so that the scattering vector q must be matched to a reciprocal lattice site (HKL), i.e. the Bragg diffraction condition.

4.3.1 X-ray Topography

By means of x-ray diffraction, it is possible to gain detailed information about the structure of the crystalline lattice integrated over the whole illuminated region of the sample. If information about the spatial distribution of sample properties is needed, x-ray topography is a very powerful method to meet these requirements, because it provides a two-dimensional image of the measured crystal. For further information, please refer, e.g. Ref. [Tan76]. Regarding to our InAs QD samples, x-ray diffraction experiments require measured samples with an almost perfect substrate crystal structure so that the structural characteristics inside dots can be quantitatively resolved with high accuracy. Therefore, the best crystal quality of the GaAs wafers used for MBE growth are highly desired. In this case, we performed x-ray topography experiments on GaAs wafers in order to detect the crystal structure of GaAs wafers.

Fig. 26 shows the setup of x-ray topography experiments. After being reflected from a perfect monochromator crystal, the x-ray beam strikes the second asymmetric monochromator from which the beam size can be increased. The reflected beam illuminates the sample at the Bragg angular condition and finally reflected on an x-ray sensitive film. In the setup sketched here the nondispersive position for the two monochromators is chosen, i.e. theoretically the complete energy spectrum of the x-ray source can be used for topography. The usable wavelength range in reality is restricted by the distances between source and monochromator and between monochromator and sample as well as by slits in the beam path. This limitation in wavelength is of crucial importance since the direction of the intensity reflected by misoriented regions of the sample depends on the wavelength of the incoming beam. The energy of x-ray is selected to be 15 keV in the present experiments which were performed at ROEMO I beam station in DESY HASYLAB.

To gain information not only about the small sample region being illuminated by the x-ray beam which is reflected from the monochromator, but also about the complete sample area, we perform a translation of the sample and film relative to the beam. This is marked

in Fig. 26. The detector is used for the adjustment of the sample to the Bragg reflection for the topographic image.

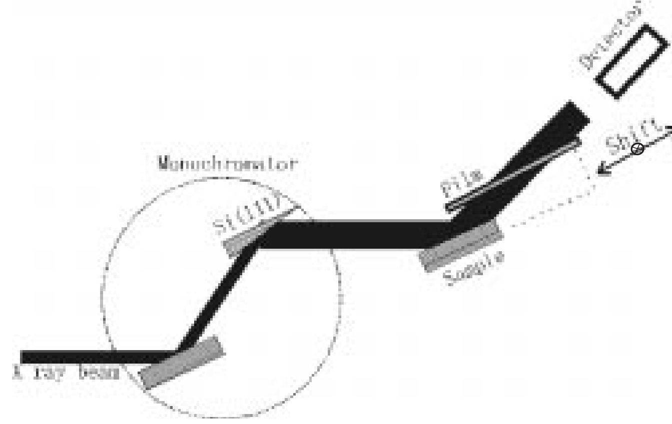

Fig. 26: Setup for x-ray topography with double monochromators. Arrows and ⊗ sign represent the shift directions of the sample and film.

We show measured topographic images in Fig. 27, in which case (a) was directly taken from incoming x-ray beam. From the illuminated area in the image we see there is a very homogeneous image contrast, which represents our incoming x-ray beam flux is homogeneous, whereas in Fig. 27(b) we observed different contrasts. Bright contrasts indicate lattice planes contributing to x-ray Bragg diffraction. Dark contrasts represent lattice planes that are off Bragg condition. However, the crystal defect is not very serious in the wafer, since we only observed one small region with high contrast. This defect may result from the crystal dislocations inside. Other contrasts shown are due to the different bending range of the crystal planes leading to a gradual deep image contrasts. By rocking sample around the Bragg diffraction condition, we determine that in our wafer, the angular difference of the planes with off-Bragg condition is within 0.01^0 in comparison to those in Bragg condition. This reflects that the quality of our GaAs wafers is good for MBE growth and expected to not give rise to additional influence on further structural investigations.

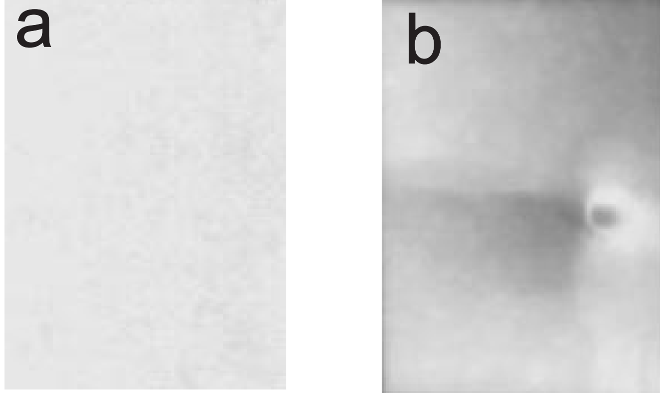

Fig. 27: Topographic images of x-ray beam (a) and GaAs wafer (b) with size of about 15 × 20 mm^2. Bright contrasts indicate their corresponding lattice planes contributing to x-ray Bragg diffraction. Dark contrasts represent their lattice planes are off Bragg condition with different ranges.

4.3.2 Grazing incidence x-ray experiments

The grazing incidence x-ray experiments include GISAXS, GIXRD, and GIXR. We employed these techniques to characterize the QD lateral distribution, QD shape, QD strain status, and the surface and interface structures of InAs samples. The principle of these techniques has been interpreted in Chap. 3, Sec. 3.3, 3.4, and 3.5. Here we note how to move angles of diffractometor in order to get different kinds of experimental conditions.

Prior to the experiments, one should adjust the zero position of the whole diffraction geometry with respect to the incoming x-ray beam. For GIXRD and GISAXS experiments, the incident angle α_i of the incoming x-ray beam to the sample surface was set to be smaller than the total external reflection angle of GaAs. This can be achieved by moving the α axis. In case of GISAXS and out-of-plane GIXRD experiments, the detector is a PSD mounted parallel to the sample surface so as to resolve the large lateral scattering vector in reciprocal space. In the following we describe the adjustments of the setup to achieve different grazing incident x-ray experiments.
i) As to GISAXS, we only need to perform γ and ω axicial movements, since the diffusing signal caused by InAs QD distribution is located at both sides of the specular beam reflected by the sample surface which is near to the origin of the reciprocal space. By moving γ, the PSD goes off the xy plane (refer Fig. 25), i.e. $q_x - q_y$ plane in reciprocal space, towards to positive z axis, i.e. along q_z in reciprocal space. The movement of ω enables us to set the sample in different sample azimuthal orientations, at which PSD

can collect the diffusing scattering signals. In this way, we are able to characterize the azimuthal dependent QD lateral distribution.
ii) As to out-of-plane GIXRD, in order to get structural information of the inclined lattice planes (refer Fig. 13(b)), we need to move ω, γ and δ axises to the (HKL) Bragg diffraction condition.
iii) As to GIXR, we need to perform radial scan at grazing incident case, i.e. $\gamma = \alpha$ indicated in Fig. 25, with α being of $0^0 - \sim 5^0$ range.

4.3.3 Crystal Truncation Rod Technique

CTR experiments on (HKL) Bragg diffraction rods are achieved by performing high resolution x-ray diffraction scans along L rods i.e. the q_z direction in the reciprocal space. In this case, the experimental setup shown in Fig. 25 was slightly altered. The sample was mounted with its surface normal parallel to x axis in Fig. 25. By rotating ω, δ, γ axises, one can approach CTR diffraction condition.

4.3.4 X-ray Standing Wave Technique

The actual performance of XSW is similar to CTR, but an ionization chamber instead of a PSD was used to record the reflectivity curve of the measured Bragg diffraction. Moreover, we need to mount an additional Si(Li) detector for In fluorescence signal collection. The principle of XSW has been interpreted in Chap. 3, Sec. 3.7. Here we introduce the setup of this experiment as shown in Fig. 28. A combination of a symmetric 1st and asymmetric 2nd monochrometer crystals was used to get a x-ray beam of small divergence and free of higher harmonics. The beam is stabilized by an intensity stabilization system which was set up in front of the slit. The incoming x-ray beam size is controlled by the slit and the intensity signal I_{in} is recorded by an ionization chamber. The sample was rocked around ω axis at the (004) Bragg reflection (ω axis here is the same as the case in CTR setup). The corresponding diffraction intensity I_{out} is measured separately by ionization chamber mounted at detector arm. The sample rocking is performed with an angular step of $\Delta\theta_0$. $\Delta\theta = 0$ corresponds to the exact Bragg diffraction position. For each step, the ratio of $R = I_{out}/I_{in}$ is counted. Simultaneously, the In fluorescence intensity spectrum generated by the standing wave field is recorded by a multiple channel analyzer (MCA). This procedure is completed after we get the whole reflectivity curve around the Bragg reflection. In this way, a series of In fluorescence spectra have been

obtained. By determining the intensity maxima I_{Fl} of In fluorescence curve at energy of E_{Fl} (in the fluorescence spectrum, the dashed lines represent the energy range of In fluorescence intensity curve), we plotted the integral intensity against $\Delta\theta$. So far, we get two experimental intensity curves, i.e. $R = f(\Delta\theta)$ and $I_{Fl} = f(\Delta\theta)$ (here I_{Fl} is the same as Y_{sc} in Eq. 3.43), from which we can determine the coherent position and coherent fraction of In atoms located in the δ layer system or inside InAs QDs.

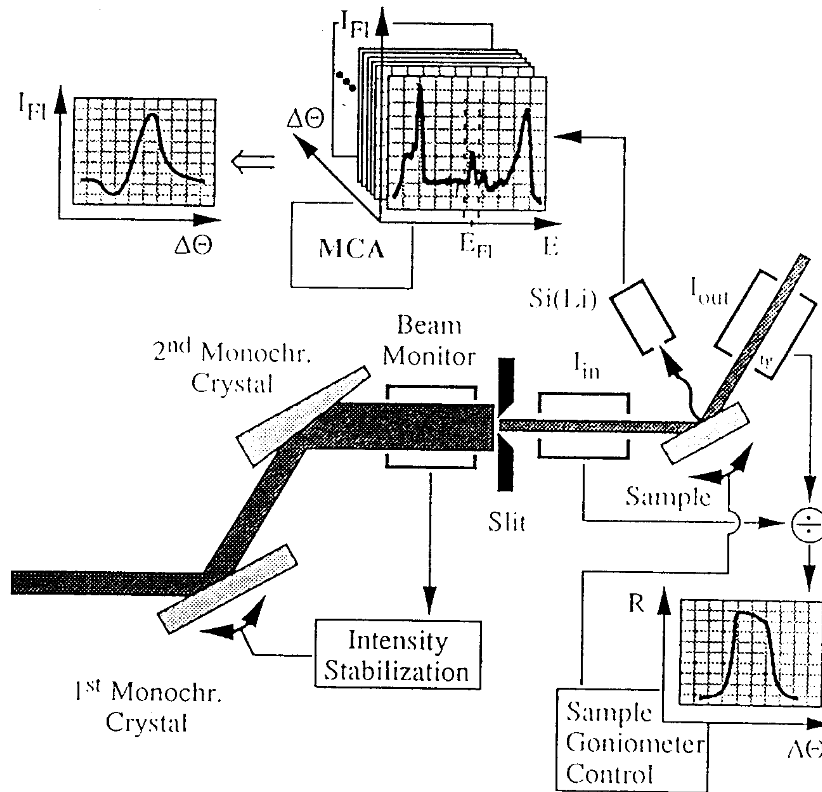

Fig. 28: Schematic illustration of the XSW experiment setup and data acquisition.

4.4 Summary

The above shown x-ray experimental setups enable us to collect structural information of MBE grown InAs on GaAs substrate. The samples grown include uncapped and capped samples. X-ray technique turns out to be very powerful to investigate the buried InAs layer. In Fig. 29, we schematically specify these different x-ray experiments in the reciprocal space. The Bragg diffraction spots illustrated in the figure are chosen to study different structural information on our InAs samples. We note that the actual reciprocal space is more complicate than the present illustration, which reflects the complicity of sample structures.

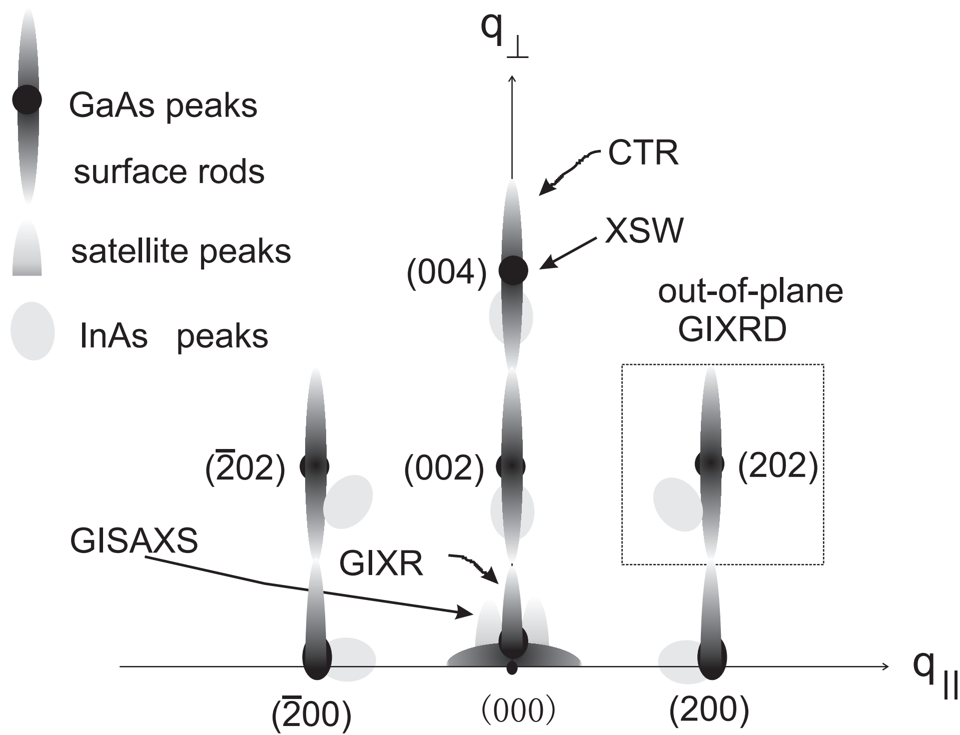

Fig. 29: Schematic illustration of different x-ray experiments, i.e. GISAXS, out-of-plane GIXRD, GIXR, CTR and XSW, in the reciprocal space.

Chapter 5

Growth Investigation by RHEED

5.1 In general

InAs QDs are grown with MBE monitored by RHEED oscillations and patterns. By utilizing different growth parameters, such as the substrate temperature, As-flux, In-flux rate and number of As-flux cells, the structure of QDs is expected to be changed. Moreover, growth with different types of misorientation and/or patterning substrates, structure features of QDs are different. These findings were studied intensively in recent years [Mas93, Toy93, BH94, Xie94, Mad94, Kob96, Ber97, Ram97b, Ram97a, Nak98, Mur99, Ish00]. In addition, in order to fabricate opto-electronic device by using InAs QDs, GaAs cap layers have to be deposited on top of the QDs, which were reported to play an important role for QD quality. Different kinds of growth conditions were used to improve the GaAs capping structure so that one can achieve desired opto-electronic properties of InAs QDs [Sch97, Hei98, Che94, Ish99, Max99]. For above cases, *in situ* RHEED technique is a conventional tool to control the MBE growth conditions of QDs and cap layers. In this chapter, we discuss *in situ* RHEED observation of self-assembled InAs QD formation.

5.2 *In situ* RHEED pattern

For RHEED study, GaAs wafers were adjusted with the $[1\bar{1}0]$ direction parallel to the electron beam. During growth, the wafer is not rotated so that the RHEED oscillation

and image could be recorded. The InAs growth speed was about 0.07 ML/s and the arsenic flux was 5×10^{-6} mbar. The RHEED pattern presents a 2×4 reconstruction with sharp spots and surface diffraction streaks as shown in Fig. 30a for buffer layer growth at 600^0C, which indicates diffraction from a smooth and facet-free surface. Due to the grazing incidence of the incoming electron beam with final mean free path of the electrons, the beam impinges only the uppermost few monolayers of the GaAs substrate surface. Therefore, in reciprocal space these thin monolayers contribute to surface truncation rods which are perpendicular to the crystal surface. The intersection between the Ewald sphere and these rods yields diffraction spots which are located on a Laue-circle. In the case of a very smooth surface, the lateral size of the rods is so narrow that the intersection shows very sharp diffraction spots. If there exist surface steps, the lateral size of the rods is broadened due to the finite size effects of the steps leading to the intersection presenting elongated RHEED patterns towards to the surface normal, which are denoted as surface streaks. Typical 2×4 reconstructed (001) GaAs surface shows a Laue-circle in $[1\bar{1}0]$ azimuth and streaks in [110] azimuth [Hey00]. This reflects the anisotropy of the two-dimensional growth islands, that have a shorter length and thus higher density of surface steps in [110] as compared to $[1\bar{1}0]$ direction [Sud92]. Prior to InAs deposition, the substrate temperature was decreased down to 500^0 C resulting in a change of the GaAs surface reconstruction to $c(4 \times 4)$ with surface diffraction streaks (Fig. 30b). Again, the RHEED spots are arranged on the Laue-circle. After the Indium shutter was opened, the reconstruction spots instantaneously disappear, but still the RHEED patterns show a two-dimensional surface morphology (Fig. 30c). The transition from 2D to 3D InAs growth was found to be at 1.7 ML InAs deposited. At this point, the 2D diffraction spots disappear (Fig. 30d) before new 3D type diffraction spots emerge. In Fig. 30e the diffraction pattern observed at 2.1 ML InAs coverage is displayed. In contrast to the above cases, the RHEED diffraction spots are not located on the Laue-circle characterizing the surface diffraction cases. Instead, they show the bcc reciprocal crystal lattice of the InAs bulk crystal. This reflects that the change from 2D surface related features to 3D bulk diffraction spots took place due to the transition of the growth mode from layer to island growth. Moreover, it can be clearly seen that the 3D diffraction spots are decorated with additional weak intensity tails, so-called chevrons [Lee98]. The origin of the chevrons is still not clear so far. One possible interpretation is that they might be attributed to the reciprocal lattice rods which are oriented perpendicular to the side facets of pyramid-like InAs QDs [Nab94, Lee98]. Moreover, we did not observed any chevrons in our RHEED pattern along [110] azimuth. We note that besides the 3D diffraction spots there still exists

a surface specular beam spot at which no chevron is attached. We terminated the InAs growth after 2.1 ML deposition. After 30 seconds delay time, a 5-10 nm thick GaAs cap was grown at the same substrate temperature as the InAs growth. The corresponding RHEED pattern is presented in Fig. 30f showing a surface specular beam spot only. From this we infer that the GaAs cap layer has considerable roughness [Zha99]. Samples used for structural investigation were grown by the same procedure as above, except that the sample was rotated during InAs and GaAs cap layer growth. While sample rotation prevents us from monitoring the InAs growth with RHEED it will improve the homogeneity of the QD size and distribution on the wafer. We note that the RHEED pattern before and after deposition of the InAs layer does not differ from the above case. As soon as the growth was finished, the sample was quenched by stopping the substrate heater.

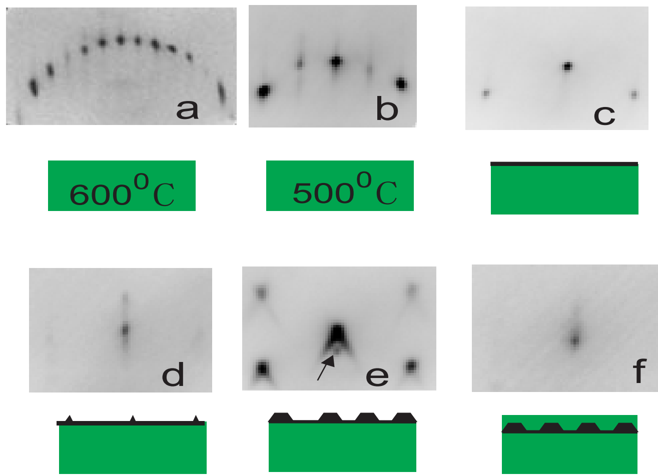

Fig. 30: *In situ* RHEED patterns observed during MBE growth of InAs on GaAs (001). (a) flat GaAs substrate surface at 600^0 C in $[1\bar{1}0]$ azimuth, (b) flat GaAs substrate surface at 500^0 C in $[1\bar{1}0]$ azimuth, (c) 1 ML InAs deposition, (d) transition from 2D to 3D takes place at InAs deposit thickness of 1.7 ML, (e) 3D InAs QDs growth at 2.1 ML InAs coverage, (f) after GaAs cap layer deposition. An arrow in (e) case indicates the specular beam spot.

5.3 RHEED intensity observation

Fig. 31 [Hey00] shows an example of the RHEED intensity evolution during InAs deposition. We recorded the reflection intensity from the specular beam spot during InAs deposition. We observe a slight intensity oscillation of the 2D growth related RHEED reflection, reflecting the behavior of the highly strained 2D surface structure. The 3D type

reflection which occurs due to the transition into the Stranski-Krastanov growth mode, gives rise to a rapid increase in intensity as recorded from a 3D Bragg spot. The time t_c between the beginning of InAs deposition and the first appearance of InAs QDs related RHEED patterns can be determined very accurately. Assuming that the flux is constant and all impinging In atoms stick on the surface, the deposited InAs coverage thickness can be calculated proportional to the deposited time. We thus obtain the critical deposited thickness for the onset of dot formation. The intensity of the 3D growth related reflection is saturated at about 2.0-2.3 ML (taking different growth parameters utilized in the actual experiments into account), which is associated to that reported in literature [Moi94, Ram97a, Joy97], from which the density of 3D InAs islands on the surface is saturated at approximately 2.0 ML. In the saturation regime the InAs QDs grow only in size while the number density of QDs keeps constant [Moi94, Ram97a, Joy97]. The above similarity reflects that in the saturation regime the intensity of RHEED reflection is primarily controlled by the QD density not by the QD size [Hey00]. In this way, the time t_f as indicated in the figure, between the onset of QD formation and the saturation of RHEED intensity corresponds to the time for a complete 2D to 3D transition.

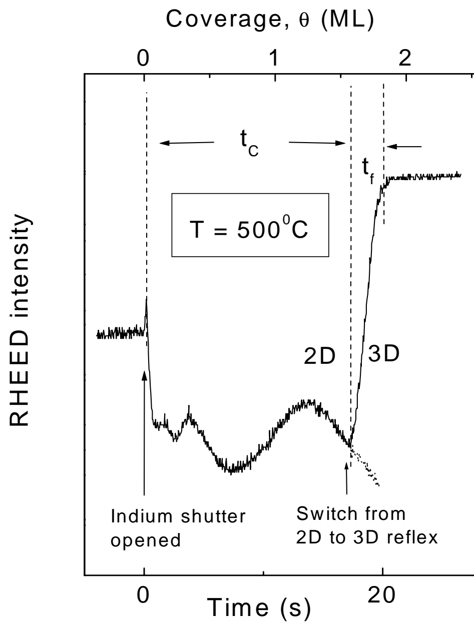

Fig. 31: Time evolution of the intensity of 2D and 3D growth related reflection. When the intensity of 3D reflection exceeds that of the 2D reflection, the data acquisition software switches to record this reflection. This arrangement is applied since both reflections may be found at different positions depending on the respective diffraction conditions. The dotted intensity data represents a second measurement of the 2D reflection under identical conditions but without switch. [Hey00].

Chapter 6

AFM Investigations on Self-assembled InAs QDs

6.1 In general

The AFM technique is an easy tool utilized to investigate surface morphology of crystals. In the present work, direct pictures of self-assembled InAs QDs were obtained by AFM in contact mode. The AFM machine is TopoMetrix Explorer. The cantilever tip (Si) used here has a nominal diameter of about 10 nm, which is of the same order of magnitude as the size of InAs QDs. By AFM scanning, we can get direct information on the lateral distribution of dots.

6.2 AFM image

A series of samples with InAs coverage from 1.8 to 4.0 ML were grown at substrate temperature of 500^0C for AFM observation. The In deposition rate was about 0.1ML/s and the As-flux was $4-6\times10^{-6}$ mbar. Fig. 32 shows AFM images of self-assembled InAs QDs. The AFM scanning direction is along $[1\bar{1}0]$. The InAs coverage is labeled in each picture. For all pictures, the image size is 500×500 nm^2. From AFM images, we observe that 2.3 ML InAs coverage is a limit value, below which the InAs QD size is homogeneous with a relatively low QD density. At 2.3 ML, the InAs QDs are still homogeneous, but the dot density becomes saturated. Along with an increasing InAs deposit, the dot density

keeps constant, but the dot size increases. In particular, at 2.8 ML InAs deposit, we find there are a few big dots appearing in the image, which means the existence of coalescence in this case leading to dislocation inside such coalescence dots. This effect is even more pronounced in the case of a 4.0 ML InAs deposit.

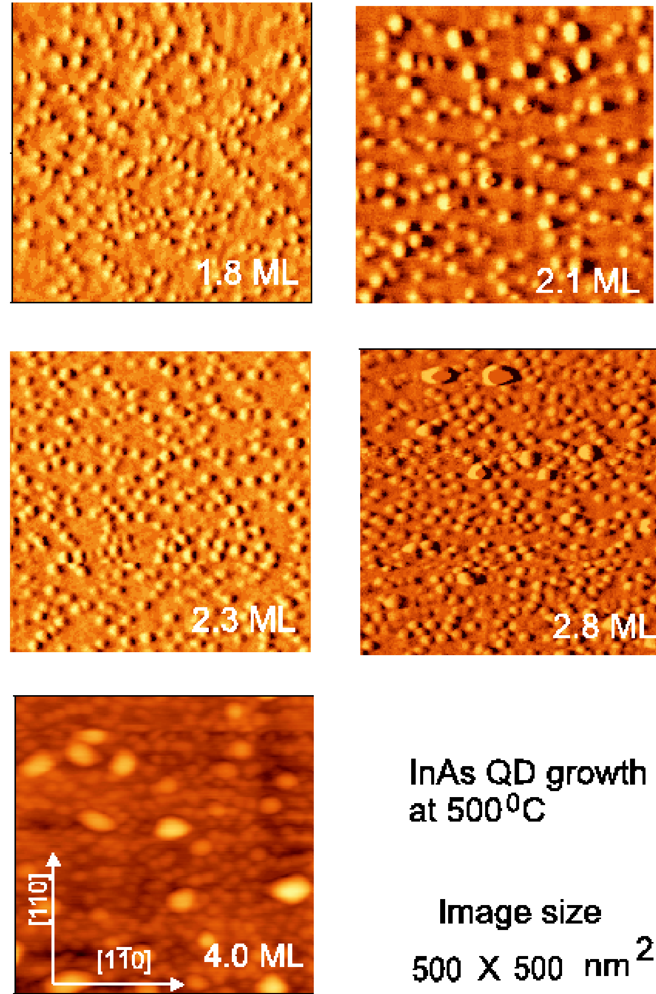

Fig. 32: AFM images for samples with different InAs deposits ranging from 1.8 ML to 4.0 ML. The AFM image size is 500×500 nm^2. The AFM scanning direction in along [1$\bar{1}$0].

By analyzing AFM images, we thus get the height distribution and the number density of the dots as shown in Fig. 33. We find the most homogeneous dot height distribution

below 2.3 ML InAs deposit.

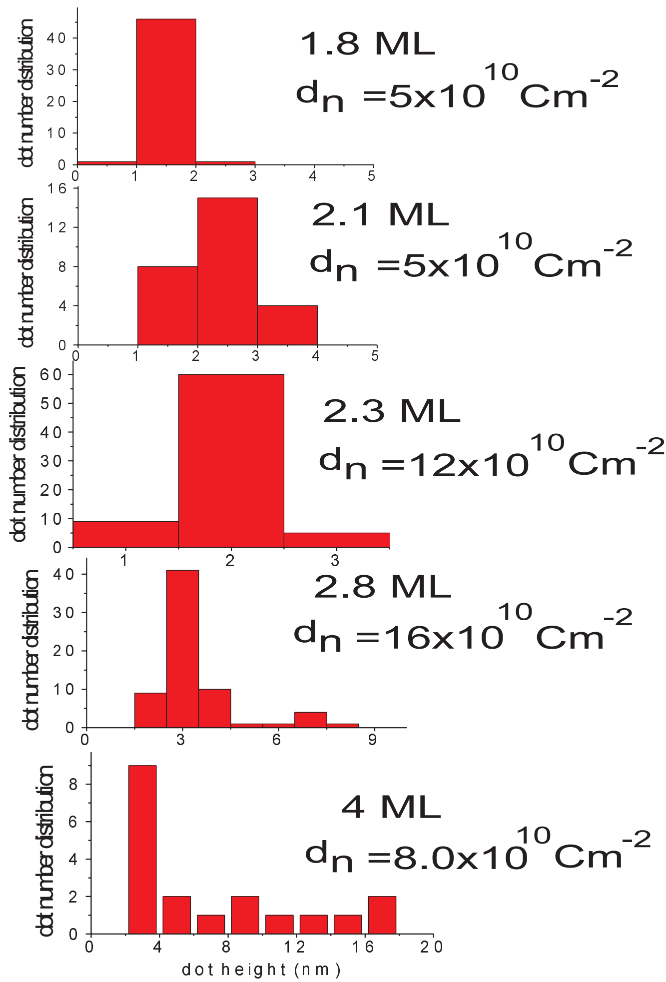

Fig. 33: InAs QD height distribution analyzed from Fig. 32 for samples with InAs deposits of 1.8 ML-4.0 ML, respectively. In each case, the dot density is also presented.

From the analysis of above AFM images, we conclude that there is a limit value for InAs deposition, below which the dot size is homogeneous with a narrow size distribution.

In addition, InAs QD growth on a stepped crystal surface was also performed. The stepped GaAs wafer is labeled with orientation as $(100)2^0 \rightarrow (1\bar{1}0)$ $(\alpha = 45^0)$, which indicates the surface normal [001] misoriented with 2^0 towards to [100] crystal direction. The InAs deposit was 2.3 ML coverage with an In flux rate of 0.1 ML/s. The As-flux was controlled to 4.2×10^{-6} mbar. These are the same growth conditions as we used to grow InAs QDs on a well-oriented [001] GaAs wafers. Comparative AFM images for both types of samples are shown in Fig. 34. From the images, it is easy to distinct the

quality of the QD distribution. The QD height distribution on the stepped wafer (b) is more homogeneous than that in normal wafer (a). Moreover, the average dot height on the stepped wafer is slightly larger than that in case (a), while the dot number density is smaller than that in (a). Especially, we note that the InAs QD lateral distribution on the stepped wafer is more ordered in comparison to the case (a). The white arrow in (b) indicates the misorientation direction of the surface with a step width of approximate 10 nm. In the perpendicular direction i. e. [010] there is no such limit. Instead of the isotropic QD lateral distribution, we observe an ordering trend as indicated by a white line, i. e. the dots line up along the step direction. Moreover, QD lateral arrangement tends to a square-like lattice type. Therefore, we suggest that the stepped GaAs surface may improve the InAs QD lateral distribution.

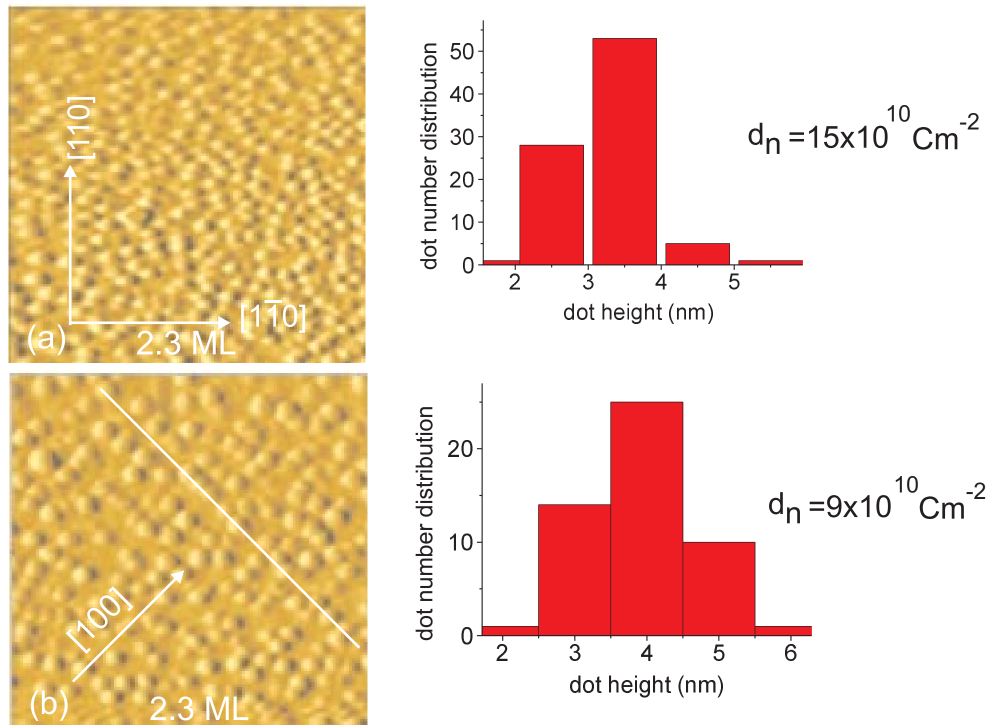

Fig. 34: AFM images of InAs QDs on (a) a well-oriented wafer with surface perpendicular to [001], (b) a stepped wafer with surface oriented 2^0 towards to [100] direction. For each case, the dot height distribution and dot number density are also shown. The AFM image is $500 \times 500 nm^2$.

Chapter 7

Ordering and Shape of Self-assembled Uncapped InAs QDs

Quantitative GISAXS and AFM experiments have been performed on self-assembled InAs QDs grown by MBE. We find pronounced nonspecular diffuse scattering satellite peaks with high diffraction orders, indicating a lateral ordering in the spatial positions of the InAs QDs. The mean dot-dot distance and correlation lengths of the dot lateral distribution are found to be anisotropic. We observe the sharpest dot distribution in [110] direction. Additional broad diffraction peaks are observed and associated to dot facet crystal truncation rods (CTR) of the {111} and {101} facet families. This suggests an octagonal-based dot shape truncated by (001) plane.

7.1 Research focus

The smallest and strongest confinement in three dimensions, e.g. InAs QDs on GaAs substrate is achieved in so-called self-assembled systems with the Stranski-Krastanov growth mode [Str39]. Studies with AFM and transmission electron microscopy (TEM) reveal that at low InAs coverage the QDs are coherently strained, dislocation-free and have diameters of a few 10 nm with a surprisingly narrow size distribution [Leo93]. Furthermore, there is a great effort to characterize, understand and improve the structural properties of such QD nanostructures, as reported recently [Dar97, Xie95, Spe97, BH95, Ter96]. In models for strain-induced self-assembling and ordering it is pointed out that vertical stacking of many layers of QDs, separated by thin spacer layers, may enhance the lateral and vertical

ordering as well as the size homogeneity [Ter96]. Experimental studies qualitatively verify the theoretical predictions [Xie95]. It has been shown experimentally that the strain field of a QD extends far into the underlying wetting layer and substrate [Chr94, Str98]. This strain field surrounding each QD may induce dot-dot interaction, that strongly influences the growth of neighboring dots and thus causes short range ordering of neighboring dots. This scheme has been applied to interpret the vertical ordering in a multilayer of InAs/GaAs QDs [Gru95a, Bim95]. Experimentally, high resolution X-ray diffraction plays an important role in the study of the structure in the vertical stacking InAs QD samples [Dar97]. However, as to a single dot layer structure, there is little experimental knowledge about the lateral ordering character of QDs, and x-ray diffraction measurements are difficult to resolve directly the structure information concerning of QDs, since the total amount of volume fraction of InAs dots is so small that generally, the scattering intensity from InAs QDs is very weak.

Also the shape of InAs QD is debated intensely, since an accurate calculation of the electronic structure depends critically on the exact QD shape [Sti99]. Square-based pyramid lens shapes [Gru95b, Sai98] and conical dot shapes [Mar94] have been proposed and complex numerical models have been developed to predict the dot shape, e. g. an octagonal-based shape predicted by finite element calculation [Mol98]. Various experimental techniques like AFM [Leo94, Moi94], RHEED [Nab94, Lee98], scanning tunneling microscopy (STM) [Joy98, kX99], and transmission electron microscopy (TEM) [Leo93, Xie95, Gru95a, Chu99] have been employed in order to determine the shape of the dots. However, these investigations so far did not provide a definite picture of the QD shape.

In order to measure the ordering and shape of an uncapped InAs QD single layer, we have performed novel high resolution GISAXS experiments [Sch98] with high flux synchrotron radiation. The grazing incidence technique probes the crystal surface up to depths of only a few nanometers so that the volume fraction of InAs probed is much larger in comparison to conventional x-ray techniques. Furthermore, as compared to AFM measurements, a relatively large area contributes to coherent scattering so that the distribution can be determined with improved statistics. In addition, the GISAXS technique allows the determination of the facet families and the average facet sizes of the InAs QDs. Most importantly, it provides us an opportunity to investigate InAs QD layers buried beneath a GaAs cap layer which would obstruct AFM studies. This will be discussed in Chap. 8.

7.2 Sample preparation

For the detailed sample growth procedure, please refer Chap. 5. The specific of growth is that the substrate temperature was set to 500^0 C for InAs growth. The As-flux was controlled to be about 6×10^{-6} mbar. The amount of InAs deposited corresponds to a coverage of 2.1 ML. The In flux was calibrated to be 0.1 ML/s with RHEED oscillations. The misorientation of the wafer surface with respect to the (001) crystal plane is determined to be about 0.01^0 by x-ray topographic technique.

7.3 Experimental

GISAXS measurements were performed at beamline BW1 at a wavelength of 1.17 Å. For the experimental setup and principle, refer Fig. 14 and Chap. 4, Sec. 4.3. The incidence angle to the sample surface was chosen to 0.18°, which is just below the total external reflection angle of 0.23°. Intensity profiles i. e. the specularly reflected beam (reflected by the sample surface) and the scattered intensity distribution from InAs QDs were collected by a PSD detector which was mounted parallel to the sample surface and was placed about 1000 mm behind the measured sample. In order to reduce air scattering effects of the reflected beam, the beam path between the sample and detector was set by an evacuated flight tube. Also, to avoid the influence of the very strong specular beam intensity, we slightly moved the PSD out of the specular beam position, i. e. to a higher exit angle with respect to the specular beam. The slit in the front of sample was set to 0.02×2 mm^2, leading to a illuminated area on the sample of 16×2 mm^2. Another slit was mounted on the flight tube with a width of 1 mm in q_z direction. In the present work, a PSD lateral resolution (in q_x direction, or denoted as $q_{||}$ in the text) of 2.1×10^{-3} Å^{-1} was achieved in the direction parallel to the sample surface. With this resolution mean dot-dot distances of up to 300 nm can be determined. Sample azimuthal orientation with respect to the incoming x-ray beam were achieved by rotating sample along its surface normal. We thus were able to record the scattering intensity along different sample azimuths, from which the lateral ordering of QD distribution can be evaluated.

A schematic illustration for the evaluation of QD lateral distribution is given in Fig. 35. It shows the scattering intensity distribution around the whole sample azimuthal orientation from $\Omega = 0^0$ to 360^0, where 0^0 denotes [110] sample azimuth, 90^0 for $[1\overline{1}0]$, 180^0 for $[\overline{1}\overline{1}0]$ and 270^0 for $[\overline{1}10]$ azimuths, respectively. A central black spot represents the specular

beam intensity. The background is indicated as light grey color, and the scattering intensity from QDs is labeled as dark grey color. A disordered case of QD lateral distribution is shown in Fig. 35a, where only a specular beam spot and no contribution of scattering intensity from QDs are found. A linear intensity curve of specular beam intensity derived from the cross-section along [110] direction is also shown there. Fig. 35b is the typical short-range ordering case of QD lateral distribution. It is clearly sketched that in the case of short-range ordering (at larger standard deviation of mean dot-dot distance $\langle\sigma/\overline{d}\rangle$, see Chap. 4, Sec. 4.3) the azimuthal distributed scattering intensity exhibits isotropic distribution, i. e. like a ring structure. In the case of a smaller $\langle\sigma/\overline{d}\rangle$ for QD distribution, there is still a ring-like isotropic intensity distribution, but with a narrow ring width. In both cases, the radius of ring stands for the inverse mean dot-dot distance and the ring width is inversely proportional to the correlation length of QD distribution. One feature of isotropic QD distribution with short-range ordering is that the mean dot-dot distances and ring widths do not depend on the sample azimuth. However, as to anisotropic dot distribution, it is more complicated in comparison to the above cases. Usually, two situations are discussed in order to understand dot anisotropic distribution. One is the azimuthal dependent distribution of mean dot-dot distance. The other is azimuthal dependent correlation length and integrated satellite peak intensity distribution of QDs. The long correlation length and large integrated intensity lead to the better ordered InAs QD distribution. Moreover, for the well ordered case, The satellite peaks may appear with high diffraction orders. If the QD lateral distribution has a perfect lattice-like structure, i.e. long-range ordering, then the corresponding scattering intensity peaks locate to the case described by Fig. 35c.

7.4 Results and discussions

7.4.1 AFM results

The AFM measurements were taken with a scan range of 1×1 μm^2. Fig. 36 shows a zoom to the 1×1 μm^2 AFM image. The results are summarized in Table 7.1. A quantitative analysis of the AFM images indicates that the dots exhibit a narrow size distribution. The average dot height and lateral size are determined to about 4$\pm$1 nm and 30$\pm$10 nm

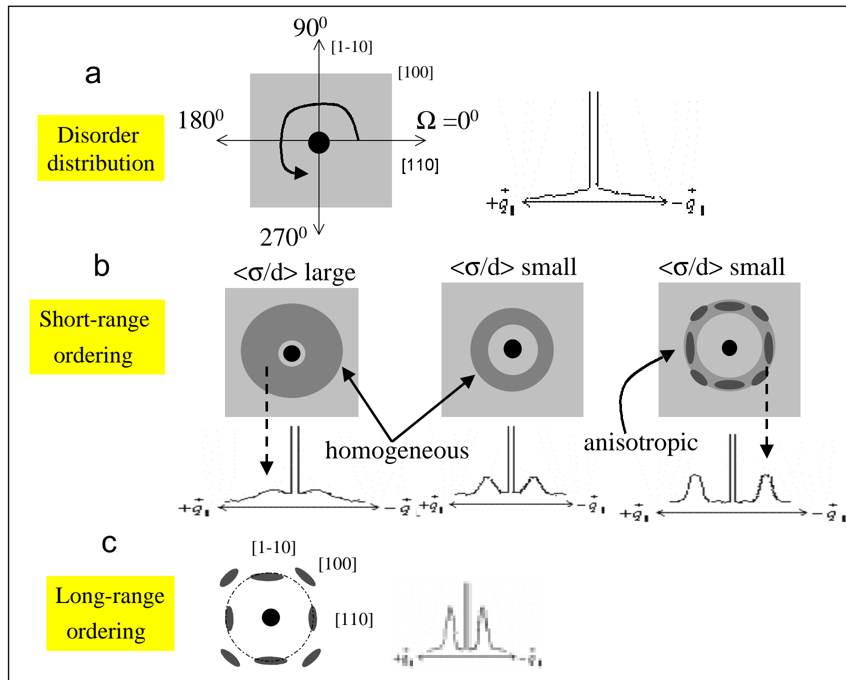

Fig. 35: Schematic illustration of ordering situation in all sample azimuthal orientation for QD lateral distribution with (a) disordered distribution, (b) short-range ordering, (c) perfect lattice-like distribution.

respectively. The dot density is about 3.8×10^{10} cm^{-2}. The lateral ordering of the dots can be evaluated by a one dimensional Fourier transformation of the AFM image. Fig. 37 shows the result for the [110] (a) and [$1\bar{1}0$] (b) directions. We found a weak satellite peak indicated by the arrow as in Fig. 37a, whereas no evidence of the existence of satellite peak was found in Fig. 37b. The existence of the satellite peak is a direct evidence for a short-range ordering of the InAs QDs. From the peak position, we estimate the mean dot-dot distance to be about 67 ± 8 nm in the [110] direction. We note that the above distance is a scale of the laterally periodic distribution or "most frequent" dot-dot separation and it may differ from an average distance determined from the above dot density assuming a perfect square lattice. However, we do not resolve any ordering information in [$1\bar{1}0$] direction. This implies that the ordering of lateral QD distribution is better in [110] than in [$1\bar{1}0$] direction. Moreover, since AFM image scanned only lies in a few μm^2 range, this

leads to no pronounced scattering intensity appearing in Fourier transformation. In order to achieve detailed information about the QD distribution from AFM measurements, one must investigate many AFM images with a large number of QDs, which may provide a pronounced statistic of structure parameters. Also, the shape of the QD facets cannot be determined from our AFM measurements since the size of these dots is beyond our instrumental resolution.

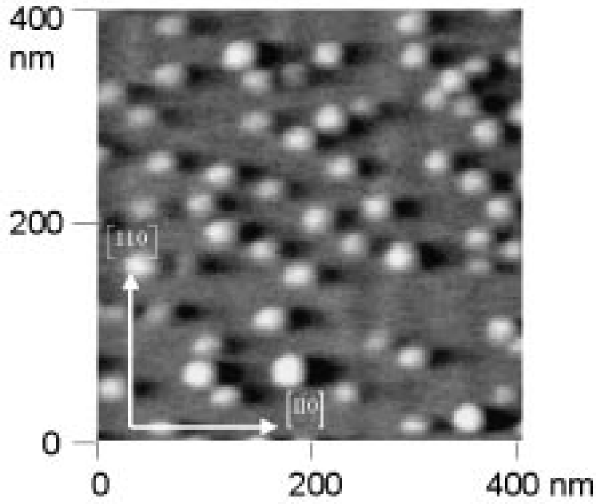

Fig. 36: Typical AFM image of self-assembled InAs QDs with 2.1 ML InAs coverage. Left shading at an angle of 45° to the surface is processed to the AFM image for clarity.

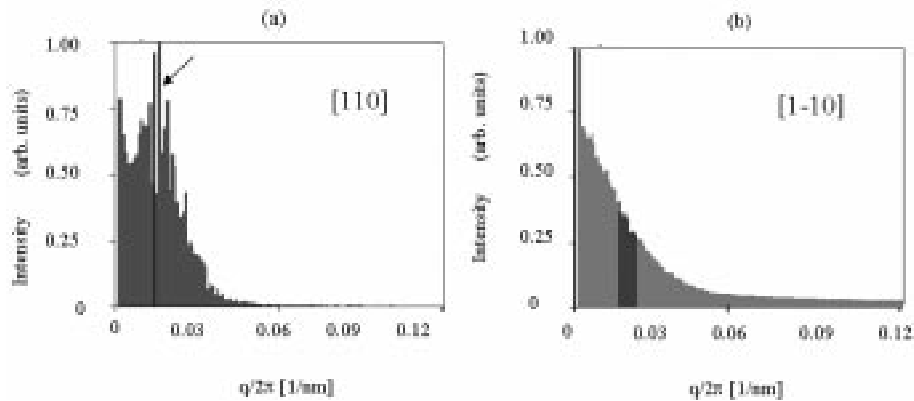

Fig. 37: One dimensional Fourier transformation of $1 \times 1\ \mu m^2$ AFM image for self-assembled InAs QDs in [110] (a) and [$1\bar{1}0$] (b). X-coordinate is the corresponding momentum transfer.

Table 7.1: Comparison of structure parameters for QD lateral distribution determined by AFM and GISAXS.

AFM	[110]	[1$\overline{1}$0]	[100]
dot height $h \pm 1$ (nm)	4		
lateral size ±7 (nm)	30		
mean dot-dot $\overline{d} \pm 8$ (nm)	67	–	–
average dot density $\times 10^{10}$ (cm^{-2})	3.8		

GISAXS	[110]	[1$\overline{1}$0]	[100]
mean dot-dot $\overline{d} \pm 2$ (nm)	64	65	72
standard deviation $\langle \sigma/\overline{d} \rangle$ %	30	30	40
correlation length $L \pm 5$ (nm)	102	102	90
facet family	{111}	{111}	{101}
facet width ±2 (nm)	8	≈8	≈8
average dot height ±1 (nm)	5		

7.4.2 GISAXS results

To further characterize the lateral distribution of self-assembled InAs QDs, GISAXS experiments were performed for different sample azimuthal orientations Ω in an angle range of -10° to 110° in steps of 5°. The sample azimuth Ω is defined and that $\Omega = 0°$ when the [110] direction is oriented parallel to the incoming beam. As the PSD was mounted perpendicular to the incoming beam and parallel to the surface plan, it probes scattering vectors $\overrightarrow{q}_{||}$ (and thus structural properties, e.g. at $\Omega = 0°$ in the [1$\overline{1}$0] direction). From the diffuse scattering spectra in all azimuths, we find the existence of nonspecular satellite peaks. These satellite peaks are located nearly symmetrically at both sides of the specular beam ($q_{||}$=0 Å^{-1}) and can be clearly resolved. Since no satellite peaks are found in GaAs reference samples, these peaks can be attributed to diffuse scattering from the InAs QDs. We present GISAXS profiles in Fig. 38 for $\vec{q}_{||}$ parallel to [110], [1$\overline{1}$0], and [100] as an example. Fig. 38 clearly shows high order satellite peaks in these three azimuths, i. e., ±1, ±2, ±3 orders, indicating that the dot arrangement is well ordered.

The mean dot-dot distance $\overline{d}$ is determined by the first satellite peak position with respect to the origin, i. e., $\overline{d} = 2\pi/q_{||}$. In [1$\overline{1}$0] and [110] directions we find the same value $\overline{d} = 64 \pm 2$ nm, whereas in [100] direction the data yields $\overline{d} = 72 \pm 2$ nm. We thus

determine the ratio $R = \overline{d}_{100}/\overline{d}_{110} \sim 1.13$. Intrinsically, a value of $R = 1.0$ is expected for an isotropic dot distribution. Hence $R = 1.13$ reflects the presence of anisotropy in the ordering of the QDs. The anisotropy is smaller than in a perfect square-like lattice for which $R = 1.41$ is expected.

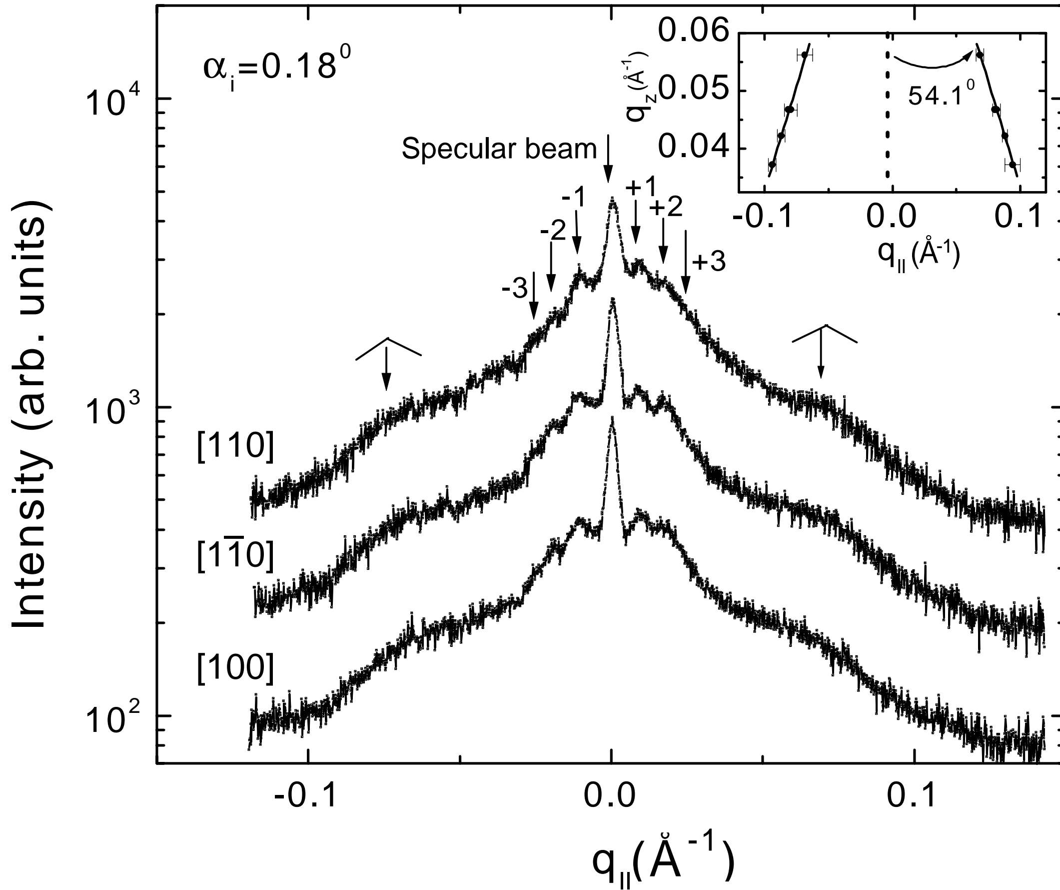

Fig. 38: Logarithmic GISAXS intensities along different $\vec{q}_{||}$-directions as indicated at each profile. (At incidence angle $\alpha_i = 0.18°$ and exit angle $\alpha_f = 0.40°$.) The central peak at $q_{||} = 0$ is generated by the specular beam. The satellite peaks with higher orders are indicated by ±1, ±2, ±3. Additional broad facet spots at $q_{||} = \pm0.07\,\text{Å}^{-1}$ are indicated by $\wedge$-signs. The inset depicts the position of these facet spots in the $q_{||}$–q_z space (recorded at fixed α_i).

Using an appropriate fit function and deconvolution algorithm, we can determine the full width at half maximum (FWHM) values of the first order satellite peaks. From AFM

measurements at different surface spots, there is no evidence for large scale fluctuations of the QD density. We thus regard the finite width of the satellite peaks to originate from local disorder among the nearest neighbors of each dot row in the chosen azimuth. With this assumption, correlation lengths of the dot distribution [Sch98] can then be obtained, which quantitatively reflect the degree of ordering in the lateral dot distribution. We find that the standard deviation of the dot-dot distance [Wol95] in $[1\bar{1}0]$ and [110] direction equals to 30 %, whereas along [100] it is 40 %. Assuming a short range order mode of the correlation function [Sch98], we then calculate the correlation length of $L = 102 \pm 5$ nm along $[1\bar{1}0]$ and [110] directions and $L = 90 \pm 5$ nm along [100], respectively. In combination with a larger mean dot-dot distance along [100] direction this suggests a much weaker ordering along [100] than in $[1\bar{1}0]$ and [110] directions.

The integrated intensities of the satellite peaks as a function of the azimuthal orientation are presented in fig. 39. The intensity values are normalized to the corresponding specular beam intensities and have three maxima located at angles of 0°, 45°, and 90°, respectively. These maxima reflect the anisotropic enhanced azimuthal ordering of the lateral dot distribution in $[1\bar{1}0]$, [100] and [110] directions. We note that there is a higher intensity and a more narrow azimuthal peak width (about 20°) in [110] direction as compared to $[1\bar{1}0]$ and [100] in fig. 39. Although for both [110] and $[1\bar{1}0]$ direction we find the same mean dot-dot distance and correlation length, this difference clearly indicates a better azimuthal ordering of the dot arrangement along [110] than along $[1\bar{1}0]$ direction. We note that this observation is in agreement with our AFM Fourier analysis. The anisotropic lateral ordering of QDs may be caused by an anisotropic strain field around the QDs, in correspondence to previous studies on islands in InAs films below the critical thickness [BH94].

In addition to the satellite peaks we find broad maxima in the GISAXS spectra, located at $q_{||} = \pm 0.07$ Å^{-1} and marked by $\wedge$-signs in Fig. 38. We have investigated the dependence of the $q_{||}$-peak position on q_z for $\vec{q}_{||}$ parallel to $[1\bar{1}0]$, [110] and [100], respectively. An example is shown in Fig. 40a in $[1\bar{1}0]$ direction, where GISAXS intensity curves were recorded at different q_z values. We clearly see the arrows denoted peak maximum positions shift towards to small $\pm q_{||}$ with respect to the reference dotted line. We measure the corresponding maximum positions $q_{||}$ and q_z, and plot them in $q_{||} - q_z$ space.

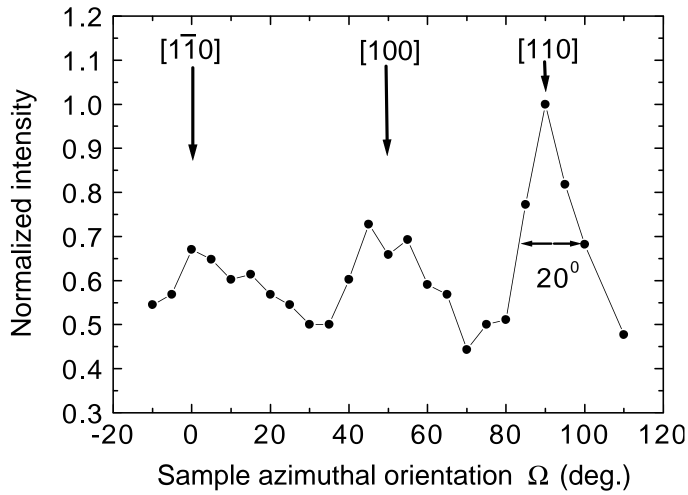

Fig. 39: Integrated satellite peak intensity versus sample azimuthal orientation Ω. Satellite intensities have been normalized by the corresponding specular beam intensity.

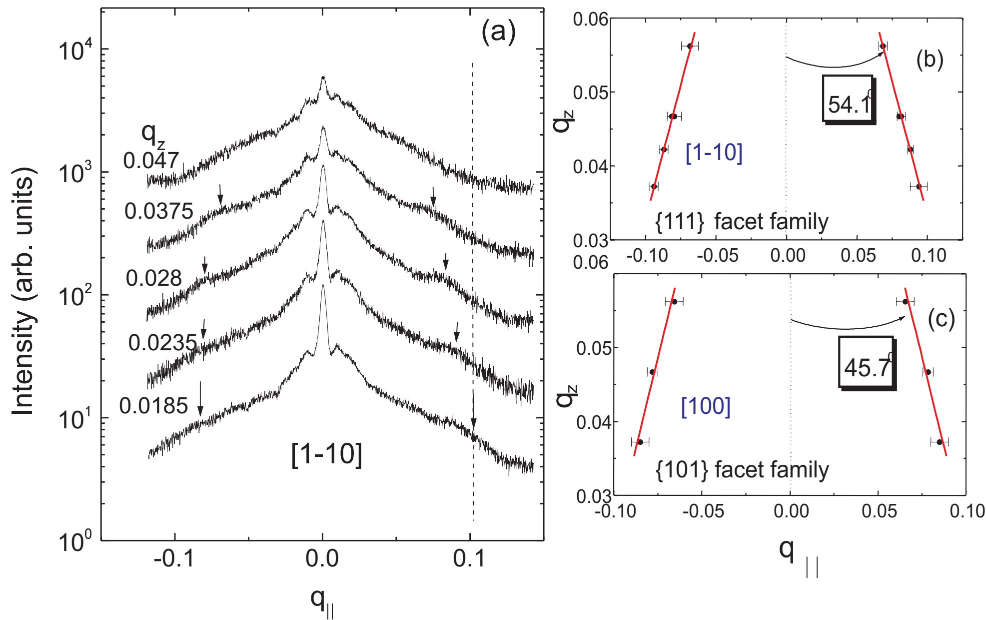

Fig. 40: GISAXS intensity at different q_z values are shown in (a) for $q_{||}$ in [1$\bar{1}$0]. (b) and (c) show the CTR facet peak positions in $q_{||} - q_z$ for $q_{||}$ in [1$\bar{1}$0] and $q_{||}$ in [100] directions, respectively.

Fig. 40b, c show the peak positions for $\overrightarrow{q}_{||}$ in [1$\bar{1}$0] and [100] direction. The inset of Fig. 38 shows an example for the [110] direction. The peak positions can be described by a linear relation in the $q_{||}$–q_z space. This suggests that these broad intensity maxima are associated with crystal truncation rods of the QD facets. The inclination angle of 54.1° with respect to the [001] surface normal strongly suggests that the peaks observed originate from {111} QD facets. The same facet family is also observed for $\vec{q}_{||}$ parallel to [1$\bar{1}$0] (54.1^0), whereas in [100] direction {101} facets (45.7^0) are found. The observed facet spots originate from higher order Bragg points and do not merge at (000) but at a finite q_z-value. This points to a partial strain relaxation within the InAs dots.

From the present experimental results, we propose that the InAs QDs are truncated pyramids with an octagonal basis and facet families of {111} and {101}, in agreement with finite element calculations [Mol98] and transmission electron microscopy (TEM) studies by Grundmann et al [Gru95a] and by Chu et al [Chu99]. In the literature a number of different experimental techniques has been employed to gain information on the dot geometry among which the most important are TEM [Gru95a, Chu99], atomic force microscopy (AFM) [Leo94, Kob96, Moi94], scanning tunneling microscopy (STM) [kX99, Joy98], and RHEED [Nab94, Lee98]. Yet, at present no consistent picture can be composed from the results reported. This may be caused by the fact that the contrast resolved by the different techniques originates from different physical properties. Moreover, even authors using the same technique propose different facets, which may indicate that the dots investigated are under different growth conditions like e.g. different growth temperature, InAs deposit thickness, and different interdiffusion of In and Ga in the dots. In addition, from the FWHM of the facet CTR peaks an estimation can be given for the average facet size [Sch98, Son94]. We assume that the facet CTR induced broad peak is of a Lorentzian profile, and the instrumental peak shape is a Gaussian profile. The exact facet size induced peak FWHM value can be obtained from a deconvolution of the measured broad peak with the instrumental peak, i. e. $W = 5.9/[cos(\theta_{facet}) \times \triangle q_{||}]$, where W represents the facet size, θ_{facet} is the facet angle with respect to the surface normal [001], and $\triangle q_{||}$ is the above deconvoluted FWHM value. In our case we calculate a facet size of approximately 8±2 nm, and from this, a dot height of about 5 nm, which is consistent with our AFM data. Finally, in Fig. 41 we show the sketched QD shape as determined from GISAXS.

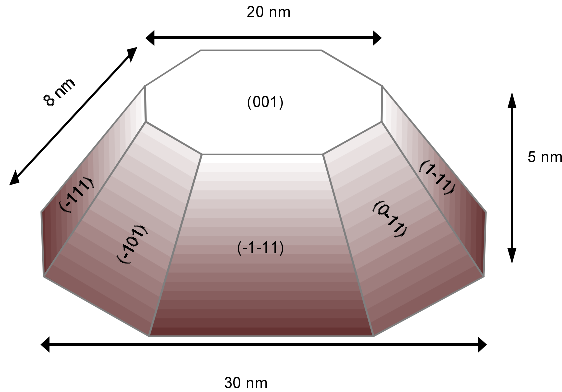

Fig. 41: The sketched InAs QD shape. The bottom size is observed from AFM image. The facet family and size are determined from GISAXS experiments. The dot shape is determined as a octagonal-based pyramid truncated by (001) plane.

7.5 Summary

We present GISAXS experiments that for the first time reflect lateral ordering in a single layer of self-assembled InAs QDs on GaAs(001). Furthermore, in our experiments facet CTR peaks are observed from which the dot facet shape can be inferred. Enhanced lateral ordering of the InAs QD distribution is found along $[1\bar{1}0]$, [110] and [100] directions. We derive a mean dot separation of 64 nm in <110> like directions. The azimuthal dependence of the GISAXS intensity points to an anisotropic dot distribution with a large dot separation and a small correlation length in <100> like directions. Moreover, the azimuthal dot distribution function is sharper in [110] than in other directions. This may indicate the presence of an anisotropic strain field around QDs. The shape of InAs QDs is determined as a truncated octagonal-based pyramid.

Chapter 8

Ordering Study on Self-assembled Capped InAs QDs

Novel GISAXS experiments have been performed on self-assembled InAs QDs grown by MBE. In the present work, we focus on the characterization of the lateral dot distribution in a single dot layer buried beneath a 6 or 10 nm GaAs cap layer. The sample growth procedure is the similar to that described in the last chapter. The InAs deposit was chosen to 2.2 ML. As soon as the InAs deposition was finished, a 6 or 10 nm-thick GaAs layer was deposited at the same substrate temperature in order to cap the InAs dot layer. For the GaAs cap growth, we utilized 2 As-flux cells, each of which has pressure of 5×10^{-6} mbar. The main purpose of this utilization is that we expect to reduce interdiffusion and intermixing between In and Ga atoms during capping. Prior to GISAXS experiments, we investigated the morphology of sample surface by using *ex situ* AFM as shown in Fig. 42. No evidences for the existence of InAs QD morphology were found, which may imply that the InAs QDs are possibly capped beneath the GaAs layer. This seriously obstacles the AFM investigation on buried InAs QD lateral distribution. In contrast to AFM, GISAXS makes it possible to investigate the structural property of the buried InAs QDs.

The GISAXS experimental setup is sketched in Fig. 43. Again, the lateral resolution of the setup is $2.1 \times 10^{-3} \AA^{-1}$. Accordingly mean dot-dot distances up to 300 nm can be determined. $\alpha_i = 0.26^0$, is the incidence angle. At this angle the x-ray penetrates into the sample by a depth of more than 10 nm. α_f is the reflection angle. The intensities are recorded by PSD detector. Scattering vector $\overrightarrow{q_{||}}$ is perpendicular to azimuthal orientation. Since in the present sample the surface roughness is determined by AFM to be about 1

nm, the reflection intensity from such surface, i.e. the specular beam intensity, is very strong comparing to the uncapped case. In order to get rid of such strong intensity, we move PSD to a large exit angle of $\alpha_f = 0.8^0$. Ω is the sample azimuthal orientation angle.

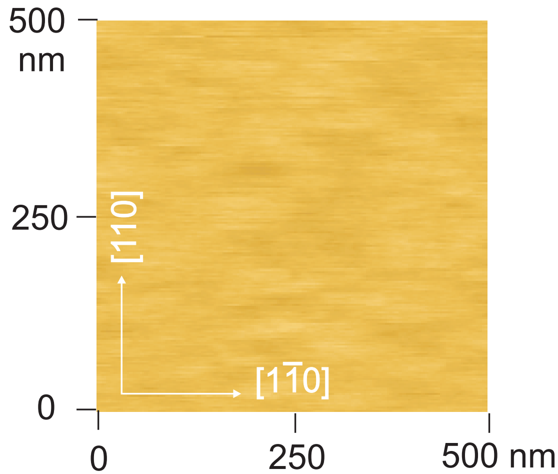

Fig. 42: AFM image on capped InAs QDs. The image size is $500{\times}500$ nm^2. The surface roughness is determined to be about 1 nm.

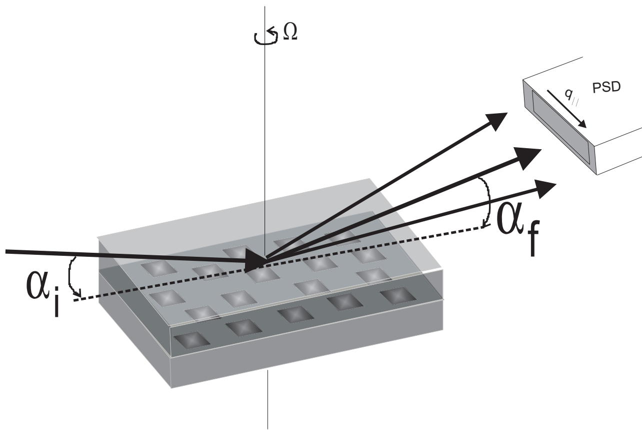

Fig. 43: Schematic GISAXS experiment on buried InAs QDs.

The central, bright and narrow line in Fig. 44 represents the specular beam intensities for all measured azimuths. In addition, non-specular diffuse scattering satellite peaks are found at symmetric positions of both sides of the specular beam for all measured azimuthal orientations i. e. $0^0 - 150^0$ in Fig. 44a (with 6 nm GaAs cap layer) and $0^0 - 180^0$ in Fig. 44b (with 10 nm GaAs cap layer) with respect to the incoming beam. They are attributed to the diffuse scattering of the buried InAs QDs. By means of the image

contrast labeled at the right side of Fig. 44, in the measured azimuthal range, the highest satellite peak intensity is found at azimuth around 0^0 for case (a), and 0^0 and 180^0 for case (b). These azimuthal orientations are associated to [110] direction for both (a) and (b) cases. Moreover, the largest distance between satellite peak and specular beam in both cases is also found around [110] direction. Qualitatively, we observe that the azimuthal dependent satellite peak intensity and position distributions are anisotropic. Here, we note that the main difference between (a) and (b) is the different GaAs cap thickness. In both cases, the variation of the azimuthal dependent satellite peak intensity is the same but different intensity scale, which is due to the different cap layer thickness. We thus stress on the analysis of sample with 10 nm cap layer, i. e. (b) case. For comparison, we also show the satellite peak intensity distribution of uncapped InAs QDs in Fig. 44c with Ω=$-25^0 -\ 135^0$, from which we found that the satellite peak intensity is inhomogeneous and the highest intensity is located in [110] direction. Although the lowest intensity is found at around $[1\overline{1}0]$ direction, it is still clearly observable in comparison to the (a) and (c) cases.

In Fig. 44b, the most pronounced satellite peak intensity is observed along $[1\overline{1}0]$ azimuth, where the corresponding diffuse scattering vector $\overrightarrow{q_{||}}$ is parallel to [110] direction. This significantly concentrated distribution of satellite peak intensity indicates a strong anisotropy of QD lateral distribution. We quantitatively analyze the diffuse scattering spectra with $q_{||}$ for all measured sample azimuths. As an example, we show the scattering spectra for $q_{||}$ in [110], $[1\overline{1}0]$ and [100] directions in Fig. 45a and Fig. 45b. By fitting the satellite peak with Eq. 3.15 and specular beam intensity with a Gaussian function as shown in the inset of Fig. 45a and b, we derive the structure parameters concerning of the QD lateral distribution. The mean dot-dot distances $\overline{d}$ of the InAs QD lateral distribution are determined to be anisotropic. The shortest one is around [110] $\pm 15^0$ direction i. e. $\overline{d}$=76 ± 2 nm, whereas, in other measured azimuths $\overline{d}$ values are approximately the same. For instance in $[1\overline{1}0]$ direction $\overline{d}$=122 ± 20 nm and in [100] direction $\overline{d}$=126 ± 20 nm. From these, we infer that the anisotropy of the lateral QD distribution is only along [110] direction. Moreover, we obtain the standard deviation of the dot-dot distance $\langle \sigma/\overline{d} \rangle$ for all measured azimuths. We get $38 \pm 2\%$ in [110] direction, and $60 \pm 5\%$ in other azimuths, e. g. in $[1\overline{1}0]$ and [100] directions. Assuming short range order type of the correlation function [Sch98, Zha00], this implies correlation lengths of 80 nm in [110], and 50 nm in other azimuths e. g. $[1\overline{1}0]$ and [100] directions, respectively. As we know, the longer the correlation length, the better the QD lateral ordering. The correlation length is inversely proportional to the standard deviation $\langle \sigma/\overline{d} \rangle$ value. We suggest that the QD

lateral distribution is better ordered in [110] direction.

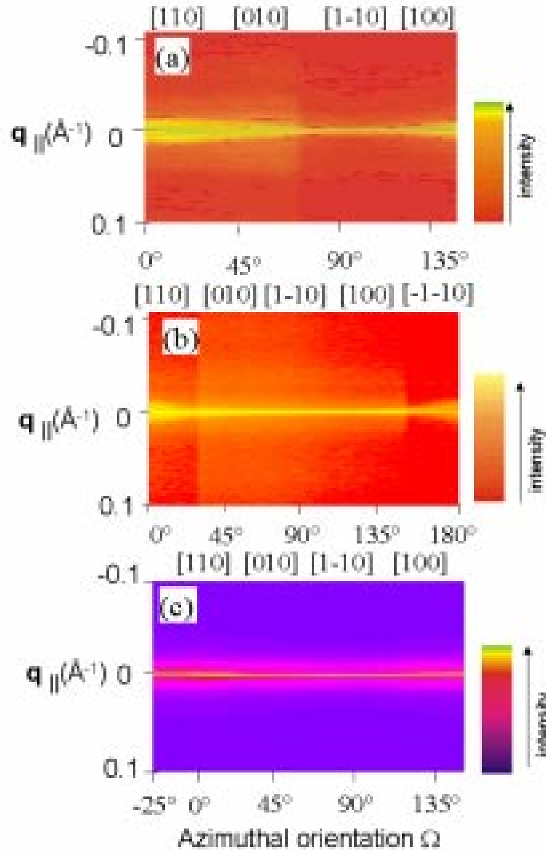

Fig. 44: Grey scale plots of the GISAXS intensity versus the scattering vector and sample azimuthal orientations. $[1\bar{1}0]$ azimuth is set to 0^0 azimuthal orientation. On top of the figure the direction of the scattering vector $\vec{q_{||}}$ is indicated. (a) is for buried QDs with 6 nm GaAs cap; (b) for buried QDs with 10 nm GaAs cap, (c) for uncapped QDs.

From the analysis of the structure parameters such as satellite peak intensity, mean dot-dot distance, standard deviation of the mean dot-dot distance, and correlation length, we conclude that the lateral distribution of the buried InAs QDs is strongly anisotropic and better ordered in [110] direction, which is consistent with the distribution found in uncapped dot samples [Zha00]. In addition, from GISAXS intensity curves, no evidences are observed for the existence of dot facets in comparison to that of the uncapped dots [Zha00]. It may suggest that the dot facets are highly disturbed by the GaAs cap layer. In addition, we note that the present experiments in this chapter do not imply any influences of GaAs cap layer to InAs QD lateral distribution, since the buried QD samples have different growth conditions in comparison to the uncapped QD samples discussed in Chap. 7.

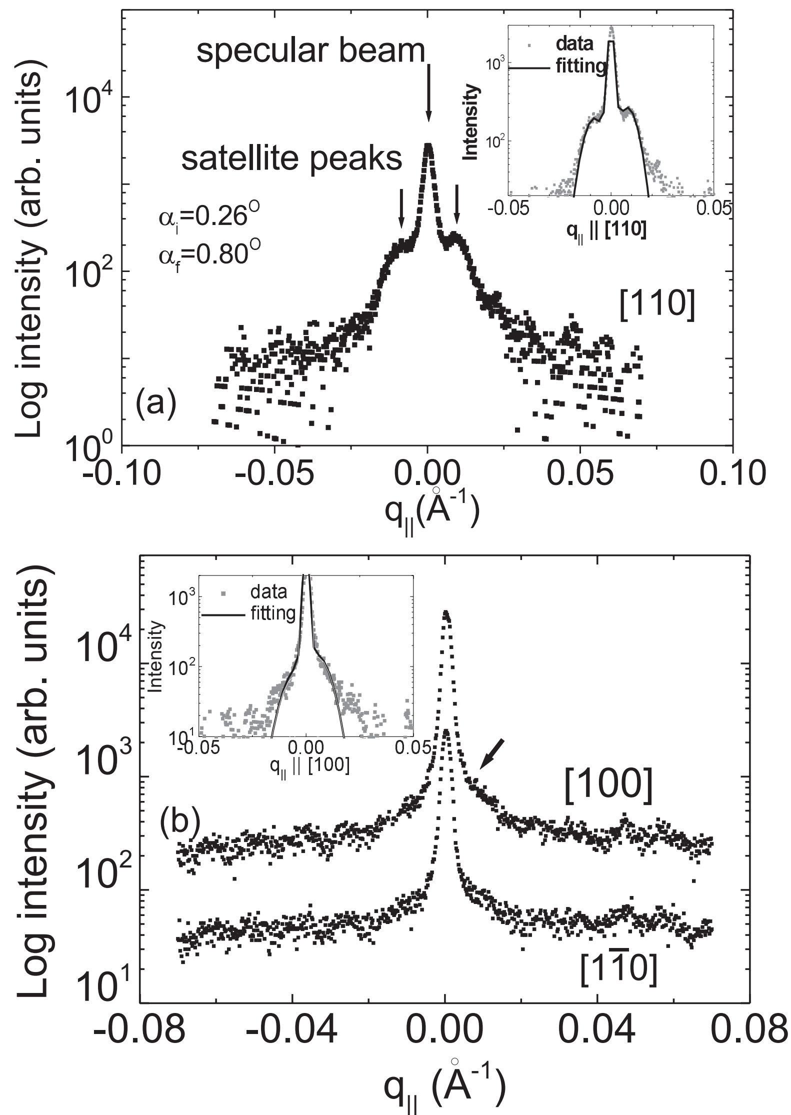

Fig. 45: Logarithmic GISAXS intensity curve versus $q_{||}$ along (a): the [110] and (b): [100], $[1\bar{1}0]$ directions. The incidence angle is 0.26^0, and the reflection angle is 0.8^0. The specular peak is located at $q_{||} = 0(\AA^{-1})$. In (a) case, two satellite peaks are symmetrically distributed beside the specular peak. The inset in (a) represents a fitting to the data. In (b) case, only very tiny scattering intensity from QDs is observed as indicated by an arrow. The inset in (b) indicates a fitting to the measured data.

Chapter 9

Strain Status of Self-assembled InAs QDs

GIXRD experiments employing the asymmetric (202) and/or $(0\bar{2}2)$ Bragg diffractions have been performed to characterize self-assembled InAs QDs grown by molecular beam epitaxy. We find that the strain is elastically relaxed with different components in all measured samples. In addition a small volume fraction of relaxed $In_xGa_{1-x}As$ is found in samples grown with lower As-flux values.

9.1 Research focus

Structural [Gru95b, Mol98, Xie95, Keg99, Sch97, Rub96, Zha00] and opto-electronic [Leo93, Mil97, Dre94, Fri96] studies have been done for self-assembled InAs QDs. It is presently thought that the island formation is entirely driven by the strain originating from the lattice mismatch between InAs and GaAs [Dar97]. Moreover the electronic states are strongly dependent on the strain status of the dots [Gru95b]. On the other hand so far only very few experiments exist that yield quantitative information on the strain of the dots [Gru95b, Keg99, Dar97]. From conventional high resolution x-ray diffraction of single or multiple InAs QD layers an average strain value has been deduced [Gru95b, Dar97]. However, from the conventional diffraction experiments, it is very difficult to obtain detailed information on the strain distribution inside the InAs QDs due to intensity problems.

In the present work, we address the strain status of the material inside the InAs QDs. We report GIXRD experiments on uncapped InAs QD single layer samples. The grazing incidence technique strongly enhances the intensity of the InAs QDs in comparison to the conventional x-ray techniques. In combination with high flux synchrotron radiation this allows us to map out the diffraction intensity in reciprocal space in the vicinity of the GaAs (202) or $(0\overline{2}2)$ Bragg diffraction spots. Previously, Kegel et al [Keg99] used this technique at the in-plane (220) Bragg diffraction spot and analyzed their results using a so called iso-strain model in order to determine a strain distribution within the dots. In comparison, our scattering geometry has several advantages. In our case the diffraction intensity of the InAs QDs is well separated from the diffuse intensity of the GaAs (202) or $(0\overline{2}2)$ substrate Bragg peak. Furthermore, we are able to distinguish the diffraction intensity between the strained pure InAs and intermixed $In_xGa_{1-x}As$, which cannot be resolved by GIXRD in the in-plane diffraction geometry. Thus we can determine the role of intermixed $In_xGa_{1-x}As$. Recently it was reported from a scanning tunneling microscopy (STM) study that the intermixing inside the InAs QDs at common growth temperatures, i. e. 420°C≤T≤500°C, is strong [Joy98].

9.2 Sample preparation

Sample growth procedure is described in Chap. 5. Two types of samples are discussed in this chapter. For the first type of samples, we choose the growth temperature of 450°C within the temperature range mentioned in Joyce's work [Joy98]. The corresponding As-flux was controlled to be about $7 - 8 \times 10^{-6}$ mbar. As to the second type of samples, the growth temperature is 500^0C with As-flux of approximate 1×10^{-5} mbar. For both types, the InAs deposit corresponds to a coverage of 2.3 monolayers (ML) so as to get large InAs QD size. The critical thickness for dot formation is found to occur at about 1.5 ML for the first type, and 1.8 ML for the second type as monitored by RHEED. The InAs QD topologies are observed by AFM for both types of samples, in which the average dot height is determined to be about 8 for the first type and 10 nm for the second type. As an example, we show AFM image for the first type of samples in Fig. 46.

9.3 GIXRD experimental

GIXRD measurements have been performed at the undulator beamline BW1. The wavelength was chosen to be 1.17 Å. The incidence angle was set to 0.15°, which is smaller than the total external reflection angle of 0.23°. The sample area illuminated by the incoming beam was 16×2 mm^2, providing sufficient statistics on a large number of dots. A PSD detector was mounted parallel to the sample surface with a lateral resolution in reciprocal space of 2.1×10^{-3} Å^{-1}. For the first type of samples, scans of the vertical scattering vector q_z near the GaAs (202) Bragg reflection have been performed in a range between q_z=1.70 and 2.0 reciprocal lattice unit (rlu). For the second type of samples, we have performed GIXRD experiments on (202) and $(0\overline{2}2)$ Bragg diffractions, respectively. The q_z scan range is in q_z=1.65-2.05 r.l.u.. For the details of GIXRD principle, please refer Chap. 3, and Chap. 4.

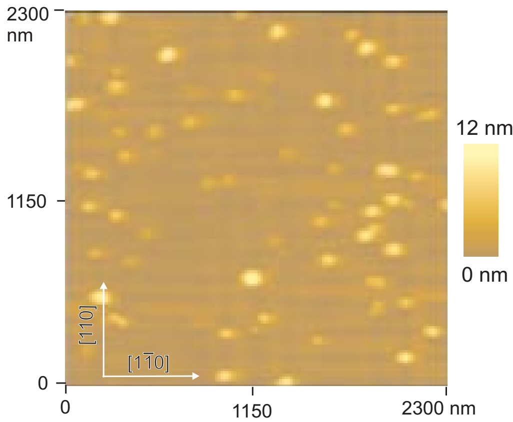

Fig. 46: AFM image for InAs QD topology. The sample was grown at substrate temperature of 450^0 C.

9.4 Results and discussions

9.4.1 The first type of samples

We present a three-dimensional plot of the scanning data as shown in Fig. 47. The diffraction intensity is plotted with respect to the q_x and q_z which are denoted as scattering vectors in the reciprocal space. $(q_x, q_z) = (2, 2)$ represents the GaAs (202) Bragg diffraction. The broad intensity peak located at smaller q_x and q_z value results from

strained InAs QDs. A white arrow indicates additional diffraction intensities appearing near GaAs (202) Bragg peak.

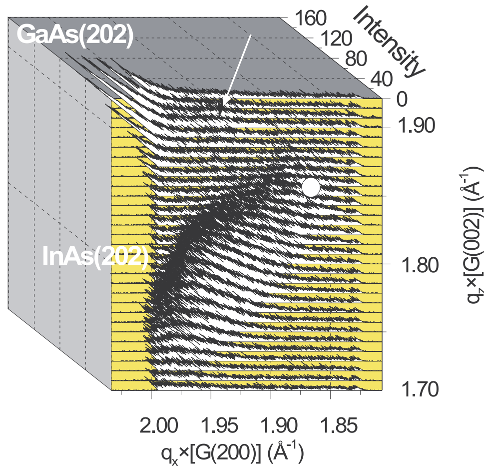

Fig. 47: 3-dimensional plot of GIXRD (202) diffraction intensity in reciprocal space $q_x - q_z$ for InAs QDs on GaAs (001) substrate. A white circle denotes the diffraction condition expected for a bulk-like InAs crystal. A white arrow indicates the intensity from intermixed $In_xGa_{1-x}As$.

For clarity, a reciprocal space map was composed showing the scattering intensity contour as a function of q_x and q_z. In order to magnify the diffraction intensity from the strained InAs QDs, a zoom of the map is presented in Fig. 48, where the scattering intensity is displayed in grey scale. Here, $(\Delta q_x, \Delta q_z) = (0, 0)$ rlu corresponds to the GaAs (202) Bragg spot. A broad diffraction spot in the center of the figure is observed. The black dot in the figure indicates the diffraction point expected for totally relaxed InAs, i.e. $(\Delta q_x, \Delta q_z) = (-0.135, -0.135)$ rlu. One can clearly see that most diffraction intensity is continuously distributed between this point and the position of $(0, -0.263)$ rlu at which the diffraction intensity of the fully strained InAs matching to the GaAs substrate would be expected. The maximum intensity is located half way in between these two points. The observation of the broad scattering peak in reciprocal space clearly points to the presence of InAs QDs with a partial strain relaxation inside. The broadening of the spot in q_x and q_z orientation can be explained by the finite size of the volume elements at given strain states.

From the position distribution of intensity maxima in reciprocal space we are able to deduce the strain state and composition inside the dots. The wetting layer is not accessible to x-ray diffraction. Firstly, it expands only over a few atomic layers. This leads to very broad features in reciprocal space, i. e. in q_z. Secondly, the wetting layer is likely fully oxidized as it was uncapped during the experiments. In Fig. 49 we plot the intensity

maxima positions (full circles) as determined from Δq_z cuts of the data in Fig. 48. The cuts were taken along Δq_z direction in order to account for the aspect ratio of the InAs QDs and avoid strong finite size effects. The distribution of the peak positions (full circles) has a linear relation in Δq_x-Δq_z space, which is in good correspondence to the elastic strain function represented by the solid line, i.e. $\Delta q_z = \beta - \alpha \cdot \Delta q_x$, where $\beta = -0.263$ and $\alpha = 0.945$ as calculated by elastic theory for the strained bulk like InAs [Nye57]. The present position distribution confirms that this broad scattering peak in Fig. 48 is contributed entirely by the strained InAs components inside QDs.

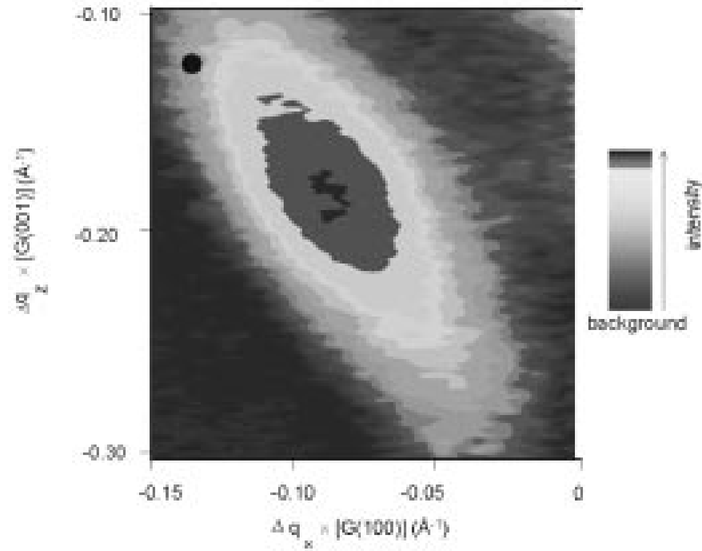

Fig. 48: Reciprocal space Δq_x-Δq_z map of GIXRD (202) Bragg diffraction for InAs QDs on GaAs substrate (001). The black dot is the expected diffraction position for bulk-like InAs (totally relaxed InAs). G(100)=$2\pi/a_\circ^{GaAs}$, where $a_\circ$=5.65 Å, is the GaAs lattice constant.

The scattering intensities at both extreme positions of totally relaxed InAs as well as InAs almost fully matched to GaAs are very small. In particular, the almost complete absence of fully strained InAs (i.e. the position in the reciprocal space at $(\Delta q_x, \Delta q_z) = (0, -0.263)$) is surprising in view of the matching between the InAs dots and the GaAs substrate. This puzzle may possibly be resolved by the existence of intermixed $In_xGa_{1-x}As$ at the interface. This however is not directly accessible in the experiment due to the extremely

small thickness of the wetting layer.

Beside the intense peak, a small additional one is found close to the GaAs substrate peak as displayed in the inset of Fig. 49. These scans present the same Δq_x range at different Δq_z values with peaks located at $\Delta q_x = -0.06$ rlu. The separation in Δq_z allows to distinguish between strain and composition effects. Open circles in Fig. 49 denote the peak positions of the diffraction intensity for the intermixed $In_xGa_{1-x}As$ in the Δq_x-Δq_z plane. The dashed line indicates the positions of $\Delta q_z = \Delta q_x$ as expected for unstrained $In_xGa_{1-x}As$. The positions of the intensity maxima can be resolved in the range of $(-0.06, -0.06)$ rlu $\leq (\Delta q_x, \Delta q_z) \leq (-0.03, -0.03)$ rlu, corresponding to an In content x in the range of $0.21 \leq x \leq 0.42$. Outside this range the scattering intensity can hardly be measured as the peak merges either into the background or into the diffuse intensity of the GaAs (202) peak.

Hence, the data show a large contribution from partially strained InAs and a small one from unstrained $In_{1-x}Ga_xAs$. However no evidence is found for the presence of partially strained $In_{1-x}Ga_xAs$ which would result in intensity in between the dashed and the full line of Fig. 49.

The almost complete absence of fully strained InAs is in contrast to the interpretation infered from GIXRD data taken in the vicinity of the in-plane GaAs (220) Bragg spot [Keg99]. However, in that experiment overlap of the InAs diffraction intensity with the strong (220) GaAs Bragg spot renders a determination of the intensity behavior for $\Delta q_x, \Delta q_y \to 0$ impossible.

In order to derive the volume fraction between the $In_xGa_{1-x}As$ alloy and strained InAs structure inside dots, we integrate the respective diffraction intensities over the measured area in the reciprocal space. The volume fraction of relaxed $In_xGa_{1-x}As$ vs. partially strained InAs is directly proportional to the ratio of the corresponding integrated intensities of the diffraction peaks. Using this relation, we obtain a value of 3% for the relative volume fraction of the intermixed $In_xGa_{1-x}As$. For principle reasons, however, this calculation excludes the wetting layer as explained above. The volume fraction of $In_xGa_{1-x}As$ is small in comparison to the findings reported previously, however this discrepancy may be explained by differences in temperature measurements, placing our growth conditions at the low temperature side in the range of Joyce et al. [Joy98] who reported substantial Ga intermixing into the InAs QDs at higher growth temperatures.

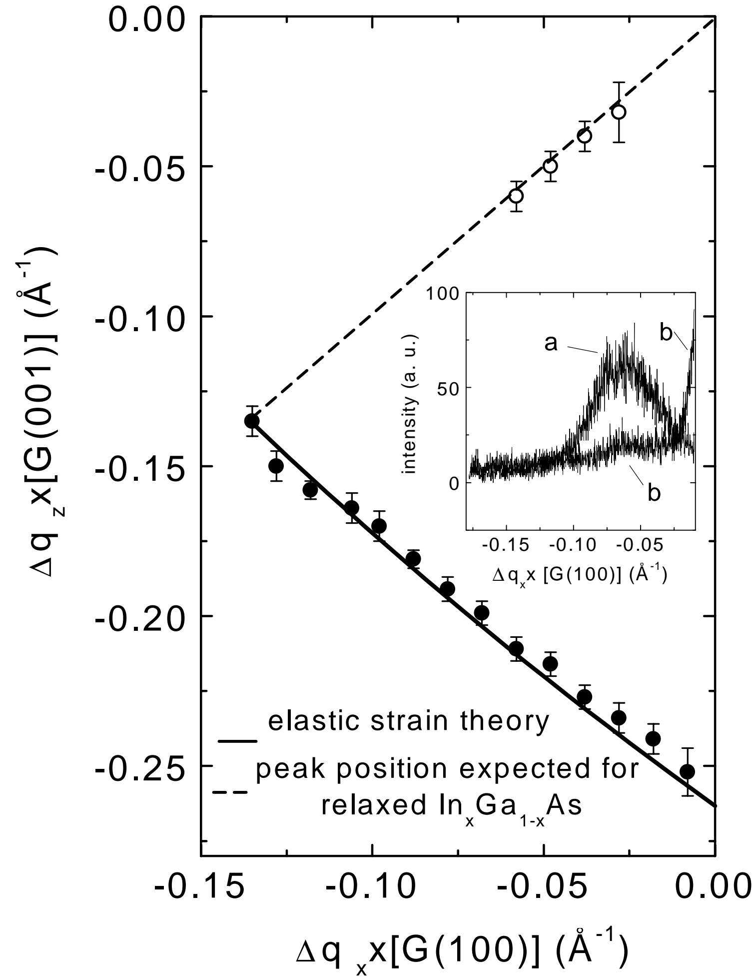

Fig. 49: The position distribution of GIXRD intensity maxima in Δq_x-Δq_z space. Full circles denote the strained InAs, open circles represent the intermixed $\mathrm{In}_x\mathrm{Ga}_{1-x}\mathrm{As}$ alloy. The inset is an example for the distinction of GIXRD intensities between the strained InAs (a) and intermixed $\mathrm{In}_x\mathrm{Ga}_{1-x}\mathrm{As}$ (b) with the same Δq_x range, a: $\Delta q_z = -0.21$ rlu, b: $\Delta q_z = -0.06$ rlu. G(100)=$2\pi/\mathrm{a}_\circ^{GaAs}$

From Fig. 48 we can determine the maximum peak intensities for the strained InAs (full circles in Fig. 49) as a function of the lateral strain component ε_x and shown in Fig. 50a.

As the measured peak intensity is proportional to the square of the number of crystal unit cells, we calculate the volume fraction $f_x \cdot \triangle\varepsilon_x$ of the different strain components normalized to the InAs QD volume, as shown in the inset of Fig. 50a. The distribution of these intensity maxima can be described by a Lorentzian function. The maximum value and hence the dominant volume fraction of strained InAs is found at strain values around $\varepsilon_x = 3.5\%$ and the volume fraction of both totally relaxed and almost fully strained InAs is quite small. This is in contrast to the assumption of an iso-strain model used by Kegel et al [Keg99] for the interpretation of their data obtained by in-plane x-ray diffraction. We also show the peak intensity maxima of $In_xGa_{1-x}As$ alloy *vs.* different In compositions in Fig. 50a indicated by open circles. Again, the lower peak intensity maxima of the $In_xGa_{1-x}As$ structure comparing to the strained InAs crystal is due to the small volume fraction of $In_xGa_{1-x}As$ structure.

Based on the experimental evidence of the elastic strain relaxation, we determine the elastic strain energy inside InAs QDs. As we know from elastic theory [Nye57], the elastic energy density e for strained crystal is given by: $e=\frac{1}{2}C_{ij}\varepsilon_i\varepsilon_j$ $(i,j=1,2,3)$, where C_{ij} represents stiffness constants of the crystal, $\varepsilon_{i,j}$ represents the elastic strain state, $\varepsilon_1=\varepsilon_2=\varepsilon_x$ is for the lateral strain states, and $\varepsilon_3=\varepsilon_z$ for the vertical strain states. For each strain component, e can be calculated and shown in the inset of Fig. 50b. Considering the effect of the normalized volume fraction for different strain components, we calculate the elastic energy distribution inside InAs QDs as shown in Fig. 50b (full squares). It essentially reflects the experimental strain energy inside InAs QDs. Therefore, the present results make it possible to replace the theoretical models [Mol98] of the assumption on elastic strain energy for further calculation.

From transmission electron microscopy it is known that QDs with small size as investigated here are free of dislocations [Leo93]. Moreover, our data indicate elastic strain relaxation inside the InAs QDs. On the other hand, we only find an almost vanishing fraction of the InAs to show the in-plane GaAs lattice constant, i.e. fully strained InAs. Hence, the adjustment of lateral lattice parameters between the substrate and the InAs QDs must be accomplished by an interlayer at the interface. This points to an enhanced intermixing of Ga and In near the interface which also might affect and be triggered by the wetting layer.

In addition, we have performed (202) Bragg diffraction in $q_x - q_z$ reciprocal space for samples grown at 500^0C with As-flux of approximate 4×10^{-6} mbar. The preliminary results indicate that the strain relaxation of the InAs QDs are elastic as well. However, there ex-

ists low scattering intensity with intensity maxima located in between the InAs bulk-like diffraction position and GaAs (202) spots. By analyzing the intensity peak positions, we reveal that these scattering intensities are contributed by unstrained $In_xGa_{1-x}As$ alloy. The corresponding volume ratio between the unstrained $In_xGa_{1-x}As$ alloy and strained InAs equals to $12 \pm 2\%$.

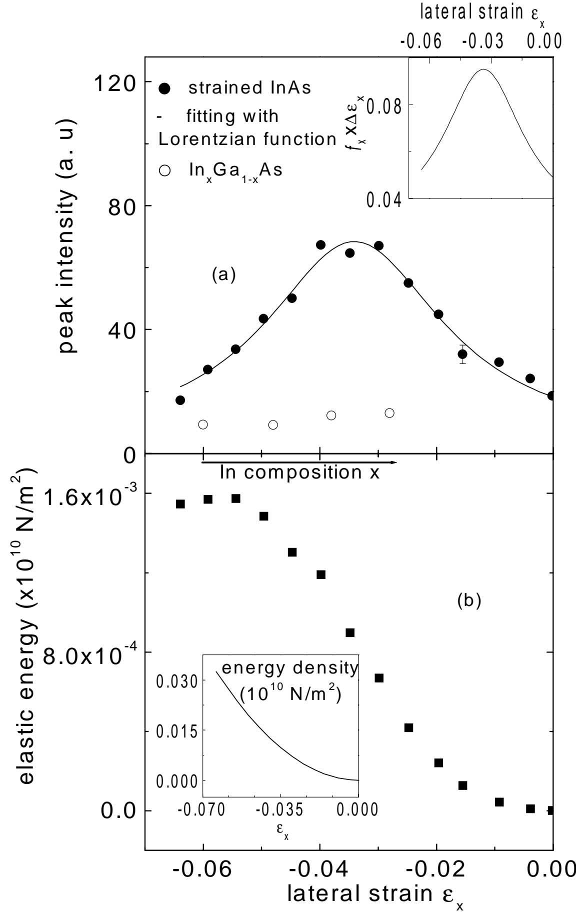

Fig. 50: GIXRD peak intensity maxima (full circles) for different lateral strain components ε_x. The inset is normalized volume fraction $f_x \cdot \Delta\varepsilon_x$ for the different strain components inside InAs QDs as determined from the GIXRD peak intensity maxima. Open circles represent the intensity maxima for $In_xGa_{1-x}As$ with different In composition values of x. ε_x=(a^{InAs}-$a_\circ^{InAs}$)/$a_\circ^{InAs}$, $a_\circ^{InAs}$=6.06 Å, for InAs bulk crystal. $\Delta\varepsilon_x = 0.01$. (b) The elastic energy distribution along with different strain components inside InAs QDs. The inset in (b) is the elastic energy density calculated from elastic theory.

9.4.2 The second type of samples

For the second type of samples, a reciprocal space map was composed showing the scattering intensity with logarithmic scale as a function of q_x and q_z for (202) in Fig. 51a,

and q_y and q_z for $(0\overline{2}2)$ in Fig. 51b, respectively. In the figure, the very bright intensity is from GaAs (202) ((a) $q_x, q_z = 2, 2$) and $(0\overline{2}2)$ ((b) $q_y, q_z = -2, 2$) Bragg diffraction spots with surface rods. In both cases, in addition to the GaAs diffraction peak, we also observe broad intensity peaks which are located at lower q_z values as compared to (202) and $(0\overline{2}2)$ peak positions. The positions of the broad peaks indicate that they are attributed to strained InAs QDs. Especially, by cutting surface rods along q_z direction in both cases, we observe the existence of weak intensity profiles in addition to the rod intensities, which are located with intensity maximum positions of (q_x, q_z)≅2,1.73 r.l.u. for (202) case, and (q_y, q_z)≅-2,1.73 r.l.u. for $(0\overline{2}2)$case. These confirm the existence of a fully strained InAs component in both Bragg diffraction cases. Considering the InAs QD formation is described by Stranski-Krastanov growth mode, we suggest that at QD basis there exists fully strained InAs component matching the GaAs substrate. Moreover, in both cases from intensity plots we find that the broad peak intensity increases with increasing q_z, and has maximum values located at about q_x, q_z=1.865,1.865 r.l.u. for (202), and q_y, q_z=-1.865,1.865 r.l.u. for $(0\overline{2}2)$ Bragg diffractions. These are the diffraction positions for bulk-like InAs in reciprocal space. Above these positions in both cases, the intensity rapidly decreases and merges into the diffusing background. Since the broad intensity peak is located in between InAs bulk-like diffraction peak position and InAs fully strained position, we suggest that the InAs QDs are formed with continuous strain components. However, we note that no evidence is found for the existence of unstrained intermixing $In_xGa_{1-x}As$ structure in these samples.

By analyzing the reciprocal space maps of Fig. 51 in a similar way as described for the first type of samples, we get a series of diffraction intensity peak positions and peak maximum values from InAs QDs in both (a) and (b) cases. We then plot the intensity peak positions in $q_x - q_z$ space for (a) case and $q_y - q_z$ space for (b) case, respectively. These plots are shown in Fig. 52, where open circles denote the (202) Bragg diffraction ((a) case), and full circles stand for the $(0\overline{2}2)$ Bragg diffraction ((b) case). In both cases, we find the data follow a solid line which is the elastic strain position function calculated by elastic theory [Nye57]. This reflects that the InAs QDs are elastically strained with different strain components when they are formed.

The corresponding intensity maximum values for both cases are plotted in Fig. 53 as a function of the strain component. Open and full circles stand for (202) and $(0\overline{2}2)$ cases, respectively. Arrows indicate two extreme values for fully strained and totally relaxed. For both cases, the lowest intensity value is contributed by the fully strained component, while the highest one is associated to almost totally relaxed strain. Comparing the intensity

distributions of the two cases, they are similar but significantly different. In particular, the intensity distribution maxima and their corresponding strain values are different in both cases. For (202) case, the strain value associated to the intensity maximum is located at $\varepsilon_x = -0.15 \pm 0.05$ position, whereas in $(0\overline{2}2)$ case the maximum intensity position is at $\varepsilon_x \to 0$. Moreover, for the latter case, its maximum value is larger than that of the (202) case. As the measured peak intensity is proportional to the square of the number of crystal unit cells, the intensity values reflect the normalized volume fraction to the QD volume for each strain component.

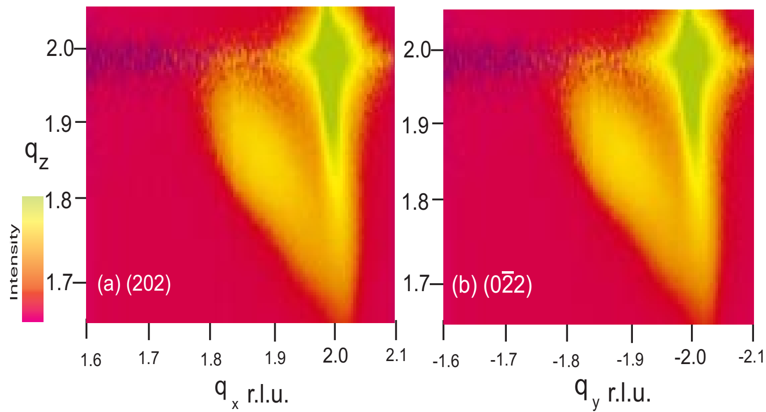

Fig. 51: Reciprocal space map of GIXRD on GaAs (202) (a) and $(0\overline{2}2)$ (b) Bragg diffractions.

In addition, we performed q_y scans for (202) Bragg diffraction, and q_x scans for $(0\overline{2}2)$ at a series of q_z values. From these one can make reciprocal space maps as shown in Fig. 54. Fig. 54a is for the case of (202) Bragg diffraction and Fig. 54b for $(0\overline{2}2)$. In both (a) and (b), $q_x - q_y$ plane is parallel to the sample surface. The very bright narrow spots in Fig. 54 are the intersection of the (202) and $(0\overline{2}2)$ truncation rods. The broad intensity peak near the rod is diffracted from InAs QDs. The central peak positions

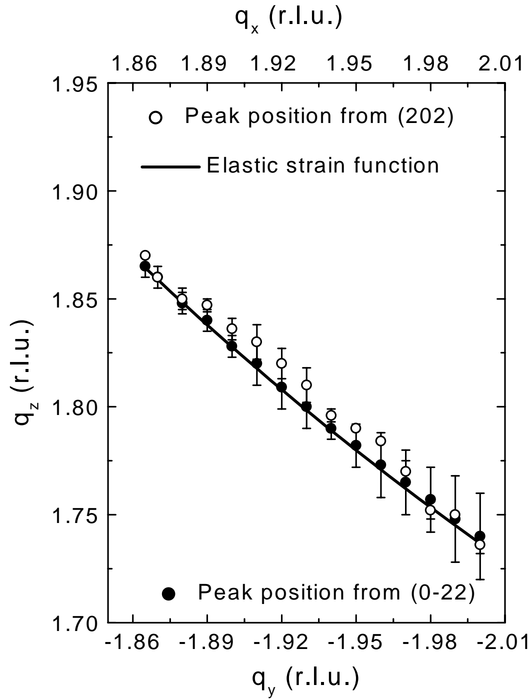

Fig. 52: The position distribution of the (202) and ($0\overline{2}2$) GIXRD intensity maxima for InAs QDs in q_x-q_z (open circles) and q_y-q_z (full circles) space, respectively. The top coordinate is for (202) case and the bottom one is for ($0\overline{2}2$) case. The solid line denotes the diffraction peak position of elastically strained InAs crystal calculated by elastic theory. r.l.u. is the reciprocal lattice unit , i. e. G(100)=$2\pi/a_\circ^{GaAs}$.

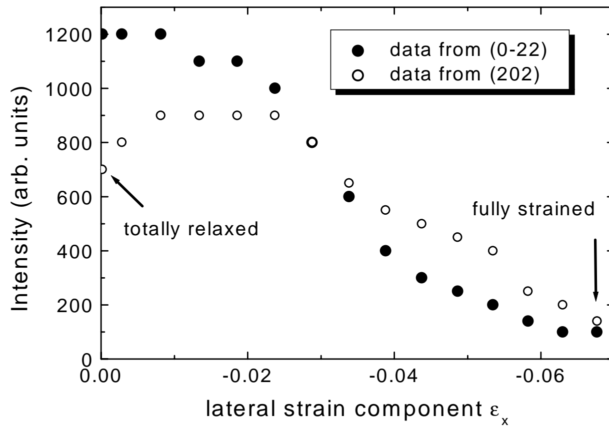

Fig. 53: GIXRD peak intensity maxima for different lateral strain components ε_x. Open and full circles denote the intensity maxima for InAs QDs (202) and ($0\overline{2}2$) cases, respectively. Arrows indicate two extreme values for the fully strained and totally relaxed.

which are determined from q_x and q_z values (for (202) case, q_y=0), or q_y and q_z values (for ($0\overline{2}2$) case, q_x=0), are associated with the corresponding strain components. For

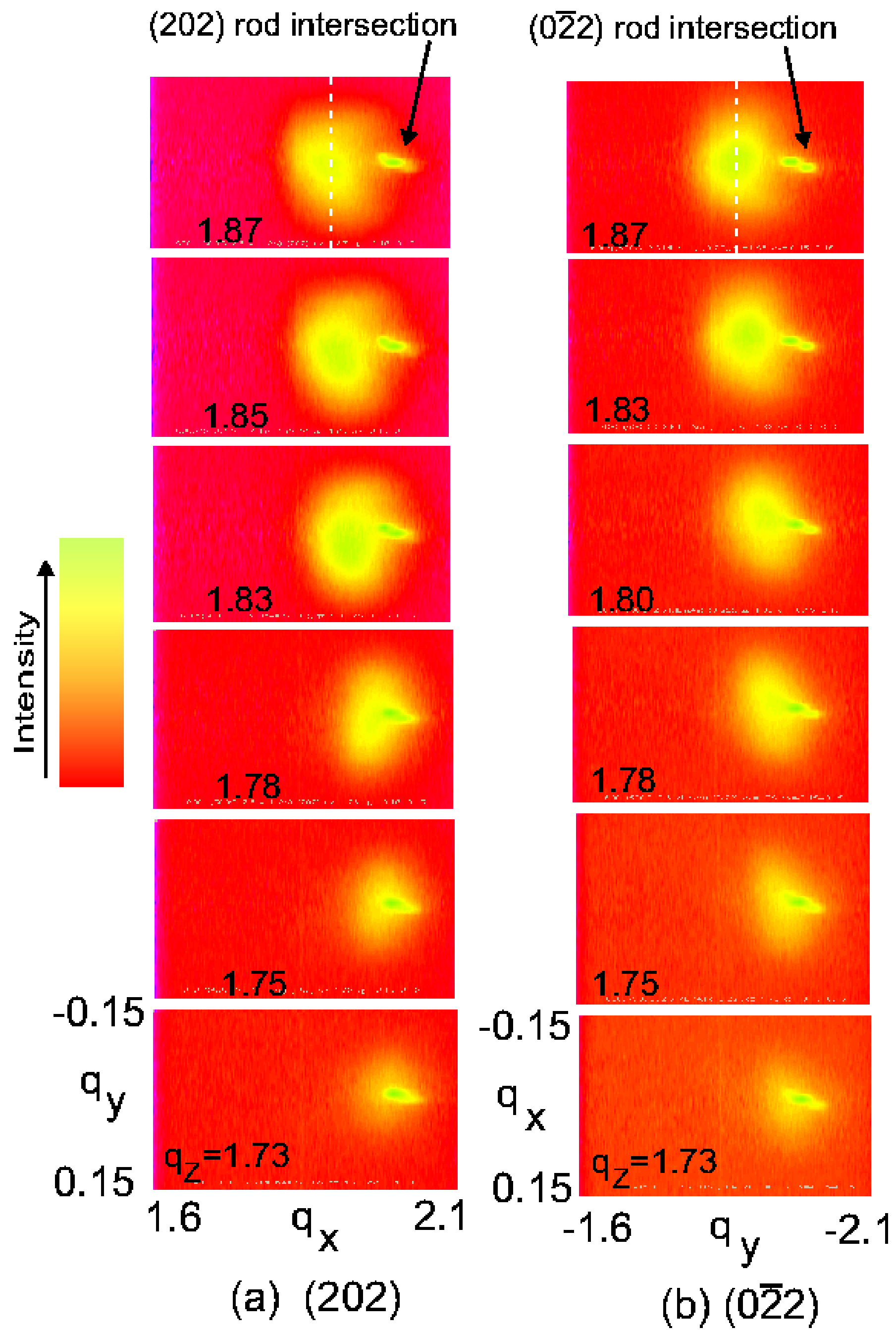

Fig. 54: Reciprocal space $q_x - q_y$ map for different q_z values. (a) is for (202) Bragg diffraction case, and (b) for (0$\bar{2}$2) case.

both (a) and (b), it is clearly seen that at q_z=1.73 r.l.u., the intensity overlaps with the rod, and along with increasing the q_z values, the central peak positions are shift with respect to the rod position. It is the same effect as observed in Fig. 51, but different reciprocal space plane. Again, the presented overlapping at q_z=1.73 r.l.u in Fig. 54 indicates the existence of fully strained InAs.

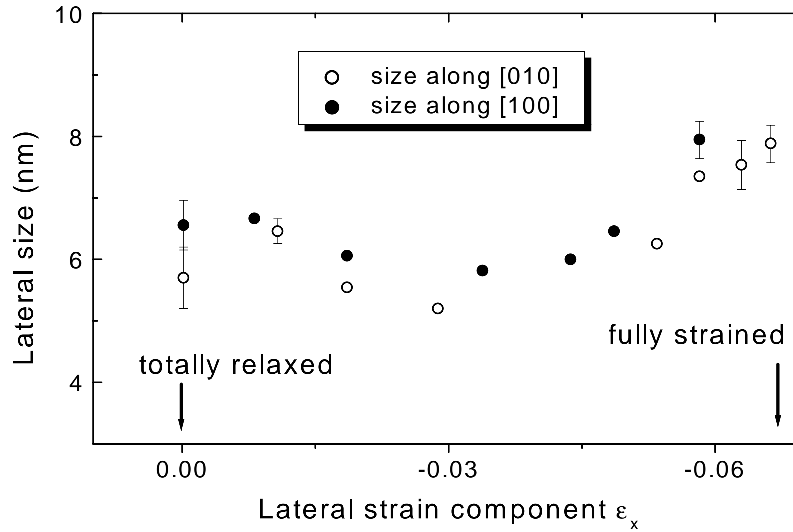

Fig. 55: Lateral size distribution with different strain components inside InAs QDs. Open circles are determined from Fig. 54a of (202) Bragg diffraction, indicating the size along [010] direction. Full circles are determined from Fig. 54b of $(0\bar{2}2)$ diffraction, indicating the size along [100] direction.

In addition, the cutting direction is also indicated at one of the images in each case by white dashed line as an example. The lateral size of InAs QDs at each strain component can be determined by analyzing an intensity profile obtained from the cut through the broad peak of each map and plotted as a function of the corresponding strain value in Fig. 55. Open circles are determined from Fig. 54a of (202) Bragg diffraction, indicating the size along [010] direction. Full circles are determined from Fig. 54b of $(0\bar{2}2)$ diffraction, indicating the size along [100] direction. We find that the distribution of the lateral size

in both cases is similar. The relative large lateral size is attributed to the almost fully strained components, which are suggested to be located at the dot basis regime. The small size is around at the strain component of -0.03. Moreover, the lateral size in [100] direction is slightly larger than that in [010] direction, suggesting that the corresponding area of $(0\overline{2}2)$ lattice plane is larger than that of (202) plane.

9.5 Summary

In conclusion, we present results of GIXRD experiments in a diffraction geometry that allows the determination of strain and composition inside the InAs QDs. The GIXRD data demonstrate that InAs QDs are elastically relaxed with different strain components for all measured samples in the present work. For the InAs QDs with different MBE growth parameters, the strain dependent volume distribution inside QDs is different. We also find intermixing of Ga and In and the formation of $In_xGa_{1-x}As$ structures only for the samples grown with low As-flux. However, the diffraction intensity originating from intermixed materials is quite weak and therefore only a smaller volume fraction of such intermixing structures exists in comparison to strained InAs QD volume. We suggest that the intermixing structure is located in relaxed $In_xGa_{1-x}As$ islands which may be related to the findings of Joyce et al. [Joy98]. Due to a slightly lower growth temperature in our case these islands may be in competition to growth of strained InAs QDs. The almost complete absence of fully strained InAs in the case of first type of samples can be explained by additional intermixing at the dot base, however this is not directly accessible to x-ray diffraction.

From the presently comparable study, we imply that the growth temperature and As-flux might be crucial elements for improving the InAs QD quality. Growth with relatively high As-flux may result not only in the larger dot size with low dot number density, but also in a good dot quality and the suppression of Ga-In intermixing.

Chapter 10

Interface Characterization of Buried InAs Monolayers

Ultra-thin buried InAs layers on GaAs (001) substrate crystals prepared by molecular beam epitaxy are structurally characterized using synchrotron radiation combined by GIXR, CTR and XSW techniques. GIXR and CTR experiments were utilized to determine a comprehensive structural information in terms of the average layer thickness, interface roughness, and the stoichiometry of the layers. XSW experiments determine the In lattice site and vertical distribution . We discuss our results in view of the structural transition of the layer system from 2D to 3D growth mode with In deposition from 1.0 to 2.1 ML.

10.1 Research focus

Much interest is devoted to the understanding of structural formation of ultra-thin InAs layers buried in GaAs, since the information on the atomic structure of the interface is essential to fully understand the electronic properties of such heterostructures [Shi90, Bra92, Mas93, Gia93, Ber94, Woi95]. The issue of the 7% lattice mismatch is one the major obstacles for InAs/GaAs epitaxy. The interface morphology, film strain, and dislocation existence are strongly affected by the discrepancy of this large lattice mismatch. Furthermore, recent research results at semiconductor heterointerfaces of the GaAs/Si system [Dan92, Luc97] were reported that the interface roughness is also depending on the lattice mismatch. The overall lattice parameter represents a fundamental constant

intrinsic to each semiconductor. However, in the case of InAs film on GaAs, 3D islands with dislocation free inside are formed as soon as the deposited InAs coverage thickness exceeds its critical thickness of about 1.8 ML. Such 3D InAs islands were intensively debated worldwide in recent years, as indicated in the Chap. 7, Sec. 7.1 and Chap. 9, Sec. 9.1.

For InAs epitaxial layers with thickness below its critical value, there are usually two contradictory strain models which were used to evaluate the atomic displacements: the elastic model and the conservation of bond length model. In the case of 1 ML InAs strained on GaAs (001), the elastic model leads to a vertical strain of 7% while the constant In-As bond length results in a value of 12%. Brandt *et al* [Bra92] reported that the elastic theory breaks down in the limit of 1 ML of InAs and the constant bond length model should be applied to this ulti-thin layer, by using the high resolution transmission electron microscopy technique (HRTEM). This finding was supported subsequently by an *ab initio* total energy calculation by Shiraishi *et al* [Shi90] and a valence-force field calculation on a surface layer by Massies *et al* [Mas93]. On the contrary, Giannini *et al* [Gia93] found the the In atom positions are consistent with the elastic model by using XSW technique. this result was also testified by extended x-ray absorption fine structure (EXAFS), XSW [Woi95], high resolution x-ray diffraction (HRXRD) [Zhe98] and calculation using the density functional theory in the local density approximation [Ber94].

In addition, segregation effects at III-V semiconductor heterointerface have been the key focus of numerous investigation throughout the past few years [Gui87, Moi89, Moi91, Hou89, Iva90, Bra92, Mur92]. HRTEM [D'A89] is able to image such objects. However, the interpretation of HRTEM images is difficult due to strain induced effects in the image contrast. Moreover, such HRTEM reflects only a local probe of the heterostructure. A detailed structure analysis in terms of the ultra-thin buried InAs layer was recently performed by high resolution X-ray diffraction [Gia93]. However, the interface roughness and the stoichiometry of the buried layer are still not well known. Especially, almost no literature reported concerning of the interface characterization in the case of growth mode transition in InAs/GaAs systems. In the following, we employ GIXR, CTR and XSW techniques to resolve the interface structure of the buried InAs layer with coverage ranging from 1 monolayer (ML) to 2.1 ML.

10.2 Sample growth

A thin InAs layer was sandwiched between a 200 nm thick GaAs buffer layer and a 5 nm GaAs cap. The buffer was deposited at 600^0 C, whereas InAs and cap are deposited at the same temperature of 500^0 C. Growth was interrupted for 1 minute prior to InAs deposition in order to reduced the substrate temperature. The InAs and GaAs flux rates were 0.07 ML/sec and 0.9 ML/sec, respectively. The amount deposited at the substrate temperature 500^0C corresponds to a coverage between 1 and 2.1 ML. The critical thickness for the transition from 2D to Stranski-Krastanov (3D) growth mode was found to occur at around 1.8 ML InAs coverage. We discuss a series of three samples with an InAs coverage of 1.0 ML (sample 1), 1.84 ML (sample 2) and 2.1 ML (sample 3). In addition, we also deposited InAs films at the substrate temperature of 450^0C, with coverage thickness between 1 ML and 1.9 ML. The transition took place at about 1.5-1.6 ML. Structural investigation for the samples grown at 450^0 C have also been performed by GIXR, CTR and XSW. In this chapter, we will list GIXR results for samples grown at 450^0 C together with those grown at 500^0 C. The CTR and XSW results for such samples grown at 450^0 C have been discussed in Ref. [Foe99] and will not be shown in here.

10.3 X-ray experimental

GIXR measurements were performed at beamline ROEMO I. A Ge (111) double crystal monochromator was tuned to a photon energy of 10 keV. The reflectometer is described in detail in the literature [Sta92]. The reflectivity scans was performed at grazing incident angle range of $0^0 - 3^0$. The incoming beam size was 0.01×3 mm^2 and the reflection intensity was counted using the PSD detector mounted in the direction vertical to the sample surface. Due to the precision of the instrument the absolute reflectivity can be determined quite accurately. Normalization and geometrical effects are therefore fixed values and no fitting parameters. This allows easy separation of signal and background contributions as well as diffuse scattering. The reflectivities were analyzed using the dynamical scattering theory [Par54, Nev80, Bah93].

CTR around the GaAs (004) Bragg reflection were measured at the undulator beamline BW1 at 9 keV using two symmetric Si (111) crystals as monochromator as well as two gold coated mirrors for focusing and suppression of higher harmonics. A PSD detector with spatial resolution in the vertical scattering plane was used to determine the diffuse

scattering and background simultaneously with the surface rod scans.

XSW measurements were performed at the BW1 beamline in the (004) Bragg reflection at a photon energy of 8 keV using a nondispersive monochromator consisting of a pair of symmetrically and asymmetrically cut Ge (004) crystals. The rocking curving and In fluorescence were monitored simultaneously by sweeping the incidence angle at the sample through the Bragg condition. For the detail in terms of the experimental procedures, please refer Chap. 4, Sec. 4.3.4.

10.4 Results and discussions

10.4.1 GIXR

The interface structure and roughness of buried InAs monolayers with a coverage ranging from 1 to 2.1 ML is studied by means of GIXR. The GIXR data were analyzed using dynamical scattering theory [Bah93]. The ratio δ/β between δ (dispersion correction) and β (absorption coefficient), and δ_{GaAs} were fixed to the theoretical values ($\delta_{GaAs} = 9.1 \times 10^{-6}$, $\delta_{InAs} = 10.0 \times 10^{-6}$). In order to further reduce the number of free parameters for the simulation, the InAs interlayer thickness was determined from measurements of CTR. Typical GIXR oscillation curves and the sample structural models for the simulation are shown in Fig. 56. For samples with an In deposit below the critical thickness, the GIXR oscillation curve was fitted to a three layer model, i.e., GaAs substrate/InAs/GaAs/oxide as illustrated in Fig. 57a. For thicker films a four layer model was applied as explained in Fig. 57b. In Fig. 56, intensity oscillations at larger incidence angles reflect the existence of a buried InAs layer between the GaAs substrate and cap layer. The amplitude of the oscillation is mainly due to the difference in electron density of the InAs layer and the GaAs cap layer. Its damping is determined by the interface roughness which may be induced by the interdiffusion and/or island formation in the InAs layer. The fitting results clearly confirm that without substantial intermixing of Ga and In, no agreement between data and fit could be achieved. Furthermore, the slope of the GIXR curve slightly above total external reflection is very sensitive to the oxide layer on top of the GaAs cap layer. The GIXR data were analyzed in terms of the formulas using dynamical scattering theory [Bah93]. For sample 1, the GIXR oscillation curve was fitted to a three layer model on GaAs substrate. For the thicker films, i. e. sample 2 and 3, a four layer model was applied to account for the dot formation: InAs wetting layer/InAs islands

mixed layer/GaAs /oxide, on GaAs substrate. The structural parameters derived by the simulation are shown in Table 10.1. For sample 1, the dispersion correction for the InAs interlayer is $(9.5 \pm 0.1)\times 10^{-6}$ which indicates a Ga content of $60 - 70\%$ in this layer. The interface roughness is found to be in the range of 4.9-6.5 Å. For sample 2 (slightly exceeding the critical thickness), a more pronounced oscillation of the GIXR intensity is found due to the larger In content of the film. In order to account for the presence of In islands the model is modified to be 4 layer model, as shown in Fig. 57b. In this model, an additional layer of GaAs mixed with InAs reflects the InAs islands embedded in the GaAs layer. The 4 layer model yields an In content of about 50% in the wetting layer. Moreover, the interface roughness is derived to be 3.2-5.5 Å. The average height of the InAs islands as obtained from the thickness of the InAs islanding layer is determined to be 21 ± 1 Å. The roughness of this islanding layer is only about 1.2 ± 0.5 Å. For sample

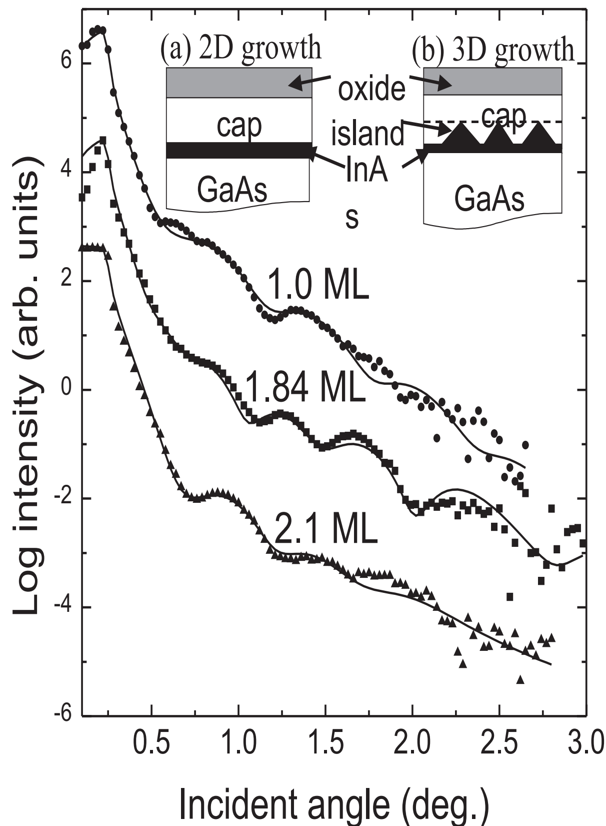

Fig. 56: GIXR intensity vs. incident angle for InAs/GaAs samples with different InAs coverage grown at 500^0C. The solid lines represent the simulations to the data by a 3 layer (a) and 4 layer (b) models. for clarity, the upper curves are moved by two orders of magnitude relative to the lower one, respectively. The inset shows a sketch of the sample models used to analyze the data.

3, the 4 layer model calculation yields a significantly larger In content in the wetting layer of about 70%. Here the interface roughnesses are between 5.4 and 6.8 Å. The layer containing InAs islands has a thickness of about 41 Å. The presence of the such high islands causes a strong damping of the intensity oscillations in GIXR. For all samples, the oxide layer thickness is determined to be 22±1 Å.

The same performance and analysis of GIXR have been done for samples grown at 450^0 C. The corresponding GIXR intensity curves are displayed in Fig. 58 for InAs coverage of 1 ML, 1.7 ML, and 1.9 ML, respectively. The fitting results for the interfacial structure is shown in Table 10.2. We found that the dispersion correction is slightly larger than those grown at 500^0 C, leading to higher In concentration inside the interlayer. Moreover, the interface roughness is also smaller in comparison to those grown at 500^0 C. The InAs island layer is derived to be 27 Å, which is smaller than that grown at 500^0 C. Above structural features suggest that the In interdiffusion and segregation at the interface take place during cap layer growth, resulting in interface roughness and InGaAs structure of the δ layer. However, as compared to the structural parameters of samples grown at 500^0 C, we conclude that the interface quality is better for sample grown at 450^0 C than that grown at 500^0 C.

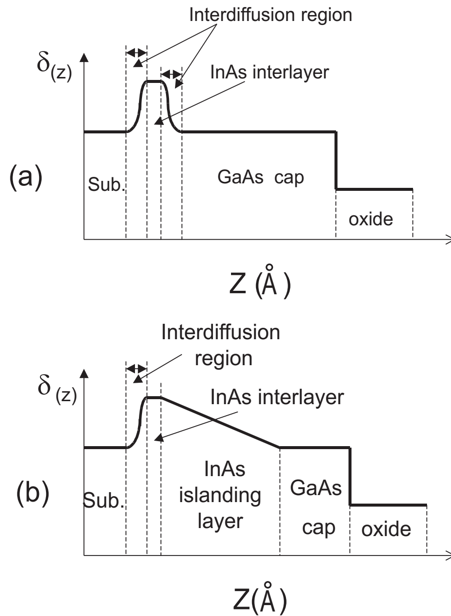

Fig. 57: The profile of the dispersion correction δ_z perpendicular to the sample surface used to model the reflectivity data derived from 2D growth samples (a) and 3D growth samples (b). The perpendicular distance between dash lines are the layer thickness.

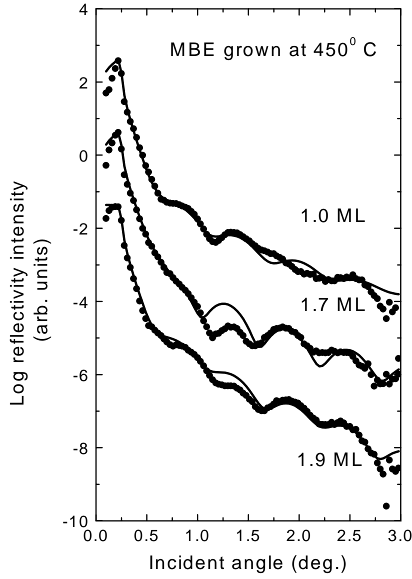

Fig. 58: GIXR intensity vs. incident angle for InAs/GaAs samples with different InAs coverage grown at 450^0C. The solid lines represent the simulations to the data by a 3 layer (Fig. 57a) and 4 layer (Fig. 57b) models. For clarity, the upper curves are moved by two orders of magnitude relative to the lower one, respectively.

Table 10.1: Structure parameters of InAs δ layer derived by GIXR, CTR, and XSW.

sample grown at 500^0C	InAs coverage by flux (ML)	1.0	1.84	2.1
GIXR	interface roughness (Å)	4.9–6.5	3.2–5.5	5.4–6.8
	cap layer thickness (Å)	55.0±1.0	65±2.0	57±1.8
	oxide layer thickness (Å)	22±1		
	$^*\delta_{disp.}$ in wetting layer $\times 10^{-6}$	9.5	9.6	9.8
	island height (Å)	–	≈21	≈41
CTR	wetting layer thickness N_δ (ML)	2	2	1
	lattice spacing a_δ (Å)	1.47	1.50	1.41
	In concentration x_δ%	31	46	68
	rms interface roughness (Å)	1.0±0.3		
	segregation length $1/e$ (Å)	5.0±1.0		
XSW	coherent position Φ_c	1.11±0.01	1.25±0.01	1.22±0.02
	coherent fraction f_c	0.86±0.05	0.76±0.04	0.41±0.06

*the dispersion corrections for pure GaAs and InAs crystals are 9.1×10^{-6} and 10.0×10^{-6}, respectively.

Table 10.2: GIXR simulation data for InAs/GaAs δ layer samples grown at 450^{0}C with different InAs coverage.

structure parameters	1 ML	1.7 ML	1.9 ML
substrate roughness (Å)	6.0±0.26	5.8±0.4	3.0±0.1
wetting layer $\delta_{disp.} \times 10^{-6}$	9.7	9.8	9.8
wetting layer roughness (Å)	2.5±0.7	2.3±0.4	3.0±0.3
wetting layer thickness (Å)	2.9	5.6	6.04
dot layer $\delta_{disp.} \times 10^{-6}$			9.4±0.1
dot layer roughness (Å)			1.0±0.2
dot height (Å)			27±1
GaAs cap $\delta_{disp.} \times 10^{-6}$	9.07	9.07	9.07
GaAs cap roughness (Å)	1.5±0.2	0.8±0.3	2.5±0.5
GaAs cap thickness (Å)	53±1	58±3	32±1.5
oxide layer $\delta_{disp.} \times 10^{-6}$	7.3±0.1	7.6±0.1	4.2±0.1
oxide layer roughness (Å)	18.5±1.0	17.0±1.0	17.0±1.5
oxide layer thickness (Å)	16.0±1.5	16.0±2.0	22.0±5.0

10.4.2 CTR

Fig. 59 shows the CTR oscillation curves measured around the GaAs (004) Bragg peak for all samples. The thickness of the GaAs cap layer is obtained from the period of the oscillation. The amplitude of the oscillation is determined by the jump of the average lattice constant at the InAs/GaAs interface and its damping is related to the roughness of the interfaces. The distance between the maximum of the oscillation and the (004) Bragg peak is mainly due to the thickness of the InAs layer. Straight lines in Fig. 59 are the fits calculated from kinematical diffraction theory [Bah96]. We also interpreted this theory by Eq. 3.30 in Chap. 3, where top layer is GaAs, δ layer is InAs and substrate is GaAs. For CTR the structural model is, GaAs substrate/InAs/GaAs cap. In the case of X-ray diffraction, the amorphous oxide basically is not visible. The main parameters obtained from the fits to the CTR data are also shown in Table 10.1. For sample 1, the best fitting results show that the thickness of the InAs layer N_δ is 2 ML and the In concentration in each monolayer is only about 31%. The rest of the deposited In has segregated to the GaAs cap layer. The lattice spacing in InAs layer is determined to be

1.47 Å, which is very close to that for the composition of In in $In_{0.31}Ga_{0.69}As$, i. e. 1.48 Å, as calculated from the classical theory of elasticity. This result indicates that there is an InGaAs alloy in the layer. Moreover, the analysis yields the rms roughness in the InAs layer and the $1/e$ segregation length of In into the cap layer, which are determined to be 1.0 ± 0.3 Åand 5.0 ± 1.0 Åfor all samples, respectively. These values are in good agreement with the results of our GIXR data, if we assume that the interface roughness is dominantly determined by the In segregation into the cap.

For sample 2, the wetting layer thickness N_δ is found to be 2 ML, too. The In concentration is higher than that of the sample 1. Again, In segregation to the surface is found to be strong during growth of the GaAs cap layer. The lattice spacing in the wetting layer amounts to 1.50 Å, which is in good agreement with the calculation for an $In_{0.46}Ga_{0.54}As$ alloy, i. e. 1.49 Å. For sample 3, the best fit for CTR data is only realized by choosing N_δ=1.0 ML. However, the model applied is not very suitable to characterize a layer with islands. The fitting results show that the lattice spacing in the wetting layer is 1.41 Å, which does not correspond to that calculated from an $In_{0.68}Ga_{0.32}As$ alloy. This we attribute to the formation of InAs islands.

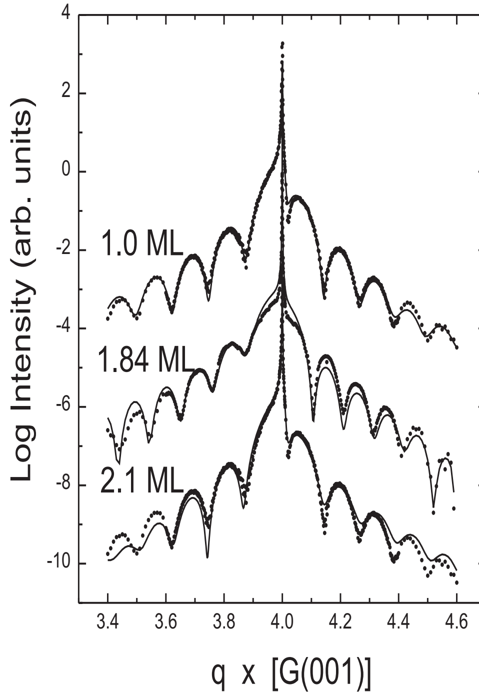

Fig. 59: CTR intensity curves around (004) Bragg peak for InAs buried δ layers grown by MBE at substrate temperature of 500^0C: 1.0 ML (upper), 1.84 ML (center), and 2.1 ML (lower). For clarity, the lower curves are displaced by three orders of magnitude relative to the upper curve, respectively. The solid lines in the figure are the fit simulated by Eq. 3.30. The reciprocal lattice unit in q-axis is $G_{001}(GaAs) = 2\pi/a_0^{GaAs}$.

10.4.3 XSW

Measurements of XSW can be analyzed to identify the lattice position and fraction of In atoms located on the lattice sites with high accuracy. An XSW field is yielded by the interference of the incoming and Bragg-reflected waves. The periodicity of XSW field is the same as that used for Bragg reflection. For a proper description of the interference effects and the exact shape of the Bragg reflection, the dynamical theory of x-ray scattering is employed [Pin78]. Details of the XSW experiments and analysis can be referred in the literature, e. g. [Zeg93]. The main parts of this theory and experimental performance were extracted in Chap. 3, Sec. 3.7 and Chap. 4, Subsec. 4.3.4. In our samples, since the GaAs capping layer is thin in comparison to the extinction depth of the x-ray fluorescence, extinction effects can be neglected in the analysis. We can use Eq. 3.43 to simulate the measured data. In Eq. 3.43 $R(\theta)$ is the sample reflectivity describing the shape of the Bragg peak. $\nu(\theta)$ denotes the phase shift of the XSW field changing from π to 0 when scanning through the Bragg reflection. The coherent position Φ_c and coherent fraction f_c are the phase and amplitude of the H, K, L-Fourier component of the atomic distribution function in the crystal with H, K, L denoting the Bragg reflection employed for the measurements. A value of $f_c = 1$ indicates that all atoms occupy an identical lattice position, whereas $f_c = 0$ represents random distribution around the exact lattice site. Coherent position Φ_c denotes the relative position of In atoms with respect to the GaAs diffraction planes.

Fig. 60 shows reflectivity and normalized fluorescence yield data for InAs δ layers grown on GaAs (001) at 500^0C. Also displayed are the fits and the obtained values of Φ_c and f_c. The fits to the data according to an analysis method described in Ref. [Zeg93] yield the coherent position Φ_c and coherent fraction f_c as summarized in Table 10.1. Φ_c and f_c are the phase and amplitude of the (004) Fourier component of the atomic distribution of In. Hence, they reflect the crystallinity of the In. For sample 1 with 1.0 ML InAs coverage, the coherent fraction is 0.86, which is close to the InAs bulk value of perfect crystallinity of the In. This indicates a high crystallinity of the layer. Moreover, the value of coherent position in this sample is agreement with a pseudomorphically strained InGaAs δ layer assuming that strain relaxation of InAs δ layer can only occur in growth direction. The values summarized in Table 10.1 show an increased coherent position and a reduced coherent fraction with increasing InAs deposit. This may be interpreted by an enhanced multilayer occupation with increasing InAs thickness. The smaller coherent fraction for thicker layers (for sample 2) can be attributed to an increased number of the

relative lattice positions devoting to Φ_c and f_c. In particular, the significant reduction of the coherent fraction with increasing In deposit (for sample 3) reflects the onset of 3D islanding. For multiple layer occupancy of In, the lattice position may not be derived directly from the corresponding coherent position, instead, it depends critically on the model suggested.

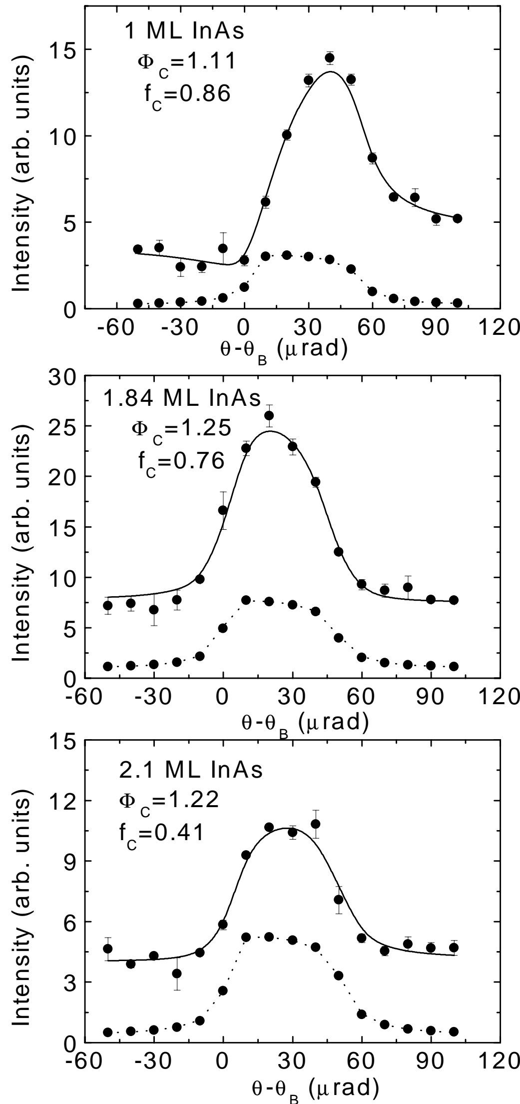

Fig. 60: XSW intensities for the sample 1 (1 ML InAs), sample 2 (1.84 ML InAs), sample 3 (2.1 ML InAs). The full circles denote the experimental data. The solid and dotted lines are fits to In L fluorescence yield and GaAs (004) Bragg reflection curve, respectively. $\theta - \theta_B$ is the rocking angle of the sample with respective to the exact Bragg peak position θ_B. Φ_c and f_c are the coherent position and coherent fraction of In atoms, respectively.

10.5 Summary

The interface structure of ultra-thin buried InAs layers has been investigated. The structural parameters obtained by different methods are in reasonable agreement. For In and Ga intermixing above the InAs layer, we find that the effect of In segregation into the cap is very important at these temperatures. The In concentration in the InAs layer increases with increasing In coverage, as determined by GIXR and CTR. In XSW measurements we find a high crystallinity of In at low coverage and a strongly reduced coherent fraction at high In coverage reflecting the onset of InAs island formation.

Chapter 11

Conclusion and Prospect

In conclusion, we have studied MBE growth and structure investigation of self-assembled semiconductor InAs QDs on GaAs substrate.

In situ RHEED diffraction pattern and intensity oscillation enable us to control InAs deposit coverage precisely. RHEED accurately monitors ultra-thin InAs 2D film growth as well as the transition to 3D InAs QDs with Stranski-Krastanov growth mode. In the present work, we observe the transition from 2D thin film growth to 3D QD growth occurs at around 1.5 ML for growth temperature of 450^0C and 1.8 ML for temperature of 500^0C. AFM allows to investigate the topology of InAs QD. In the case of 500^0C substrate temperature, the saturation of InAs QD lateral distribution is found to occur at InAs coverage thickness of 2.3 ML, below which InAs QD topologies are highly homogeneous with very narrow size distribution. From comparable AFM investigations on samples with stepped surface of 2^0 off towards [100], we find that the significantly anisotropic QD lateral distribution occurs in [100] direction, manifesting the square-like lattice distribution of QDs. This phenomenon implies that the better distribution of InAs QDs may depend on the GaAs substrate features, by patterning which one may expect to grow InAs QDs with square-like lattice distribution. This will lead to prospective applications on opto-electronic semiconductor devices.

AFM technique employed in the present work is limited to investigation of the InAs QD topology in most cases. A further study on InAs QD crystal structure is obstructed. Moreover, for capped InAs QD samples, no information in terms of buried InAs QDs can be achieved by AFM. In order to get thorough structure characterizations of InAs QDs, x-ray diffraction techniques supported by synchrotron radiation have been employed in

the present work.

We present GISAXS experiments that for the first time reflect lateral ordering in an uncapped single layer of self-assembled InAs QDs on GaAs(001). Furthermore, in our experiments facet CTR peaks are observed from which the dot facet shape can be inferred. Enhanced lateral ordering of the InAs QD distribution is found along $[1\bar{1}0]$, [110] and [100] directions. The azimuthal dependence of the GISAXS intensity points to an anisotropic dot distribution with a large dot separation and a small correlation length in <100> like directions in comparison to ¡110¿ like directions. Moreover, the azimuthal dot distribution function is sharper in [110] than in other directions. This may indicate the presence of an anisotropic strain field around QDs. The morphology of InAs QD shape is determined by GISAXS as a truncated octagonal-based pyramid.

In addition, GISAXS technique has also been employed to investigate the lateral distribution of buried InAs QDs, from which we reveal that the azimuthal scattering intensity distribution induced by QDs is highly concentrated into around [110] crystal direction. However, in other azimuths the scattering intensity is rather low and homogeneous. The mean dot-dot distances with a large standard deviation in most sample azimuths are the same, except for the case in [110] direction, where the smaller mean dot-dot distance with a narrow standard deviation is found. This reflects that the dot distribution in [110] direction is better ordered than in other azimuths. Moreover, no evidence is observed for the existence of dot facets in comparison to that of the uncapped dots [Zha00], which may suggest that the dot facets are highly disturbed by the GaAs cap layer.

In particular, very important experiments presented in this work are GIXRD experiments in a diffraction geometry that allows the determination of strain and possible composition inside the InAs QDs. Among samples with different growth conditions, a common point is that the GIXRD data demonstrate InAs QDs to be elastically relaxed with different continuous strain components. The fact that the smallest diffraction intensity occurs at nearly fully strained components and the strain dependent lateral size inside dots are found no significant difference, indicates no "iso-strain model" [Keg99] is associated in the present work. We also find intermixing of Ga and In and the formation of $\mathrm{In}_x\mathrm{Ga}_{1-x}\mathrm{As}$ in some of samples grown with relatively low As-flux. However, the diffraction intensity originating from intermixed materials is weak. We suggest that this material is located in relaxed $\mathrm{In}_x\mathrm{Ga}_{1-x}\mathrm{As}$ islands. Due to a slightly lower growth temperature in our case these islands may be in competition to growth of strained InAs QDs. The almost complete absence of fully strained InAs in some samples can be explained by additional intermixing

at the dot base, however this is not directly accessible to x-ray diffraction. Comparing the investigation results among the samples, we imply that the growth temperature and As-flux might be crucial elements for improving InAs QD quality. Growth with relative high As-flux might result not only in larger dots with low dot number density, but also in good dot quality with suppression of Ga-In intermixing.

The interface structure of ultra-thin buried InAs layers with different InAs deposit coverage from 1.0 ML to 2.1 ML has also been investigated. The structural parameters obtained by the combination of GIXR, CTR and XSW experimental methods are in reasonable agreement. For In and Ga intermixing above the InAs layer, we find that the effect of In segregation into the cap is very important at growth temperature of 500^0C. The In concentration in the InAs layer increases with increasing In coverage, as determined by GIXR and CTR. In XSW measurements we find a high crystallinity of In at low coverage and a strongly reduced coherent fraction of In at high In coverage reflecting the onset of InAs island formation.

From my preliminary studies on structure characterization of self-assembled InAs QDs, we have revealed the main structural parameters exhibited by InAs QDs when they are formed. This allows to approach the nature of InAs QDs, from which one can get a feedback of how to control MBE growth in order to achieve a desired InAs QD formation. As we know, the high density of states associated with the dots can be very profitable for semiconductor laser applications. Meanwhile, we are also aware of that the dot lateral distribution is a dominant element in such systems, which may strongly influence their optoelectronic property. The most optimized point is to make the dots with high ordering in their lateral distribution. For the electronic device application reason, the quantum dots at least must be capped by a cap layer. During the cap layer growth, the atomic segregation and interdiffusion at the interface may take place, which obstruct us to get highly desired optoelectronic properties. As a consequence, there are two common questions that need to be achieved in order to give rise to the optimized optoelectronic properties.

1) how to improve the spatial distribution of self-assembled quantum dots during growth in order to obtain a high ordering?
2) how to reduce the atomic interdiffusion of the hetero-epitaxy layer at the interface?

Regarding to the above two points, investigation on structural properties like geometry, lateral correlation, strain behavior, and composition of the InAs dots should be kept on studying.

Based on the previous studies, I suggest to do as following,
1) **SAMPLE GROWTH**: InAs dot samples are grown in UHV MBE monitored by *in situ* RHEED, which can control the growth condition accurately. The substrate utilized will be GaAs (001) wafer. Furthermore, misoriented wafers with different degrees of the inclination are highly expected to study the influence of surface steps to the dot ordering. Also, Patterning GaAs substrates in etching chamber with different procedures is strongly desired, with which one can get opportunities to study the subsequent InAs QD growth.
2) **STRUCTURE INVESTIGATION**: The dot morphology can be investigated by *in situ* scanning tunneling microscopy (STM). The dot spatial distribution can be characterized by Fourier transportation of AFM image. In order to get more detailed structural information, the combination of high resolution transmission electron microscopy (TEM) and grazing incidence x-ray techniques is required. TEM can provide us a direct view of the interface structure from which we can analyze the strain behavior and the possible atomic interdiffusion at the interface by the induced image contrast. The most important crystal structure is given by grazing incidence x-ray techniques, since a larger illuminated area of x-ray beam on the sample can be achieved comparing to other techniques. This will result in a higher statistics for the structure investigation in comparison to others. Here, GISAXS to study the dot lateral distribution quantitatively is encouraged. With GISAXS, one can also easily determine the dot facet family, that can be taken for electron structure calculation. GIXRD is a power tool to study the stain status inside the dots, which may provide us the strain distribution in different crystal directions. Moreover, by GIXRD experiments, one may get an unique opportunity to determine experimentally the elastic strain energy distribution inside InAs QDs. Combined with STM, AFM, TEM, and x-ray techniques, one can quantitatively make clear how the strain affects dot lateral distribution. All above techniques will be complementary and important. An essential suggestion here is that for uncapped InAs QDs, above studies had better to be performed in vacuum system. In this way, one can avoid the complicated oxide effect on QDs leading to get thorough structure information of QDs. In fact in devices of technological interest the self-assembled QDs in general will be capped by GaAs layer. In this case, TEM and GIXRD techniques can also gain the very important information on the interdiffusion at the interface quantitatively. Moreover, the study on comparison of capped and uncapped samples will help us to further understand the interaction between Ga and In atoms conveniently.
3) **OPTOELECTRONIC PROPERTIES**: The study of the optoelectronic properties

of the dots will be emphasized on photoluminescence as well as Far Infrared absorption and transmission spectroscopy. Furthermore, the electronic ground states in the dots will be studied with capacitance spectroscopy.

In summary, the strain behavior as a driving force for the dot formation, and the lateral correlation of dots in the capped and uncapped dot layers can be derived by above techniques. In addition, a systematical study by varying both the substrate temperature and the amount of InAs deposited as well as As-flux is expected. The results of the structural investigation will be backed up by studies of the optoelectronic properties. Subsequently, one can improve both the molecular beam expitay growth condition and the fabrication technology of electronic device in order to get the expected optoelectronic properties.

Bibliography

[AN87] J. Als-Nielsen. Structure and Dynamics of Surfaces ii. In: W. Schomers and P. Blanckenhagen, editors, *Topics in Current Physics*, volume 43, S. 181, Berlin, Heidelberg, New York, 1987. Springer–Verlag.

[Bah93] D. Bahr, W. Press, R. Jebasinski, and S. Mantl. Phys. Rev. B **47**, 4385 (1993).

[Bah96] D. Bahr, J. Falta, G. Materlik, B. H. Müller, and M. Horn von Hoegen. Physica B **221**, 96 (1996).

[Bal83] C. A. B. Ball and J. H. van der Merwe. The Growth of Dislocation–Free Layers. In: F. R. N. Nabarro, editor, *Dislocations in Solids*, volume 6, S. Chap. 27, Amsterdam, 1983. North–Holland.

[Bas78] J. H. Basson and C. A. B. Ball. Phys. Stat. Sol. A **46**, 707 (1978).

[Bat64] B. W. Batterman and H. Cole. Rev. Mod. Phys. **36**, 681 (1964).

[Ber94] J. E. Bernard and A. Zunger. Appl. Phys. Lett. **65**, 165 (1994).

[Ber97] M. Berti, A. V. Drigo, G. Rossetto, and G. Torzo. J. Vac. Sci. Technol. B **15**, 1794 (1997).

[BH94] V. Bressler-Hill, A. Lorke, S. Varma, P. M. Petroff, K. Pond, and W. H. Weinberg. Phys. Rev. B **50**, 8479 (1994).

[BH95] V. Bressler-Hill, S. Varma, A. Lorke, B. Z. Nosho, P. M. Petroff, and W. H. Weinberg. Phys. Rev. Lett. **74**, 3209 (1995).

[Bim95] D. Bimberg, M. Grundmann, N. N. Ledentsov, S. S. Ruvimov, R. Werner, U. Richter, J. Heydenreich, V. M. Ustinov, P. S. Kop'ev, and Zh. I. Alferov. Thin Solid Films **267**, 32 (1995).

[bim98] D. bimberg, M. Grundmann, and N. N. Ledentsov. *Quantum Dot Heterostructures.* John Wiley & Sons, UK, 1998.

[Bra92] O. Brandt, K. Ploog, R. Bierwolf, and M. Hohenstein. Phys. Rev. Lett. **68**, 1339 (1992).

[Bue86] J. Buechler, E. Kasper, P. Russer, and K. M. Strohm. IEEE Trans. **MTT–34**, 1516 (1986).

[Cha85] L. L. Chang and K. Ploog. *Molecular Beam Epitaxy and Heterostructures.* Martimus Nijhoff Publishers, 1 edition, 1985.

[Che94] P. Chen, Q. Xie, A. Madhukar, L. Chen, and A. Konkar. J. Vac. Sci. Technol. B **12**, 2568 (1994).

[Cho81] A. Y. Cho and K. Y. Cheng. Appl. Phys. Lett. **38**, 360 (1981).

[Chr94] S. Christiansen, M. Albrecht, H. P. Strunk, and H. J. Maier. Appl. Phys. Lett. **64**, 3617 (1994).

[Chu99] L. Chu, M. Arzberger, G. Böhm, and G. Abstreiter. J. Appl. Phys. **85**, 2355 (1999).

[Cop89] M. Copel, M. C. Reiter, E. Kaxiras, and R. M. Tromp. Phys. Rev. Lett. **63**, 632 (1989).

[D'A89] C. D'Anterroches, J. M. Gerard, and J. Y. Marzin. In: D. Cherns, editor, *Evaluation of Advanced Semiconductor Materials by Electron Microscopy*, volume 203 of NATO Advanced Study Institute aus *B: Physics*, S. p. 47, New York, 1989. Plenum.

[Dae87] H. Daembkes. In: *In Proc. 2nd Int'l Symp. on Si–MBE*, Honolulu, 1987.

[Dan92] R. G. Dandrea and C. B. Duke. Phys. Rev. B **45**, 14065 (1992).

[Dar97] A. A. Darhuber, V. Holy, J. Stangl, G. Bauer, A. Krost, F. Heinrichsdorff, M. Grundmann, D. Bimberg, V. M. Ustinov, P. S. Kop'ev, A. O. Kosogov, and P. Werner. Appl. Phys. Lett. **70**, 955 (1997).

[Dre94] H. Drexler, D. Leonard, W. Hansen, J. P. Kotthaus, and P. M. Petroff. Phys. Rev. Lett. **73**, 2252 (1994).

[Fal98] J. Falta, D. Bahr, G. Materlik, B. H. Müller, and M. Horn von Hoegen. Surf. Rev. Lett. **5**, 145 (1998).

[Far95] R. F. C. Farrow. *MOLECULAR BEAM EPITAXY–Applications to key Materials*. Noyes Publications, Park Ridge, New Jersey,U.S.A., 1 edition, 1995.

[Fin34] A. I. Finch and A. G. Quarrell. Proc. Phys. Soc. **48**, 148 (1934).

[Foe99] A. Foede. *Strukturbestimmung von InAs-Deltaschichten in GaAs(100)*. Master thesis in University of Hamburg, 1999.

[Fra49] F. C. Frank and J. H. van der Merwe. Proc. R. Soc. **198**, 216 (1949).

[Fri96] M. Fricke, A. Lorke, J. P. Kotthaus, G. Medeiros-Ribeiro, and P. M. Petroff. Europhys. Lett. **36**, 197 (1996).

[Gia93] C. Giannini, L. Tapfer, S. Lagomarsino, J. C. Boulliard, A. Taccoen, B. Capelle, M. Ilg, O. Brandt, and K. H. Ploog. Phys. Rev. B **48**, 11496 (1993).

[Gru95a] M. Grundmann, N. N. Ledentsov, R. Heitz, L. Eckey, J. Christen, J. Böhrer, D. Bimberg, S. S. Ruvimov, P. Werner, U. Richter, J. Heydenreich, V. M. Ustinov, A. Yu. Egorov, A. E. Zhukov, P. S. Kop'ev, and Z. I. Alferov. Phys. Stat. Sol. B **188**, 249 (1995).

[Gru95b] M. Grundmann, O. Stier, and D. Bimberg. Phys. Rev. B **52**, 11969 (1995).

[Gru96] M. Grundmann, N. N. Ledentsov, O. Stier, D. Bimberg, V. M. Ustinov, P. S. Kop'ev, and Zh. I. Alferov. Appl. Phys. Lett. **68**, 979 (1996).

[Gui87] C. Guille, F. Houzay, J. M. Noison, and F. Barthe. In: A. Christou and H. S. Rupprecht, editors, *Proceedings of the 14th International Symposium on GaAs and Related Compounds*, volume No. 91 aus *IOP Conf. Proc.*, S. 327, London, 1987. Institute of Physics.

[Hei93] D. Heitmann and J. P. Kotthaus. Physics Today **46**, 56 (1993).

[Hei98] F. Heinrichsdorff, M. Grundmann, O. Stier, A. Krost, and D. Bimberg. Journal of Crystal Growth **195**, 540 (1998).

[Her82] M. A. Herman. Vacuum **32**, 555 (1982).

[Her86] M. A. Herrman. *Semiconductor Superlattices*. Akademie–Verlag, Berlin, 1986.

[Her89] M. A. Herrman and H. Sitter. *Molecular Beam Epitaxy*. Springer Verlag, Berlin, springer series in materials science vol. 7 edition, 1989.

[Hey00] Ch. Heyn, D. Endler, K. Zhang, and W. Hansen. Journal of Crystal Growth **210**, 421 (2000).

[Hou89] F. Houzay, J. M. Moison, C. Guille, F. Barthe, and M. Van Rompay. Journal of Crystal Growth **95**, 35 (1989).

[Ish99] T. Ishigure, T. Haga, S. Muto, Y. Nakata, and N. Yokoyama. Jpn. J. Appl. Phys. **38**, 504 (1999).

[Ish00] T. Ishikawa, T. Nishimura, S. Kohmoto, and K. Asakawa. Appl. Phys. Lett. **76**, 167 (2000).

[Iva90] S. V. Ivanov, P. S. Kop'ev, and N. N. Ledentsov. Journal of Crystal Growth **104**, 345 (1990).

[Joy97] B. A. Joyce, J. L. Sudijono, J. L. Belk, H. Yamaguchi, X. M. Zhang, H. T. Dobbs, A. Zangwill, D. D. Vvedensky, and T. S. Jones. Jpn. J. Appl. Phys. **36**, 4111 (1997).

[Joy98] P. B. Joyce, T. J. Krzyzewski, G. R. Bell, B. A. Joyce, and T. S. Jones. Phys. Rev. B **58**, R15981 (1998).

[Kah83] A. Kahn. Surf. Sci. Rep. **3**, 193 (1983).

[Keg99] I. Kegel, T. H. Metzger, P. Fratzl, J. Peisl, A. Lorke, J. M. Garcia, and P. M. Petroff. Europhys. Lett. **45**, 222 (1999).

[Kob96] N. P. Kobayashi, T. R. Ramachandran, P. Chen, and A. Madhukar. Appl. Phys. Lett. **68**, 3299 (1996).

[Kra87] G. D. Kramer, R. K. Tsui, J. A. Curless, and M. S. Peffley. Properties of Algaas Grown by MBE on Lenticular Substrates. In: *GaAs and Related Compounds 1986*, Inst. Phys. Conf. Ser. 83, S. 117, Bristol, 1987. Inst. of Phys.

[kX99] Qi kun Xue, Kukio Hasegawa, Hisashi Kiyama, and Toshio Sakurai. Jpn. J. Appl. Phys. **38**, 500 (1999).

[Lag92] S. Lagomarsino, F. Scarinci, P. Castrucci, C. Giannini, E. Fontes, and J. R. Patel. Phys. Rev. B **46**, 13631 (1992).

[Lar83] P. K. Larsen, J. H. Neave, J. F. van der Veen, P. J. Dobson, and B. A. Joyce. Phys. Rev. B **27**, 4966 (1983).

[Lee98] H. Lee, R. Lowe-Webb, W. Yang, and P. C. Sercel. Appl. Phys. Lett. **72**, 812 (1998).

[Leo93] D. Leonard, M. Krishnamurthy, C. M. Reaves, S. P. Denbaars, and P. M. Petroff. Appl. Phys. Lett. **63**, 3203 (1993).

[Leo94] D. Leonard, K. Pond, and P. M. Petroff. Phys. Rev. B **50**, 11687 (1994).

[Lew78] B. Lewis and J. C. Anderson. *Nucleation and Growth of Thin Films*. Academic, New York, 1978.

[Loh93] M. Lohmeier and E. Vlieg. J. Appl. Cryst. **26**, 706 (1993).

[Luc97] N. Lucas, H. Zabel, and H. Morkoc. J. Appl. Phys. **82**, 227 (1997).

[Mad83] A. Madhukar. Surface Science **132**, 344 (1983).

[Mad94] A. Madhukar, Q. Xie, P. Chen, and A. Konkar. Appl. Phys. Lett. **64**, 2727 (1994).

[Mai70] L. I. Maissel and R. Glang. *Handbook of Thin Film Technology*. McGraw–Hill, New York, 1970.

[Mar94] J. Y. Marzin and G. Bastard. Solid State Commun. **92**, 437 (1994).

[Mas93] J. Massies and N. Grandjean. Phys. Rev. Lett. **71**, 1411 (1993).

[Mat75] J. W. Matthews. Coherent Interfaces and Misfit Dislocations. In: J. W. Matthews, editor, *Epitaxial Growth*, volume Part B, New York, 1975. Academic.

[Max99] M. V. Maximov, A. F. Tsatsul'nikov, B. V. Volovik, D. A. Bedarev, A. Yu. Egorov, A. E. Zhukov, A. R. Kovsh, N. A. Bert, V. M. Ustinov, P. S. Kop'ev, Zh. I. Alferov, N. N. Ledentsov, D. Bimberg, I. P. Soshnikov, and P. Werner. Appl. Phys. Lett. **75**, 2347 (1999).

[Mil97] B. T. Miller, W. Hansen, S. Manus, R. J. Luyken, A. Lorke, J. P. Kotthaus, S. Huang, G. Medeiros-Ribeiro, and P. M. Petroff. Phys. Rev. B **56**, 6764 (1997).

[Moi89] J. M. Moison, C. Guille, F. Houzay, F. Barthe, and M. Van Pompay. Phys. Rev. B **40**, 6149 (1989).

[Moi91] J. M. Moison, F. Houzay, F. Barthe, J. M. Gerard, B. Jusserand, J. Massies, and F. S. Turco-Sandroff. Journal of Crystal Growth **111**, 141 (1991).

[Moi94] J. M. Moison, F. Houzay, F. Barthe, L. Leprince, E. Andre, and O. Vatel. Appl. Phys. Lett. **64**, 196 (1994).

[Mol98] N. Moll, M. Scheffler, and E. Pehlke. Phys. Rev. B **58**, 4566 (1998).

[Mui95] D. S. L. Mui, D. Leonard, L. A. Coldren, and P. M. Petroff. Appl. Phys. Lett. **66**, 1620 (1995).

[Mur92] V. Muraki, S. Fukatsu, Y. Shiraki, and R. Ito. Appl. Phys. Lett. **61**, 557 (1992).

[Mur99] R. Murray, S. Malik, P. Siverns, D. Childs, C. Roberts, B. Joyce, and H. Davock. Jpn. J. Appl. Phys. **38**, 496 (1999).

[Nab67] F. R. N. Nabarro. *Theory of Crystal Dislocations.* Clarendon, Oxford, 1967.

[Nab94] Y. Nabetani, T. Ishikawa, S. Noda, and A. Sasaki. J. Appl. Phys. **76**, 347 (1994).

[Nak98] A. Nakamura, A. N. Titkov, A. Ichida, V. P. Evtikhiev, and K. Kryganovskii. Appl. Phys. A **66**, S1035 (1998).

[Nea78] J. H. Neave and B. A. Joyce. Journal of Crystal Growth **44**, 387 (1978).

[Nev80] L. Nevot and P. Croce. Rev. Phys. Appl. **15**, 761 (1980).

[Nye57] J. F. Nye. *Physical properties of crystals.* at the clarendon press, Oxford, 1957.

[Ols75] G. H. Olsen. Journal of Crystal Growth **31**, 223 (1975).

[Osb87] G. C. Osbourn, Pl L. Gourley, I. J. Fritz, R. M. Biefold, L. R. Dawson, and T. E. Zipperian. Strained Layer Superlattices. In: R. K. Willardson and A. C. Beer, editors, *Semiconductors and Semimetals*, volume 32, S. Chap. 2, New york, 1987. Academic.

[Par54] L. G. Parrat. Phys. Rev. **95**, 359 (1954).

[Peo86] R. People. J. Appl. Phys. **59**, 3296 (1986).

[Pin78] Z. G. Pinsker. *Dynamical Scattering of X–ray in Crystals.* Springer–Verlag, Berlin, Heidelberg, New York, 1978.

[Ram97a] T. R. Ramachandran, R. Heitz, P. Chen, and A. Madhukar. Appl. Phys. Lett. **70**, 640 (1997).

[Ram97b] T. R. Ramachandran, R. Heitz, N. P. Kobayashi, A. Kalburge, W. Yu, P. Chen, and A. Madhukar. Journal of Crystal Growth **175/176**, 216 (1997).

[Rie85] K. H. Rieder. Structural Deterimnation of Surface and Overlayers with Diffraction. In: F. Nizzoli, K. H. Rieder, and R. F. Willis, editors, *Dynamical Phenomena at Surfaces, Interfaces and Superlattice*, volume 3 aus *Springer Ser. Surf. Sci.*, S. 2, Berlin, Heidelberg, 1985. Springer.

[Rob86] I. K. Robinson. Phys. Rev. B **33**, 3830 (1986).

[Rob88] I. K. Robinson, R. T. Tung, and R. Feidenhans'l. Phys. Rev. B **38**, 3632 (1988).

[Rub96] M. E. Rubin, G. Medeiros-Ribeiro, J. J. O'Shea, M. A. Chin, E. Y. Lee, P. M. Petroff, and V. Narayanamurti. Phys. Rev. Lett. **77**, 5268 (1996).

[Sai98] T. Saito, J. N. Schulman, and Y. Arakawa. Phys. Rev. B **57**, 13016 (1998).

[Sau97] S. Sauvage, P. Boucaud, F. H. Julien, J. M. Gerard, and J. Y. Marzin. J. Appl. Phys. **82**, 3396 (1997).

[Sch97] K. H. Schmidt, G. Medeiros-Ribeiro, J. Garcia, and P. M. Petroff. Appl. Phys. Lett. **70**, 1727 (1997).

[Sch98] M. Schmidbauer, Th. Wiebach, H. Raidt, M. Hanke, R. Köhler, and H. Wawra. Phys. Rev. B **58**, 10523 (1998).

[Shi90] K. Shiraishi and E. Yamaguchi. Phys. Rev. B **42**, 3064 (1990).

[Siv87] S. Sivananthan, X. Chu, and J. P. Faurie. J. Vac. Sci. Technol. B **5**, 694 (1987).

[Sny91] C. W. Snyder, B. G. Orr, D. Kessler, and L. M. Sander. Phys. Rev. Lett. **66**, 3023 (1991).

[Son94] S. Song and S. G. J. Mochrie. Phys. Rev. Lett. **73**, 995 (1994).

[Son95] S. Song and S. G. J. Mochrie. Phys. Rev. B **51**, 10068 (1995).

[Spe97] B. J. Spencer and J. Tersoff. Phys. Rev. Lett. **79**, 4858 (1997).

[Sta92] F. Stanglmeier, B. Lengeler, W. Weber, H. Goebel, and M. Schuster. Acta Crystallogr. A **48**, 626 (1992).

[Sti99] O. Stier, M. Grundmann, and D. Bimberg. Phys. Rev. B **59**, 5688 (1999).

[Str39] I. N. Stranski and L. von Krastanov. Akad. Wiss. Lit. Mainz–Natur. K1. IIb **146**, 797 (1939).

[Str82] G. B. Stringfellow. Rep. Prog. Phys. **45**, 469 (1982).

[Str98] M. Strassburg, V. Kutzer, U. W. Pohl, A. Hoffmann, I. Broser, N. N. Ledentsov, D. Bimberg, A. Rosenauer, U. Fischer, D. Gehrtsen, I. L. Krestnikov, M. Maximov, P. S. Kopev, and Zh. I. Alferov. Appl. Phys. Lett. **72**, 942 (1998).

[Sub86] S. Subbanna, H. Kroemer, and J. L. Merz. J. Appl. Phys. **59**, 488 (1986).

[Sud92] J. Sudijono, M. D. Johnson, C. W. Snyder, M. B. Elowitz, and B. G. Orr. Phys. Rev. Lett. **69**, 2811 (1992).

[Tan76] B. K. Tanner. *X-ray Diffraction Topography.* Pergamon Press, 1976.

[Ter96] J. Tersoff, C. Teichert, and M. G. Lagally. Phys. Rev. Lett. **76**, 1695 (1996).

[Toy93] H. Toyoshima, T. Shitara, P. N. Fawcett, J. Zhang, J. H. Neave, and B. A. Joyce. J. Appl. Phys. **73**, 2333 (1993).

[Upp87] P. N. Uppal, J. S. Ahearn, and D. P. Musser. J. Appl. Phys. **62**, 3766 (1987).

[Ven84] J. A. Venables, G. D. T. Spiller, and M. Hanbuecken. Rep. Prog. Phys. **47**, 399 (1984).

[Vin86] L. Vina and W. T. Wang. Appl. Phys. Lett. **48**, 36 (1986).

[Wak95] A. Wakahara, K. K. Vong, T. Hasegawa, A. Fujihara, and A. Sasaki. Journal of Crystal Growth **151**, 52 (1995).

[Wan86] W. T. Wang, R. F. Marks, and L. Vina. J. Appl. Phys. **59**, 937 (1986).

[War90] B. E. Warren. *X–ray Diffraction*. Dover Publications, Inc., New York, 1990.

[Wat95] G. M. Watson, D. Gibbs, S. Song, A. R. Sandy, S. G. J. Mochrie, and D. M. Zehner. Phys. Rev. B **52**, 12329 (1995).

[Wil62] R. K. Willardson and H. L. Goering. *Compound Semiconductors*. Reinhold, London, 1962.

[Woi95] J. C. Woicik, J. G. Pellegrino, S. H. Southworth, P. S. Shaw, B. A. Karlin, C. E. Bouldin, and K. E. Miyano. Phys. Rev. B **52**, R2281 (1995).

[Wol95] J. Wollschläger. Surface Science **328**, 325 (1995).

[Wol97] J. Wollschläger. Surface Science **383**, 103 (1997).

[Xie94] Q. Xie, P. Chen, and A. Madhukar. Appl. Phys. Lett. **65**, 2051 (1994).

[Xie95] Q. Xie, A. Madhukar, P. Chen, and N. P. Kobayashi. Phys. Rev. Lett. **75**, 2542 (1995).

[Zab92] H. Zabel and I. K. Robinson. *Surface X-ray and Neutron Scattering*. Springer–Verlag, Berlin Heidelberg, 1992.

[Zeg93] J. Zegenhagen. Surf. Sci. Rep. **18**, 199 (1993).

[Zha99] K. Zhang, A. Foede, Th. Schmidt, P. Sonntag, Ch. Heyn, G. Materlik, W. Hansen, and J. Falta. Phys. Stat. Sol. B **215**, 791 (1999).

[Zha00] K. Zhang, Ch. Heyn, W. Hansen, Th. Schmidt, and J. Falta. Appl. Phys. Lett. **76**, 2229 (2000).

[Zhe98] Y. Zheng, J. C. Boulliard, B. Capelle, A. Lifchitz, and S. Lagomarsino. Europhys. Lett. **41**, 623 (1998).

Publications

1 Grazing incidence structural characterization of InAs quantum dots on GaAs
K. Zhang, Ch. Heyn, W. Hansen, Th. Schmidt, and J. Falta
to be published as a special issue in Appl. Surf. Sci. for ICSFS-10 in Princeton, America, 2000.

2 Lateral distribution of buried self-assembled InAs quantum dots on GaAs
K. Zhang, J. Falta, Ch. Heyn, Th. Schmidt, and W. Hansen
in preparation for ICPS 25 in Osaka, Japan, paper number: ba858QH5, 2000.

3 Structural characterization of self-assembled InAs quantum dots grown by MBE
K. Zhang, Ch. Heyn, W. Hansen, Th. Schmidt, and J. Falta
J. Crys. Growth, in preparation for MBE 11th conference in Beijing, China, paper number:Ref-181-QD,2000.

4 Strain status of self-assembled InAs quantum dots
K. Zhang, Ch. Heyn, W. Hansen, Th. Schmidt, and J. Falta
Appl. Phys. Lett. accepted for publication in issue on August 28, 2000.

5 Ordering and shape of self-assembled InAs quantum dots on GaAs (001)
K.Zhang, Ch. Heyn, W. Hansen, Th. Schmidt, and J. Falta
Appl. Phys. Lett. **76**, 2229 (2000).

6 Formation and dissolution of self-assembled InAs quantum dots
Ch. Heyn, D. Endler, K. Zhang, and W. Hansen
J. Crystal Growth **210**, 421 (2000).

7 Study on distribution and shape of self-assembled InAs quantum dots grown on GaAs (001)
K. Zhang, J. Falta, Ch. Heyn, Th. Schmidt, G. Materlik and W. Hansen
Special Topic issue on Pure and Applied Chemistry (IUPAC) **72**, 199 (2000).

8 Structure of MBE grown InAs quantum dots studied by x-ray techniques
K. Zhang, Ch. Heyn, W. Hansen, Th. Schmidt, and J. Falta
Annual report, synchrotron radiation laboratory (DESY), Germany, 439 (1999).

9 X-ray interface characterization of buried InAs layers on GaAs (001)
K. Zhang, A. Foede, T. Schmidt, P. Sonntag, Ch. Heyn, G. Materlik, W. Hansen, and J. Falta
Phys. Stat. Sol. (b) **215**, 791 (1999).

10 Interface characterization of MBE growth InAs films on GaAs (001)
k. Zhang, A. Foede, J. Falta, P. Sonntag, Ch, Heyn, G. Materlik, W. Hansen
Annual report, synchrotron radiation laboratory (DESY), 481 (1998).
*online : http : //www − hasylab.desy.de/science/annual_reports/*1998/

11 Structure of buried InAs films on GaAs (001) by x-ray standing waves and crystal truncation rods
A. Foede, J. Falta, Th. Schmide, P. Sonntag, K. Zhang, W. Hansen, G. Materlik
Annual report, synchrotron radiation laboratory (DESY), 455 (1998).
*online : http : //www − hasylab.desy.de/science/annual_reports/*1998/

Acknowledgement

I gratefully acknowledge financial support by the Graduiertenkolleg "Physik Nanostrukturierter Festkörper" of German Science Foundation (DFG). Without this sponsored research project, there would be no chance for me to realize the present work.
I gratefully acknowledge the administration of department of physics for confirming my master of science degree as Dipl.-Phys. degree in Germany, so that I can pursue my study project as a doctoral student.
Many thanks for former leader of Graduiertenkolleg: Prof. H. Heyszenau and present leader: Prof. W. Hansen, who gave me lots of guidance on how to get on well with my study as a Graduiertenkolleg student.
In particular, I would like to sincerely thank my supervisor of my doctoral project– Prof. W. Hansen, who guided my doctoral study not only on how to carry out this project, but also on how to perform a research project correctly, to make my scientific mind growing up, and to become initiative in research. Also, his very diligently and strictly scientific attitudes leave me very deep impression, from which I am aware of the absolutely correct way in science. Therefore, from whom I know how to work in my future scientific career.
I would thank Prof. J. Falta who keeps very closely scientific cooperation with me. Especially, he supervised me to choose useful experimental methods to study the structures of InAs quantum dots as a commonly regarded difficult point, and to graduate my abilities on experimental performances of x-ray diffraction techniques with synchrotron radiation. Furthermore, he also concentrated on discussions of the observed experimental results. I should say, without him this cooperated project would not be carried out so quickly.
I would also thank Prof. G. Materlik, as a leader of the whole project, gave me a lot of benefit helps on how to start this project at the beginning of the project performance. This led me go to a shortcut way of my project.
I would thank my colleague Dr. Ch. Heyn who is a direct member of this project. Together with him, we grew and studied our InAs samples step by step and gradually we got experiences

on InAs QD growths by molecular beam epitaxy. Also, just from him I learned the knowledge of molecular beam epitaxy method.
Many thanks to Dr. Th. Schmidt, who worked together with me during my beamtime in DESY HASYLAB BW1 station. Here, I definitively note that without his direct cooperation, I would not carry on this project. Thanks him again for the days and nights working together in DESY.
Also, I thank Dipl.-Phys. A. Foede who worked in parts of this project as Diploma study. Some of the experiments such as crystal truncation rods and x-ray standing waves were performed by him. Moreover, he also helped me to deal with non-scientific communications during my beamtime in DESY HASYLAB ROMO I station.
I thank to secretariats Mrs. H. Gemegah, and B. Truppe who gave me their hands many times so that I could contribute to my work without difficulties.

Following I thank:

- Thank Dr. P. Sonntag who gave me helps when I worked at ROMO I station, and Dr. D. Novikov, as well as Dr. B. Adams when I performed my experiments at CEMO I beam station.
- Thanks also to Dr. P. Korecki who has worked for a short time in this project, to T. Hiort, R. Eisenhower, and J. I. Flege with whom I communicated scientifically during I worked in DESY. Also, a lot of helps from them have accelerated my project studies.
- Thanks to Prof. Anton who helped me to deal with RHEED pattern and TEM pictures.
- Thanks to all my colleagues in group W and H, who helped me to resolve a lot of daily things during these years.

Finally, I would also thank to my parents who help me to look after my daughter in my hometown and thus encourage me to make achievements in my scientific works. Lovely thank to my wife who stays with my daughter in China so as to let me dedicate to my work. Thanks to my sister and brother who also help to look after the whole family during the period I was not there. Without their helps, I would not concentrate on my research.